SiO and Silicon Graphite Composite Anode Material for Lithium-ion

Batteries

by

Hairui Jiang

Submitted in partial fulfilment of the requirements
for the degree of Master of Science

at

Dalhousie University
Halifax, Nova Scotia
August 2023

Dalhousie University is located in Mi'kma'ki, the
ancestral and unceded territory of the Mi'kmaq.
We are all Treaty people.

TABLE OF CONTENTS

LIST OF TABLES

LIST OF FIGURES

ABSTRACT

Lithium-ion batteries have been widely used in portable digital devices and electric vehicles. Silicon based anode materials including SiO and silicon graphite composites have attracted much attention due to their high volumetric capacity compared to conventionally used graphite. However, huge volume changes of Si-based materials can result in particle fracture and thick solid electrolyte interphase formation, leading to battery failure. One strategy of overcoming this is to utilize special binders that can maintain connection among electrode components and protect the active from side reactions. Another strategy is to design composite materials that include a Si component that is isolated from contacting the electrolyte. This thesis explores both these strategies.

Poly(acrylic acid) is known to be one of the best binders for Si-based anodes. A systematic investigation was undertaken on the effect of sodium poly(acrylic acid) binder molecular weight on silicon monoxide cycling performance. It was found that cycling performance was poor for low molecular weight binder, however this was primarily related to poor slurry rheology. It was found that if propylene glycol is used instead of water as a slurry solvent, the propylene glycol can take over the role of viscosity modifier from the binder. When propylene glycol is used as a solvent for slurries low MW NaPAA binders (e.g. 1.5 k NaPAA), the cycling outperformance of the resulting SiO electrodes outperforms conventionally made SiO electrodes with high molecular weight binder (e.g. 250 k NaPAA). These results show that binder molecular weight does only affect the cycling performance of Si-alloy based electrodes because of its role as a slurry viscosity modifier. If propylene glycol is used to increase slurry viscosity, then the molecular weight has little effect. This research enables small molecules to act as binders opening a new avenue of binder research.

Silicon-graphite composite anode materials for Li-ion cells were synthesized by embedding nano-Si into voids within natural graphite by mechanofusion followed by carbon coating by chemical vapor deposition. In the resulting structure, voids within the natural graphite were completely filled with silicon nanoparticles encapsulated in carbon. This resulted in the silicon being protected from reaction with the electrolyte. The as-prepared silicon-graphite composites were shown to cycle well in electrodes with no special binders (PVDF) and in conventional electrolytes without any additives (i.e. no fluoroethylene carbonate). Furthermore, nearly all the Si within the voids were fully active. This provides a promising and simple strategy for silicon-graphite composites that can be used as a drop-in replacement for graphite to increase Li-ion cell capacity. The electrochemical data and silicon morphology were discussed and investigated in this thesis.

LIST OF ABBREVIATIONS USED

BET	Brunauer-Emmett-Teller
BMF	Polyethylene blown microfiber.
BSE	Backscattered electron
CB	Carbon black
CCCV	Constant current constant voltage
CE	Coulombic efficiency
CMC	Carboxymethyl cellulose/Sodium carboxymethyl cellulose
CP	Cross-section polisher
CVD	Chemical vapour deposition
DEC	Diethyl carbonate
DMC	Dimethyl carbonate
EC	Ethylene carbonate
EDS	Energy dispersive X-ray spectroscopy
EV	Electric vehicle
FEC	Fluoroethylene carbonate
HF	Hydrofluoric acid
HOMO	Highest occupied molecular orbital
HT	Hydrothermal treatment

LCO	Lithium cobalt oxide
LFP	Lithium iron phosphate
LIBs	Lithium-ion batteries
LiPAA	Lithium polyacrylate
LMO	Lithium metal oxide
LNO	Lithium nickel oxide
LOMO	Lowest unoccupied molecular orbital
MW	Molecular weight
NaPAA	Sodium polyacrylate
NMC	Lithium nickel manganese cobalt oxide
NMP	1-Methyl-2-pyrrolidinine
NMR	Nuclear magnetic resonance
PC	Propylene carbonate
PEI	Poly(ethylene imine)
PG	Propylene glycol
PI	Polyimide
PVA	Polyvinyl alcohol
PVDF	Poly(vinylidene fluoride)
SBR	Styrene butadiene rubber
SE	Secondary electron
SEI	Solid electrolyte interphase
SEM	Scanning electron microscope
XRD	X-ray diffraction

ACKNOWLEDGEMENTS

First of all, I would like to thank my supervisor, Dr. Mark Obrovac. He is a very knowledgeable, passionate, and patient professor. With his support and encouragement, I can go through my research projects and finish the manuscript. I not only learned basic knowledge and methodology of lithium-ion batteries, but also enjoyed this short period graduate life.

I would like to thank my committee member, Dr. Josef Zwanziger, for his meticulous attitude. I would also like to thank all members of the Obrovac lab, I really appreciate their help. Particularly, I would like to thank Tim for training and equipment support. I would also like to thank Lea Gawne for all the paperwork.

Finally, I would like to thank my parents for their caring, understanding, and support.

CHAPTER 1   INTRODUCTION

1.1   Overview

Energy determines social economic development. Considering the increasingly serious climate crisis, renewable energy sources such as wind energy and solar energy are developed to substitute fossil fuels. In order to reduce the dependence on conventional fuels, wind power stations and solar power plants are being built worldwide. These clean energy sources have limitations due to their inherent intermittencies in supplying energy, so developing effective energy storage and conversion devices has been of great importance. Moreover, with the development of portable consumer electronics and electric vehicles, the demand for high performance rechargeable batteries is continuously growing. Of the rechargeable battery types, lithium-ion batteries have the predominant market position.

Alessandro Volta first invented the voltaic pile in 1799, which was the first purpose-built device for generating electricity chemically. His report accelerated the development of electrochemistry. The first lithium battery was made by Stanley Whittingham in the 1970s. It was comprised of a titanium disulphide (TiS_2) cathode vs. a lithium metal anode. John Goodenough ameliorated the cathode by replacing the TiS_2 with lithium cobalt oxide ($LiCoO_2$ or "LCO") and Akira Yoshino replaced the lithium metal anode with Hitherto a modern lithium-ion battery prototype was established and commercialized by Sony in 1991.

Compared with other types of batteries, the lithium-ion battery has many

advantages:

- High battery voltage

- High charge/discharge rate

- High specific energy density

- Wide working temperature range

- Low self-discharge rate

- No memory effect

- Long cycle life

- Low environmental pollution.

Benefiting from these merits, lithium-ion batteries occupy more and more of the energy storage market share.

To increase performance of electronic devices and electric vehicles, there is continuous demand for safer, higher energy-density, and longer cycle-life rechargeable batteries. Safety is always an important issue of lithium-ion batteries. Increasing the energy density of batteries can decrease the number of cells in a battery pack or reduce the volume and weight of a battery pack. Longer cycle life makes batteries more durable, which can improve customer satisfaction and avoid wasting materials.

This thesis is devoted to developing lithium-ion battery anode materials. By investigating how binders for Si-based anodes function and by making novel silicon/graphite composites, one can find a way to achieve higher energy density and longer cycle life even without specialized binders or electrolyte additives. Chapter 1 gives an overview of lithium-ion cells, especially concentrating from the anode perspective. Chapter 2 introduces the experimental techniques used in this study.

Chapter 3 shows how the molecular weight of polyacrylic acid affects cell performance by deconvoluting slurry rheology from electrode performance. Chapter 4 explores a new way to synthesize silicon embedded graphite and studies its electrochemical performance.

1.2   Lithium-Ion Batteries.
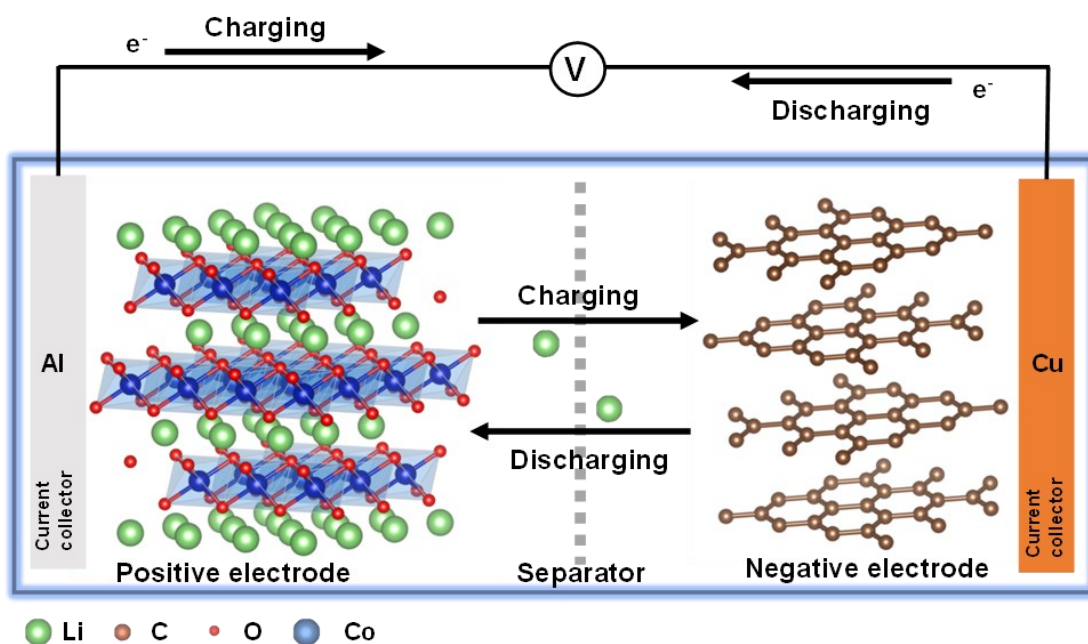
Figure 1.1   Schematic diagram of a lithium-ion battery (LiCoO$_2$/C).

Commercial lithium-ion cells are commonly available in three form factors: cylinder, prismatic and pouch. No matter how the batteries are assembled, they generally consist of a positive electrode, a separator, a negative electrode, electrolyte, and a cell casing. The positive and negative electrodes can store lithium ions at different potentials. They are made of active materials, binders and conductive agents coated on aluminum in the case of the cathode or copper foil in the case of the anode. The active

materials are the electrode component that stores lithium ions. Binders serve to hold all the electrode components together. The conductive agents form an electrically conductive network within the electrode coating. The aluminum and copper foils are used as current collectors to connect the electrode coatings with an external circuit. The separator is typically a polyolefin porous film placed between positive and negative electrodes to prevent short-circuit. The electrolyte is a lithium salt dissolved in an organic solvent, which allows lithium ions to shuttle between the positive and negative electrodes.

Typical lithium-ion batteries use a lithium transition metal oxide ($LiMO_2$, abbreviated as LMO, where M is a combination of Ni, Mn, Co with Al also often included) as the cathode active material and graphite as the anode active material as shown in Figure 1.1. When a Li-ion battery is charging, the positive electrode is oxidized while the negative electrode is reduced. Lithium ions move out from the cathode and diffuse via the electrolyte, passing through the separator, to the anode where they become reduced and intercalate within the anode active material structure. Simultaneous to this process, electrons flow from the cathode to the anode via an external circuit. As a result, electrical energy is converted to chemical energy. On the contrary, when a lithium-ion battery is discharging, lithium ions deintercalate from the anode active material and move to the cathode, where they intercalate within the cathode structure; while electrons go from the cathode to the anode, resulting in a conversion of chemical energy into electrical energy. The equations describing these reactions are shown below.

$$\text{cathode:} \qquad LiMO_2 \rightleftharpoons Li_{1-x}MO_2 + xLi^+ + xe^- \qquad (1.1)$$

anode: $$6C + Li^+ + e^- \rightleftharpoons LiC_6 \qquad (1.2)$$

overall: $$LiMO_2 + 6C \rightleftharpoons Li_{1-x}MO_2 + Li_xC_6 \qquad (1.3)$$
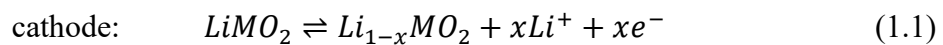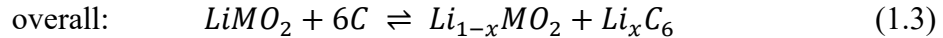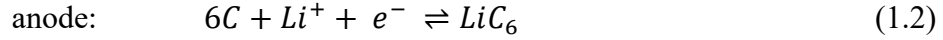
Equations (1.1) and (1.2) describe the processes that occur at the cathode and anode, respectively, during charge and discharge. Equation (1.3) describes the overall cell reaction. In these equations, LMO and graphite are used as representative active cathode and anode materials. Because lithium ions are alternately intercalating and deintercalating at the positive and negative electrodes during cell charge and discharge, this secondary battery type is also called a "rocking chair battery".[1] Because this type of cell is based on the intercalation of ions into a crystal lattice without changing the active materials' crystal structure greatly, rocking chair batteries can have very long cell lifetimes. In the case of lithium intercalation, the active materials have to be electronically conducting and ionically conductive towards lithium. Such active materials have vacancies in their crystal structure that can accommodate lithium-ions and that also provide a pathway for lithium-ion diffusion.

1.3   Cathode Active Materials

Cathode materials are a critical component that determines lithium-ion battery electrochemical performance, safety, and energy density. At present, the dominating cathode materials are lithium transition metal oxides. They can be categorized into three types by their crystalline structure: layered, spinel, and olivine. Layered-type cathodes are based on the α-NaFeO$_2$ structure type and were the first type of commercialized

cathode materials. Examples of layered type cathodes include $LiCoO_2$ (LCO), $LiNiO_2$ (LNO), $LiNi_xMn_yCo_{1-x-y}O_2$ (NMC), and $LiNi_xCo_yAl_zO_2$ (NCA). The theoretical capacity of LCO is 274 mAh/g, which corresponds to the removal of all the lithium from the $LiCoO_2$ structure. Coupled with LCO's high operating voltage (~4.4 V) this represents a very high energy density.[2] However, in practice LCO capacities of only about 170 mAh/g can be achieved because there is a risk of structural collapse when all lithium is extracted.[3] Furthermore, the high voltages associated with high delithiation levels will cause electrolyte side reactions which leads to irreversible capacity. Common upper voltage limits for cathodes in commercial cells are in the range of 4.2-4.3 V vs. Li/Li^+.[3] A major drawback of LCO is the high cost of cobalt, which limits LCO's market prospects. LNO is a potentially attractive alternative amongst cobalt-free cathodes materials, however, it has an intrinsic drawback in that nickel atoms tend to diffuse to the lithium layer and occupy lithium sites during cell operation. This reduces its capacity and cycling performance, making it unpractical for application in lithium-ion batteries.[4] Manganese is an abundant and cheap transition metal, therefore $LiMnO_2$ is also a potentially attractive cathode material. However, during lithiation and de-lithiation, layered $LiMnO_2$ converts to spinel. This crystalline change leads to volume expansion and shrinkage, resulting in capacity fade.[5]

Currently, the most widely used commercial cathode material is $LiNi_xMn_yCo_{1-x-y}O_2$ (NMC)[6] which combines nickel, manganese, and cobalt in the transition metal layer.[6] Nickel enables high capacity but too high a nickel content has the same bad inter-layer mixing effects as $LiNiO_2$. The presence of Mn helps improve the stability of the structure. Cobalt can help mitigate the lithium-nickel cation mixing. Since the

proportions of transition metals can be tuned, this material is capable of being tailored for use in various applications.

Spinel structured $LiMn_2O_4$ had attracted researchers' attention for decades because of its facile synthesis and low cost.[7] Its spinel structure includes a three-dimensional lithium diffusion network of face-shearing tetrahedra and octahedra. However, its widespread use has been limited because of its poor tolerance towards electrolytes cycling at elevated temperatures, which can cause irreversible structural changes, leading to capacity fade. Despite having significant lower energy compared to the layered oxides, olivine structured $LiFePO_4$ (LFP) has been widely used in power batteries for electric vehicles.[8] It stands out for the reasons of utilizing abundant resources, low cost, excellent safety and cycling stability.

1.4   Anode Active Materials

At first, lithium metal was used as an anode in lithium batteries. Lithium is the lightest metal (atomic weight is 6.941 g/mole) in the periodic table, so lithium metal has the highest specific capacity (3860 mAh/g). This corresponds to a high volumetric capacity of 2277 Ah/L. With the most negative potential (-3.04 V vs SHE), utilizing a lithium metal anode will result in the highest energy density battery for any given cathode. But lithium metal has severe safety issues because of the formation of high surface area dendritic lithium during cycling. Lithium metal anodes also have poor electrochemical stability because it is difficult to form a stable solid electrolyte

interphase (SEI) on lithium surfaces. These problems limit the commercialization of lithium metal in lithium secondary batteries. Recently, many studies have tried to utilize surface coatings[9] or electrode structural engineering[10] to stabilize lithium metal anodes. However, in the author's opinion, there is still a long way before lithium metal anodes can be used in practical applications. Nowadays, compounds that can intercalate lithium ions or form lithium alloys are utilized as anode materials in commercial applications.

1.4.1　　　Carbon-Based Anode Materials
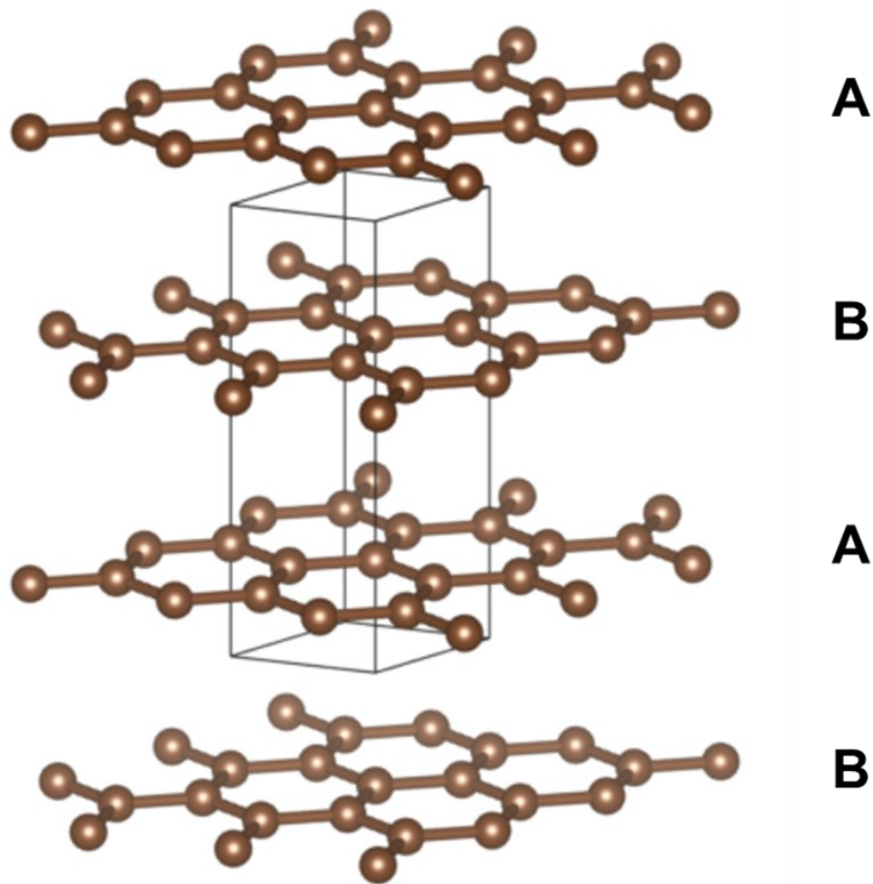
Figure 1.2　Crystal structure of graphite (2H stacking), the box represents a unit cell.

Carbon-based anode materials can be divided into different types, including graphite, soft carbon, and hard carbon. Currently, the most popular anode material in commercial lithium-ion batteries is graphite. Graphite has a layered structure as shown in Figure 1.2. In an ideal graphite lattice, the carbon atoms are sp^2 hybridized and form covalent bonds with neighboring carbon atoms to form a 2-dimensional honeycomb lattice. The honeycomb lattices (or graphene sheets) arrange in an ABAB

stacking sequence in a hexagonal lattice (2H stacking). The inter-layer spacing is 0.335 nm, where the graphene sheets are held together via the van der Waals force. These graphite sheets form the basal planes of graphite. An actual graphite particle additionally contains sp^3 hybridized carbon on its surface, forming an edge carbon plane.

The electrochemical reaction of graphite with lithium is well understood. The edge plane carbons present a high activity towards lithium and the electrolyte compared with basal plane carbons. During charging, lithium ions move to the anode and intercalate between the basal planes via the edge planes or other defect sites. Due to the hexagonal structure of the basal planes, intercalated lithium ions order so that they are as far away from each other as possible. This gives rise to staging phenomena from low to high concentrations of lithium ions, as shown in Figure 1.3. At first, lithium ions occupy the space between every 3rd basal layer. This is called a stage 3 intercalation compound. When more lithium ions intercalate, a stage 2 intercalation compound is formed, where lithium resides in the space between every 2nd graphene layer. At maximum lithiation, lithium ions occupy the space between all adjacent basal planes, forming a stage 1 intercalation compound.
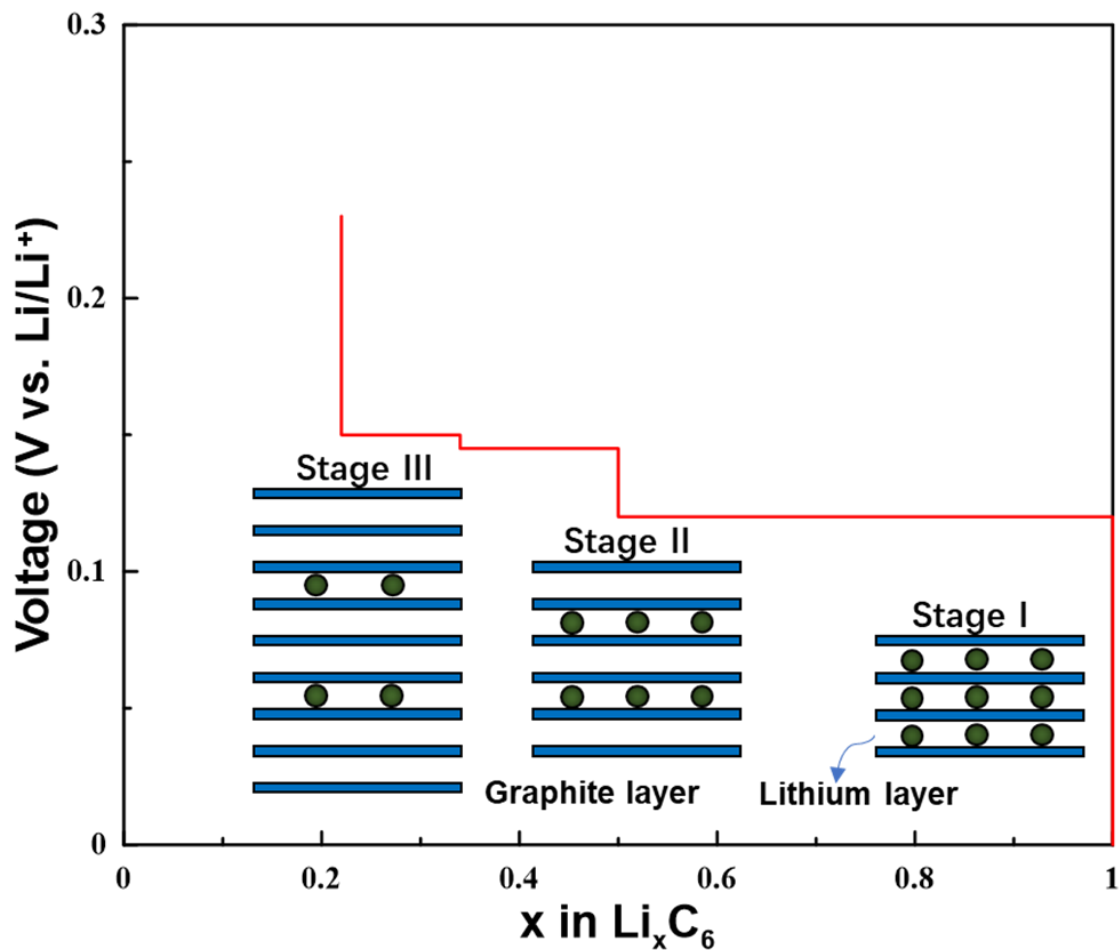
Figure 1.3   Schematic diagram of staging during the lithiation of graphite and the associated voltage profile.

Considering that the lithium atomic radius is 0.155 nm (ionic radius is 0.60 nm) and the graphite interplanar spacing d(002) is 0.34 nm, the layered structure of graphite is very suitable for lithium intercalation. During lithium intercalation process, the graphite stacking shifts from ABAB to AAAA. The intercalation process is associated with a volume expansion (10%), which is acceptable for practical electrodes. The fully lithiated form of graphite is LiC_6 which corresponds to a theoretical capacity of 372 mAh/g (719 Ah/L). In LiC_6 each carbon atom forms covalent bonds with three other carbon atoms and free electrons can roam within the basal planes, making lithiated

graphite a good electrical conductor. As a negative electrode material, graphite is excellent because it has low average voltage, good rate capability, low irreversibility, good cycle life, and good thermal and chemical stability. However, upon rapid charging and discharging, lithium metal dendrites can form on graphite particle surfaces, which causes some safety concerns. During lithium intercalation, solvent molecules can also intercalate between the graphite layers resulting in the exfoliation of graphite. Common solutions to these problems are using electrolyte additives to inhibit electrolyte decomposition[11] or modifying the graphite surface with conductive coatings.[12]

Besides graphite, amorphous carbon is another important carbonaceous anode material. According to the difficulty of graphitization, amorphous carbon can be divided into two types: soft carbon and hard carbon. Soft carbon is a type of amorphous carbon that can be graphitized at temperatures over 2500 °C. It consists of many small crystallites stacked in a similar direction. It can provide high capacity, but with high irreversible capacity. Hard carbon is a nongraphitizable carbon. The microcrystalline structure is randomly orientated and contains cross-links. Hard carbon also has a large capacity, but is limited by low density, high irreversible capacity, and severe voltage hysteresis.[13]

1.4.2   Anode Materials that form Alloys with Lithium

Lithium can form alloys with many metals and semimetals, such as aluminum, silicon and tin. Therefore, these materials are intensively studied as energy storage materials. Every element that can alloy with lithium is able to store one or more lithium

atom per host atom. This is large compared to the 6 carbon atoms required to store a lithium atom in LiC_6. Therefore, anodes based on lithium alloy forming elements are promising materials for high-capacity lithium-ion batteries.[14] The potential at which lithium is electrochemically inserted into a metallic host is generally higher than that for graphite, which lowers the energy density to some extent. On the other hand, this is also an advantage for lithium alloy forming elements, since lithium insertion at a higher potential could prevent the growth of lithium dendrites, thus improving the safety. The most serious problem of utilizing lithium alloy forming elements as anode materials is their large ($2\times$ to $4\times$) volume expansion and contraction during lithiation and delithiation. This huge volume change can destroy the electrode structure, leading disconnection of the electrode coating from the current collector or among active particles. For the particle itself, the volume change can cause fracturing, leading to particle pulverization, electrical disconnection and, ultimately, capacity loss. The active material particles' surface area also increases during lithiation due to volume expansion. The resulting fresh surfaces can react with the electrolyte, causing the loss of active material and the loss of lithium inventory. The main approaches to address these challenges have been to:

- Reduce the active material particle size to nanometers. By minimizing the size, the strain caused by volume expansion is alleviated.[15]

- Introduce a second phase with little or no volume expansion. As an example, graphite or inactive components may be used. These composites can buffer volume expansion and protect electrolytes from contacting the lithium alloying element. Although this approach sacrifices specific capacity, it results in improved

the cycle life.[16]

- Coat or encapsulate the active particles. By adding a coating layer, the contact area between the active and electrolyte is reduced, and the coating material can improve the mechanical strength of the active. As a result, particle pulverization and side reactions are suppressed.[17]

- Develop advanced binders. The function of binders is to maintain electrode structural stability. An effective binder has a good adhesion to the active and conductive agents and current collectors. The high-performance binder can relieve particle pulverization and disconnection.[18]

1.4.2.1   Silicon-Based Anode Materials

Silicon is the second most abundant element on the earth. According to the lithium-silicon phase diagram, the highest lithiated phase of silicon ($Li_{21}Si_5$) has a theoretical capacity of 4008 mAh/g. The volumetric capacity of silicon is 2257 Ah/L while graphite is 719 Ah/L. At room temperature, the electrochemical lithiation of Si does not follow the equilibrium phase diagram and the discharge capacity is limited to around 3578 mAh/g (or 2194 mAh/L).[19] An ex-situ XRD study showed that crystalline Si is lithiated via the following reaction:[19]

$$Si_{(cr)} + xLi^+ + xe^- \rightarrow Li_xSi_{(a)} \tag{1.4}$$

$$Li_xSi_{(a)} + (15 - x)Li^+ \rightarrow Li_{15}Si_{4(cr)} \tag{1.5}$$
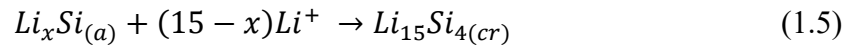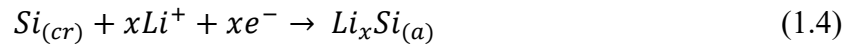
During this initial lithiation process, lithium reacts with crystalline Si, forming partially lithiated amorphous Li_xSi in a 2-phase region. Crystalline Si becomes fully converted

to amorphous Li_xSi at potentials below ~80 mV (vs. Li/Li$^+$). If lithiation is continued

and the potential becomes less than 50 mV (vs. Li/Li$^+$), the amorphous Li_xSi phase

spontaneously crystallizes into $Li_{15}Si_4$, which is the highest degree of lithiation possible

for silicon via electrochemical lithiation. The delithiation of $Li_{15}Si_4$ occurs according to

the following reactions:

$$Li_{15}Si_{4(cr)} \rightarrow 4Li_2Si_{(a)} + 7Li^+ + 7e^- \tag{1.6}$$

$$Li_2Si_{(a)} \rightarrow Si_{(a)} + 2Li^+ + 2e^- \tag{1.7}$$
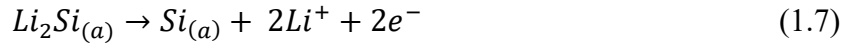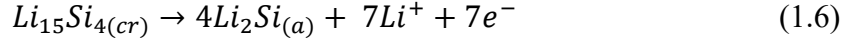
In the first half delithiation process, $Li_{15}Si_4$ delithiates to form amorphous Li_2Si. If

delithiation is continued, then amorphous silicon is formed. The formation of $Li_{15}Si_4$ is

thought to be detrimental for cycling, since Equation (1.6) describes delithiation in a 2-

phase region, which can result in strain and fracture between the two phases.

During subsequent cycling $Li_{15}Si_4$ may or may not form, depending on the lower

voltage limit. If during the lithiation of Si, the lower voltage limit is made to be higher

than 50 mV (vs. Li/Li$^+$), then no crystalline $Li_{15}Si_4$ is formed, and the lithiation reaction

will stop at the formation of lithiated amorhpous Si:

$$Si_{(a)} + xLi^+ + xe^- \rightarrow Li_xSi_{(a)} \tag{1.8}$$
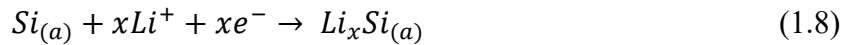
The above reaction takes place completely in a single-phase region. The subsequent

delithiation also takes place in a single-phase region:

$$Li_xSi_{(a)} \rightarrow Si_{(a)} + xLi^+ + xe^- \tag{1.9}$$
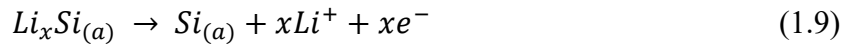
Avoiding the formation of $Li_{15}Si_4$ by such methods restricts cycling to single-phase

regions, thus avoiding internal particle strain associated with 2-phase regions.

The cost and energy density advantages of silicon have attracted much attention.

However, its volume expansion during lithiation is a key problem. Furthermore, silicon

is a semiconductor, its conductivity is 6.7×10^{-4} S/cm. Therefore, silicon-based electrodes need the incorporation of conductive agents. Silicon additionally reacts with the by-product of electrolyte decomposition, HF. These issues need to be addressed before commercialization.

To circumvent the challenges associated with Si anodes, there are a few strategies. One method to reduce the effects of volume expansion is to reduce the size of silicon. It has been reported that Si nanoparticles with diameters below 150 nm will not fracture during lithiation.[15] This is because when the size of Si particles is under 150 nm, the surface tension arising from swelling is not strong enough to generate cracks. However, nanosized silicon has a tendency to agglomerate and is sensitive to air. The huge surface area of nanoparticles also increases the extent of electrolyte decomposition reactions. Similarly, Si nano fibres or nanotubes have been synthesized. The one-dimensional structure can alleviate the volume change in the radial direction and facilitate the conductivity in the axial direction. But the growth of nano fibres or nanotubes is expensive. Another strategy is to use porous silicon. The porous structure has inner cavities. Some people think that such cavities can accommodate the volume expansion of Si and that the porosity is good for electrolyte permeation which can reduce the lithium-ion diffusion pathway. The specific surface area and porosity play an important role in the electrochemical performance of porous Si. A suitable range of specific surface area and porosity is important. Accordingly, Si prepared from different synthesis methods have different behaviour. Jia reported a magnesiothermic reduction method to make porous silicon.[20] After carbon coating, the composite exhibits good cycling life over 300 cycles.

The incorporation of silicon with other elements or compounds is another method to improve Si-based anode performance. Silicon carbon composites and silicon monoxides are successful materials. By combining silicon with other materials, the added materials can distribute the stress of silicon particles during volume expansion, helping to prevent the pulverization of the silicon particles. Meanwhile, the participation of other components may increase the conductivity and reduce the contact area with the electrolyte. For example, in silicon carbon composites, the excellent conductivity of carbon improves the electrode conductivity. Additionally, carbon acts as a buffer layer when the silicon particles expand. There are many ways to make silicon-carbon composites, such as by spray pyrolysis[21] method, chemical vapour deposition,[22] high-temperature pyrolysis,[23] and high-energy ball milling.[24] Jung used spray the drying method to synthesize porous silicon-carbon composite particles.[25] nanosized silicon and silicon dioxide and sucrose made up of the precursor solution. The resulting spherical particles were heated at 700 °C to carbonize the sucrose, followed by hydrofluoric acid (HF) etching. The prepared electrodes had 1956 mAh/g reversible capacity and retained 91% capacity after 150 cycles.

1.4.2.2   SiO

Silicon monoxide has attracted much attention. The structure of SiO is discussed controversially. One model proposed by Phillipp[26] is the random-bonding model. In this simplified model, silicon is statistically and randomly bound to another silicon or oxygen atom. According to this model, silicon monoxide is single phase. This model is supported by Nagamori et al. who found that SiO is homogeneous and that the oxidation

state of Si is 2+.[27] The other famous model is the random-mixture model proposed by Brady.[28] In this model silicon monoxide comprises a mixture of microcrystalline of silicon and silica phases. The existence of Si and SiO_2 in amorphous silicon monoxide was confirmed by NMR observations.[29] Commercial silicon monoxide is made by heating the mixture of Si and SiO_2. Such commercially derived SiO more conforms to the random mixture model in which the Si and SiO_2 phases are separated in a nano scale.

SiO forms lithium silicate (Li_xSi_yO), Li_2O during its first lithiation. This process is not reversible which means that it has a high irreversible capacity loss during the first cycle. However, the generated lithium silicate and lithium oxide can act as buffer component to alleviate the volume expansion of silicon. The charge and discharge reaction equations for SiO are described below:

$$\text{first lithiation: } SiO + xLi^+ + xe^- \rightarrow Li_xSi_yO + (1-y)Si \qquad (1.10)$$

$$\text{subsequent lithiation/delithiation: } Si + xLi^+ + xe^- \leftrightarrow Li_xSi \qquad (1.11)$$
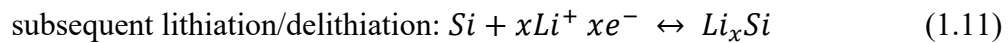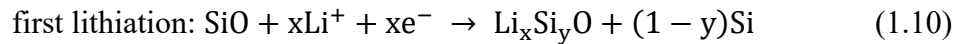
The main active material is silicon, formed by SiO reduction during the first lithiation. Compared with pure silicon, the volume expansion is much smaller, about 200%, but this volume expansion is still detrimental to cycle life. In addition, the irreversible reaction that occurs during the first cycle SiO's low electrical conductivity make SiO have a low coulombic efficiency and poor rate capability.[30]

1.4.2.3 Silicon-Graphite Composite

One of the most promising types of next generation anodes is silicon-graphite composites. Silicon-graphite composites combine the advantages of graphite and silicon. Graphite can provide high electrical conductivity and decent structural stability

while silicon can store more lithium ions. The low volume expansion of graphite (~10%) can dilute the volume change of silicon (~300%).

Depending on the incorporation of silicon in graphite, the gravimetric capacity increases linearly, while volumetric capacity increases greatly for low silicon contents (0-25 wt%). For high silicon contents, the volumetric capacity still increases but not as significantly as for low contents.[31] This means that incorporating 5-25 wt% silicon into graphite has a practical commercial value. In fact, some anode manufacturers already have blended some silicon into graphite. As an example of some of the issues with high Si content composites, Wetjen and coworkers[31] made silicon-graphite electrodes with silicon contents between 20-60 wt%.[32] They found that at high silicon contents, the electrodes had high irreversible capacity and low coulombic efficiency especially in first 50 cycles. At the same time a high electrolyte consumption occurred, and consequentially a thick SEI formed. The accumulation of SEI growth can hinder electronic and ionic conductivity resulting in the increase of electrode resistance. This overpotential leads to the gradual disappearance of $Li_{15}Si_4$. Apart from that, the repeated expansion and shrinkage can cause particle disconnection from the electrode coating.

Due to the different voltage profiles of silicon and graphite, during lithiation silicon is primarily lithiated before graphite and delithiated after graphite. During the lithiation, silicon is lithiated first and expanded.[33] Particle pulverization mainly happens during this phase. The electrode thickness change is linear with the content of silicon. Generally, the thickness change of electrodes is higher in the first few cycles and gradually levels off.

1.5   Electrolytes

Electrolytes provide ionic conduction within a lithium-ion battery. The electrolyte is not electronically conductive but transfers ions. The electrolyte in a conventional lithium-ion battery comprises a lithium salt dissolved in organic solvents. Ethylene carbonate (EC), propylene carbonate (PC), diethyl carbonate (DEC) and dimethyl carbonate (DMC) are common organic solvents used in lithium battery electrolytes. Generally, the electrolyte is expected to have good stability at high voltage, high lithium ionic conductivity, suitable melting and boiling range, and low viscosity. Typically, a mixture of different electrolyte solvents is used to balance all the advantages and disadvantages. There is also plenty of choice of lithium salts for diverse electrolytes, with $LiBF_4$, $LiClO_4$, and $LiPF_6$ being common. In order to obtain good performance, the radii of the lithium salt anion should be taken into consideration, with larger radii resulting in better lithium dissociation. However, anion radii that are too large would result in low anion mobility.

Electrochemical stability is another important factor for electrolytes since the electrolyte directly contacts the electrodes while the cell is operating. The potential of the anode is lower than the potential window of electrolyte organic solvents. During the first cycle, at the anode electrolyte decomposition starts at around 0.8 V (vs. Li^+/Li). The decomposition reactions depend on the electrolyte composition, the electrode chemistry and the cycling conditions. For a typical lithium-ion battery, the decomposition products at the anode commonly comprise Li_2CO_3, LiF, or Li-R (R is

an organic group). These side reactions happen at the surface of the anode and the side products adsorb on the anode surface forming an interfacial layer called the solid electrolyte interphase (SEI). The formation of the SEI layer consumes a large number of lithium ions leading to irreversible capacity loss. Ideally, the SEI layer is highly lithium conductive and electronically insulating, enabling cell operation while suppressing further electrolyte decomposition.
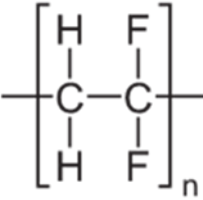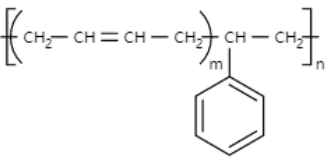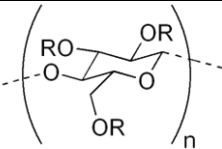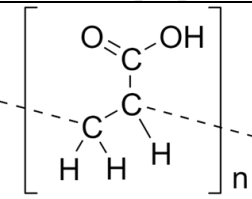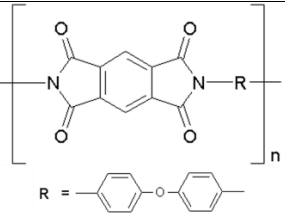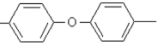
Electrolyte additives are optional electrolyte components, but their existence can greatly improve battery performance. Electrolyte additives participate in various reactions with electrodes or other electrolyte components during cell operation. Their functions include helping the formation of stable SEI layers, enhancing ionic conductivity, and enhancing thermal stability. For silicon-based anodes, fluoroethylene carbonate (FEC) is a common electrolyte additive. Due to the high electronegativity of fluorine, the HOMO and LUMO energies are lowered compared to EC,[34] resulting low reduction energy barrier. The FEC is therefore reduced before EC during anode lithiation and forms a dense SEI layer which helps prevent further electrolyte decomposition.

1.6   Binders

Binders are important electrode components. Binders usually are polymers such as polyvinylidene fluoride (PVDF). The structures of common binders used are shown in table 1.1. The main purpose of binders is to provide mechanical connections to all

Table 1.1 Chemical structure of common polymer binders

Name	Structure
Polyvinylidene fluoride (PVDF)	
Styrene butadiene rubber (SBR)	
Sodium carboxymethyl cellulose (CMC)	 $R = H$ or CH_2CO_2H
Polyacrylic acid (PAA)	
Polyimide (PI)	

particles in the electrode coating and the current collector. Most electrode materials undergo volume change during lithium intercalation and deintercalation. Therefore, the function of binders is significant for achieving long cycle life. Binders are also dispersing agents and slurry thickeners, in the electrode slurry making process, from which the electrode coatings are cast. The presence of the binder can help in establishing a homogeneous distribution of the active and conductive agents. Some binders are able to conduct lithium ions which can promote cycling performance.

During the electrode slurry-making process, binders are dissolved in a solvent. In the slurry, the binder solution wets the electrode coating particles. After coating and drying, a solid electrode coating is formed and binders provide mechanical force among particles. The interaction between binders and the electrode coating particles can be divided into intermolecular forces and chemical bonds.[35] For the binders in which intermolecular forces dominate, the binding strength comes from the van der Waals forces between polymers and particle surfaces and between different polymer chains. The first layer of binder in contact with the coating particles penetrates their pores or other structural defects. The large surface area of the active particles supplies lots of anchor points. The remaining binder acts like bridges, linking the particles together. For the binders which have functional groups, especially carboxylic or hydroxyl groups, covalent, ionic or metallic bonds can be formed between the binders with the coating particles. These chemical bonds and hydrogen bonds enhance the interparticle force. Compared to binders with only intermolecular forces, binders with functional binding groups generally show higher performance in lithium-ion batteries. [36]

To choose a right binder is very important, PVDF is the most commonly used binder in LIBs due to its mechanical properties, chemical stability to lithium, and electrochemical inertness at applied voltage. In addition, PVDF is used with N-methyl-2-pyrrolidone (NMP) slurry solvent, which has excellent wetting abilities, especially on carbonaceous materials, providing excellent slurry dispersions with good stability towards aggregation or settling. This is ideal for graphite anodes. PVDF/NMP-based slurries are also an excellent choice for cathode materials, since most layered cathodes are incompatible with water. However, the adhesive force of PVDF comes from the van

der Waals force. It is too weak to maintain the electrode structure for alloy anodes because of their volume expansion. PVDF also can swell in electrolytes (EC, DEC) at high temperatures or even react with lithium leading to a risk of thermal runaway.[37] Finally, although NMP has excellent properties as a slurry solvent, it is also expensive and toxic.

Sodium carboxymethyl cellulose (CMC) is another common binder used in lithium-ion batteries.[38] Since CMC is soluble in water, CMC enables water-based slurries. The monomer unit of CMC contains carboxylic groups and hydroxyl groups. The structure depends on the substitution of the cellulose unit, generally the 1-carboxymethyl ($-CH_2COO^-$) group and the 3-hydroxyl (-OH) groups per monomer unit. However, the cellulose backbone of CMC is rigid and brittle. In the industrial field, CMC is often incorporated with styrene butadiene rubber (SBR). The functional groups of CMC make it water soluble and give a strong binding force while SBR provides some flexibility and mechanical stability.

Polyacrylic acid (PAA) and its alkali metal salts is a new emerging binder that is also used in water-based slurries. PAA is synthesized by the polymerization of acrylic acid. It has a polyethylene backbone with a carboxylic group in each monomer. Compared with CMC, PAA has a much greater functional group density, and its polyethylene backbone is more flexible. During slurry making, the carboxylic side groups ($-COO^-$) adsorb on the active particle surfaces, lowering the surface energy or even forming bonds.[39] The electrostatic interaction of the carboxylic groups repel each other, resulting in a uniform slurry distribution. Due to the long chain length of PAA polymer and the chain flexibility, PAA can form a three-dimensional binder network.

This can help retain homogeneity during the slurry drying process. PAA binder additionally has a tendency to concentrate at the interparticle contacts, which means the bridges between particles are enhanced. This phenomenon can be increased by a "maturation" process in which the electrode is put in an 80% humid atmosphere. This concentration of binder between particles reenforces the electrode framework, so that better cycling stability is presented. Furthermore, these functional groups can etch copper current collectors, resulting in good adhesion. The improved adhesion between coatings and current collectors prevents the electrode delamination problem that is caused by active material volume expansion.[37,40]

Functional binders such as CMC and PAA are promising for silicon-based anodes. Such binders can form ester-like covalent bonds with siloxyl (SiOH) groups at the surface of Si, leading to enhanced mechanical properties.[18,41] These binders also have an influence on SEI formation. In the slurry, PAA binders will interact with silicon particles and absorb on their surface. These binders cover the bare silicon particle surfaces forming a conformal layer. When soaked in electrolyte, the artificial layer composed of PAA does not swell or take in carbonate electrolytes.[18] An effective coating of PAA can significantly decrease the contact surface area of silicon to electrolyte. During the first lithiation, there is cation exchange of PAA or NaPAA with the lithium ions in the electrolyte. PAA is lithiated to LiPAA via the substitution of protons or and NaPAA is converted to LiPAA via the substitution of sodium ions.[42] LiPAA has high lithium ionic conductivity, enabling the lithiation of silicon. After lithiation, an inorganic thin SEI layer forms beneath the PAA layer consisting of Li_2O, LiF and Li_xSiO_y in very first few cycles. Compared with uncoated Si-anode materials

(e.g. when PVDF binder is used), no significant ROCOOLi, decomposition product of carbonate electrolytes is detected and the amount of inorganic component and the thickness of SEI layer are greatly reduced.[43,44] This indicates that a highly modified SEI layer results when binders with carboxyl groups are used with Si-based anode materials. To conclude, PAA and CMC coat on silicon particles. The binder layer can prevent the direct contact between silicon and electrolyte. Therefore, the decomposition of electrolyte solvent is reduced, but the electrolyte salt such as $LiPF_6$ is decomposed on the surface of silicon forming a thin inorganic-like SEI layer. As a result, PAA and CMC binders suppress the reduction of carbonate solvents on Si-based anode materials during cell operation, significantly improving cycle life compared to non-functional binders, like PVDF.

To improve alloying active material cycling performance, a few strategies have been taken. Cross-linking is an effective way to strengthen polymer mechanical properties. Bonjae Koo reported using a thermal curing method to cross-link PAA and CMC for negative electrodes with silicon nanoparticles as the active material. The carboxylic groups from PAA form an ester group with hydroxyl groups of CMC at 150 °C under vacuum. Excess functional groups were found to bind to the hydroxide on silicon particles. As a result, the silicon nanoparticles were restrained in the 3-dimensional network built by cross-linked PAA and CMC and electric contact was maintained after volume expansion and contraction. As a result, the nano silicon retained 2000 mAh g^{-1} after 100 cycles at 30 °C. [45] As another example, Zhen Liu *et al.* reported a nano-silicon negative electrode incorporating a cross-linked polyvinyl alcohol (PVA) and poly(ethylene imine) (PEI) binder. The condensation reaction between hydroxyl groups

of PVA and the imido groups of PEI takes place during thermal heat treatment. The as-prepared PVA-PEI binder supported electrodes not only have a higher initial specific capacity of 3072 mAh g^{-1} and good long cycle life with 1063 mAh g^{-1} remaining after 300 cycles but also exhibit great rate capability retaining 1590 mAh g^{-1} at 10 A g^{-1} current density.[46] The PVA-PEI binders provide a strong interconnected 3-dimensional network and form a relatively stable artificial SEI layer on the nano silicon particles. The excess binder can encapsulate the active particles, reducing the surface area that is directly exposed to electrolyte and constrain the volume change of the coating within the binder network.

Specific binder properties can be achieved by molecular design of multifunctional binders. The alkane chain is good for flexibility; the fluorene group can improve electric conductivity; methyl benzoate ester groups increase the adhesion force; triethyleneoxide monomethylether side chains boost the electrolyte uptake.[47] Through molecular design, different functional groups are combined together to get improved mechanical strength, conductivity, flexibility and cohesion force.[40]

The performance of binders depends on many factors, such as pH value, cations, functional groups, molecular weight, slurry proportion, mixing and drying method etc. S. Y. Li studies the effect of aqueous slurry pH on the corrosion of aluminum current collectors. High pH value leads to worse aluminum corrosion and the side reaction products can migrate to the slurry and contaminate the active material resulting in high impedance and irreversible capacity.[48] Vogl et al investigated the interaction between CMC binder and silicon single crystal facets as a function of pH value.[49] At a low pH value, the adhesion force between silicon and CMC is reduced. Because the pK_a value

of the CMC is 3.9, when pH is lower, less CMC is dissociated. The protonated -COOH groups have more tendency to form hydrogen bonds with SiH or SiOH compared to deprotonated -COO$^-$ because the silicon surface is also negatively charged, there is repulsion force between -COO$^-$ and silicon surface oxide groups. The problem is that protonated -COOH is more favoured to interact with other CMC molecules instead of the silicon surface. So overall force decreases in acidic conditions.

Zhen-Ji Han discussed how alkali cations affect silicon graphite composite electrodes. [50] In this work, the researchers compared the electrochemical performance of polyacrylates that are neutralized by LiOH, NaOH, KOH and NH$_4$OH. Basically speaking, partially neutralized PAA performs better than non-neutralized PAA. It turns out that the best neutralization degree for LiOH, NaOH and KOH is 100%, 80% and 60%, with Na$_{0.8}$H$_{0.2}$PAA performing the best. Ammonium cations would decompose during battery operation impacting the electrodes, but ammonium neutralized PAA performance is still much better than PVDF. Hydrogen, lithium, sodium and potassium have larger and larger ion radii and they become easier to dissociate from polymer frames. Deprotonated -COO$^-$ groups repel each other, preventing major entanglement of PAA chains, allowing some sites to be available to form hydrogen bonds or physical cross-links between molecules, while fully dissociated PAA disables most intermolecular interaction.[39] Furthermore, ion exchange occurs between the PAA salts and the electrolyte, which can have beneficial effects. For instance, sodium salt added in electrolytes has been found to have a positive effect on performance.[51]

Polymer molecular weight is an important factor in terms of binder physicochemical properties. Different molecular chains influence the intermolecular

interaction caused by van der Waals force and physical cross-linking. Therefore, molecular weight affects the slurry's rheological properties and electrode performance. Lee et al. presented how molecular weight of sodium carboxymethyl cellulose (CMC) affect $Li_4Ti_5O_{12}$ anode performance. Their result showed that higher molecular weight binders led to a stronger adhesive strength and a better surface coverage and a higher impedance. 250k Na-CMC gave the best cell performance among all tested eletrodes.[52] Kasinathan *et al.* tested 3 different molecular weights of PAA (250k, 450k and 1250kg mol^{-1}), and 8 wt% of 250k gave the best rate capability and cycling stability for silicon alloy and graphite electrodes.[53] Although increasing molecular weight will improve viscosity, a too thick slurry is not good for mixing and casting. Hu *et al.* studied 6 different molecular weight LiPAA binders in silicon/graphite electrodes.[54] It was found that low molecular weight binders gave an inferior performance. The higher the molecular weight, the higher the apparent viscosity of the slurry and dynamic modulus of the LiPAA solution. Therefore, in the opinion of these authors, low molecular weight binders cannot maintain the cohesion and mechanical integrity of the electrodes and the optimum molecular weight range is 50-250 k in terms of vendor specification molecular weight. Miranda et al. utilized 3 different molecular weights of partially hydrolyzed polyacrylamide as binders for silicon anodes. They found that high molecular weight binders gave a stronger adhesion and mechanical strength while low molecular weight showed an improved mixing of electrode components. They concluded that for overall good performance, utilizing a moderate molecular weight binder is the best.[55] From the above research, there is an optimal molecular weight range for slurry making. If the slurry viscosity is too low, the mechanical property of both slurries and electrodes is

weak; if the viscosity is too high, the uniformity of the slurry is not easy to achieve. In short, the molecular weight has been taken into consideration when making slurries. For PAA, it is widely accepted that a 250k molecular weight outperforms other options.[53,54] However, what roles the molecular weight plays independent of maintaining slurry rheology in obtaining good the cycling performance is still not clear. The contribution of slurry rheology should be investigated independently. This is the goal of Chapter 3.

CHAPTER 2   EXPERIMENTAL TECHNIQUES

2.1   X-ray diffraction

X-ray diffraction is an effective technique to determine the structure of a crystalline material.[56] X-rays are a form of high-energy electromagnetic radiation with a short wavelength ranging from 10 pm to 10 nm. X radiation is generated by an X-ray tube in which a high voltage is applied to accelerate electrons exited from the cathode. The high-energy electrons collide with a metal target, typically Cu. The metal atoms are excited and release photons with characteristic wavelengths. During this process, the high-velocity external electrons can hit and eject an orbital electron from the inner electron shell of metal atoms and leave the orbital electron site vacant temporarily. Other orbital electrons from the outer shell can fill the vacancy. If the electron moves from the L shell to the K shell (2p to 1s), the photon is called K_α. If the electron moves from the M shell to the K shell (from 3p to 1s), it is called K_β. K_α is more intensive than K_β so K_α is often used in diffraction experiments while K_β is filtered by a special filter. For Cu K_α, the energy is 8.04 keV corresponding to an X-ray wavelength of 1.5406 Å.

In a solid crystal sample, the atoms are arranged in an array. Parallel atom planes are separated by regular distances. When an X-ray is incident on a sample, X-rays are scattered from each atom. Reflected parallel X-rays can interfere with each other. When two waves have the same frequency at the same point, interference can occur in either a constructive or destructive way. Constructive interference occurs when the phase

difference between two waves is an even multiple of π. The amplitude equates to the sum of two waves. On the contrary, when the phase difference is an odd multiple of π, destructive interference occurs. The amplitude is the difference between two waves. Bragg's law (equation 2.1) describes the necessary conditions for constructive interference due to the scattering of X-rays from a crystal:

$$n\lambda = 2dsin\theta \qquad (2.1)$$

Where λ is the wavelength of the incident X-ray, n is a positive integer, d is a lattice plane spacing of a crystal and θ is the incident angle between the X-ray and the lattice planes. The Bragg Law condition is illustrated in Figure 2.1 for the case of two incident X-rays scattered by two adjacent atoms. The lower beam travels an extra length of 2dsinθ compared to the upper beam. If 2dsinθ is equal to an even multiple of X-ray half-wavelengths, constructive interference occurs. Destructive interference occurs if 2dsinθ is equal to an odd multiple of X-ray half-wavelengths.

In the case of known crystal structures, characteristic peaks can be observed in the X-
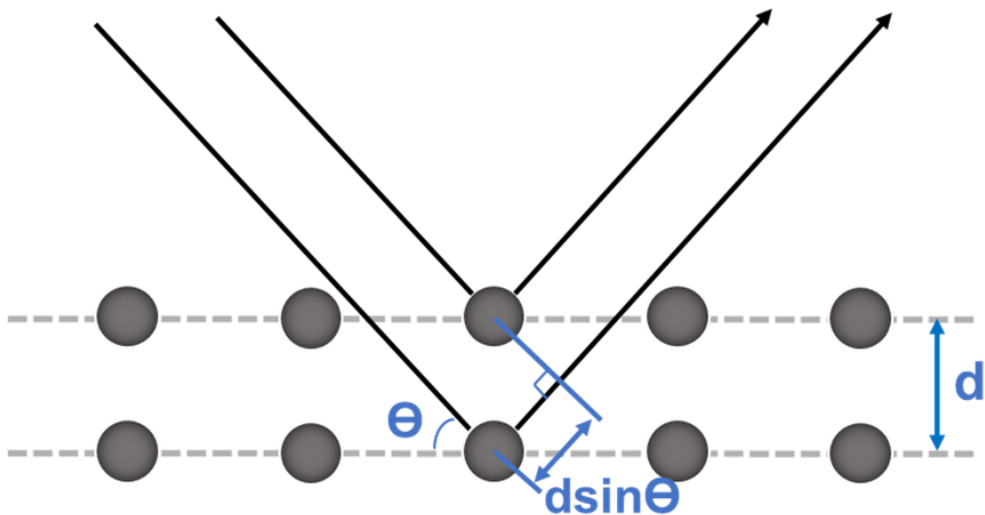
Figure 2.1   Schematic illustration of Brag's law

ray pattern.[57] The features can be identified by matching the positions of a reference XRD pattern.

In this thesis, XRD patterns were collected using a Rigaku Ultima IV diffractometer with a Cu Kα X-ray source, a graphite diffracted beam monochromator and a scintillation counter detector. A current of 40 mA and an accelerating voltage of 45 kV was used to generate X-rays. XRD patterns were recorded in a range of 10° to 80° with a step of 0.05° and 3 counts at each step.

2.2　　Scanning electron microscopy

Scanning electron microscopy is a common technique to acquire images in which researchers can get information about the topography and composition of solid samples.[58] SEM images are similar to photos taken by a camera. The utilization of electron beams makes SEM resolution significantly improved compared to light microscopy because electrons have very short wavelengths.

A typical SEM comprises an electron gun, condenser lens, apertures, a sample stage, detectors, and a vacuum pump.[59] A focused beam of electrons is generated and accelerated to scan the sample surface. The interaction between electron beams and samples generates various signals including secondary electrons (SE), back-scattered electrons (BSE), characteristic x-rays, absorbed current and transmitted electrons.

SEM electron beams have an energy ranging from 1 to 50 keV depending on the applied voltage. When the electron beam is focused on a sample, some of the electrons

lose energy by repeated random scattering and absorption within a waterdrop-shaped volume of the specimen known as the interaction volume. The interaction volume size typically is less than 100 nm in width and less than 5 µm in depth. The actual region is determined by the incident electron energy and the properties of a specimen. The interaction volume directly affects the resolution of an SEM.

When the high-energy electrons collide with a sample, elastic and inelastic scattering takes place. Secondary electrons come from inelastic scattering between the sample and the electron beam. The electrons from the outer electron shell of the sample are ejected by inelastic interactions. Secondary electrons have relatively low energy, which means that the secondary electrons from only the very top surface can escape and be detected by detectors. Secondary electron detectors are primarily installed in all SEMs and they can give detailed information on the topography of the sample surface. Backscattered electrons are high-energy electrons that are from the electron beam and are reflected or backscattered by the sample atoms' nuclei via elastic interactions. As the atomic number increases, the size of the nuclei grows, and the number of BSE increases. Thus, heavier elements give a brighter image. Therefore, the contrast and brightness of a BSE image can convey information about the composition of a sample. Characteristic X-rays are also emitted when a sample is exposed to high-energy electron beams. The inner shell electrons are knocked out by the primary electrons. The outer shell electrons fill the vacancy emitting X-ray photons at the same time. The X-ray photons are characteristic for specific elements, so they are used to analyze element distribution. This technique is called energy dispersive X-ray spectroscopy (EDS).

A JEOL JSM IT 200 and a TESCAN MIRA3-LMU FE-SEM equipped with an

Oxford Instrument X-Max 80mm2 SDD EDS system for chemical analysis were used for electronic microscopy in this study.

2.3   Ion milling

Ion milling is the process of removing a layer on a material to reveal the inside sample surface for high-revolution imaging or post-processing. In this study a JEOL IB-19530CP Cross Section Polisher (CP) was used to prepare smooth cross-sections of specimens. This CP is composed of a specimen chamber that is evacuated by a turbomolecular pump, ion source, and an X and Y axis-drive specimen stage. Ion milling utilizes an argon ion beam. To produce an ion beam, argon is charged and accelerated by a high-voltage electric field. The ion beam is emitted perpendicular to the specimen which is covered by a shielding plate. The protruding part of the sample is exposed to the ion beam and is milled away. The use of the broad argon ion beam and shielding plate enables the preparation of smooth cross-sections with less distortion compared to normal mechanical polishing. Therefore, after cross-sectioning, the sample is ready for SEM observations.

Three main parameters can be adjusted in a CP: the working potential (2-8 kV), the argon gas flow, and the cutting time. Argon flow and the working potential can affect the energy of the argon ion beam. Sufficient cutting time is given to get a good cross-section. Cut depth depends on the properties of the sample and milling time. In this thesis, all samples were operated at 6 kV with an argon gas flow of 5.5.

2.4   Gas pycnometery

A gas pycnometer is a laboratory instrument for measuring the density of solids.[60] The mass density of a solid sample is its mass divided by its volume. The mass can be measured with a scientific balance. The volume is determined by a gas pycnometer.

A gas pycnometer employs gas displacement and the relationship between volume and pressure known as Boyle's Law.[61] In this study a IQIPyc pyrometer was utilized. This instrument can give accurate measurements of the true volume (density) of solids using the gas expansion method. To do this the instrument uses two chambers of known volumes V_1 and V_2. One chamber is removable to hold the sample (V_1) with a gas-tight lip and the other chamber is an internal volume chamber (V_2). Helium is used as an inert gas.

During a measurement, the pressure (P_1) of the sample chamber is recorded after equilibrium. Then the valve connecting the two chambers is opened. The gas pressure is balanced in the two chambers. After equilibrium, the pressure (P_2) is recorded. According to Boyle's Law, the volume of the sample can be calculated:

$$V_S = V_1 + \frac{V_2}{1 - \frac{P_1}{P_2}} \qquad\qquad (2.1)$$

2.5   Brunauer-Emmett-Teller (BET) surface analysis

The BET method is widely used to measure the surface area and pore size of solid materials.[62] The BET method is based on Langmuir theory. Gaseous molecules condense on the surface of solids when pressure or temperature changes, which is

caused by van der Waals forces. This phenomenon is called adsorption. On the contrary, gaseous molecules evaporating from a solid's surface is called desorption. Langmuir's theory presumes that gaseous molecules are chemically adsorbed on the surface as a monolayer where all adsorption sites are equivalent and independent and can be occupied by only one molecule. The amount of adsorbed gas in a certain condition is a function of surface area. By measuring the quantity of adsorbed gas, the surface area is determined. However, BET theory assumes that gaseous molecules can physically adsorb on a solid in layers infinitely. Each layer is independent and obeys Langmuir's theory. BET measurement usually uses nitrogen gas as adsorbate gas at the boiling point of liquid nitrogen. A Nova 4000e surface analyzer was used for BET measurements in this thesis.

2.6   Viscometer

The viscosity of a fluid is a measure of its resistance to deformation at a given rate. The viscosity is the result of internal frictional force between adjacent layers of fluid that are in relative motion. There are two kinds of fluids, Newtonian fluids and non-Newtonian fluids. The viscosity of Newtonian fluids does not depend on the shear rate and they follow Newton's law of viscosity as shown in Equation 2.2.

$$\tau = \mu \frac{\partial u}{\partial y} \tag{2.2}$$

Where τ is shear stress, μ is viscosity, and $\partial u/\partial y$ is velocity gradient. The unit of viscosity is commonly expressed as centipoise (cP).

Non-Newtonian fluids are those fluids that do not obey Newton's law. Their

viscosity is subject to many additional variables such as temperature, shear rate, measurement conditions, time, previous conditions, composition, and additives.[63] Battery electrode slurries are suspensions that are non-Newtonian fluids. The homogeneity and stability of the electrode components are determined by the homogeneity and stability of the slurry components, which is a complex system composed of multi-component suspended particles, and its uniformity and stability are difficult to directly observe.[63] Viscosity is one indicator of electrode slurry rheological property. It must be measured with great care because of the electrode slurry's non-Newtonian properties, the tendency for solid particles to settle, and temperature effects.

There are many types of viscometers including U-tube viscometers, vibrational viscometers, rotational viscometers, and so on. The viscosity measurements in this thesis were performed with a Viscolead ONE rotational viscometer. It is based on the measurement of the torque of a rotating spindle at a specific velocity. When rotating a spindle in a fluid, a resistance is applied to the spindle. The viscosity is determined by measuring the torque on a vertical shaft that rotates the spindle. The viscosity is automatically calculated and displayed on a screen for every spindle/speed combination. To ensure accuracy, the viscometer is calibrated utilizing viscosity standards.

2.7 Electrochemical measurement

Coin cells were used for all electrochemical measurements in this thesis. Figure 2.2 shows an exploded view of a coin cell, which consists of a working electrode, blown microfiber (BMF, 3M Company) and expanded polyethylene (Celgard 2301) separators, a lithium foil counter/reference electrode, and copper spacers. The BMF separator is

utilized to more evenly distribute stack pressure within the cell, while the Celgard separator has small pores that inhibit lithium dendrite formation. The spacers take up empty volume in the cell, so that the cell can itself acts as a spring, applying pressure to the cell stack. The electrodes and separator are saturated with electrolyte during cell assembly.

To prepare the working electrodes, a slurry including the active materials, conductive agent (Super C65, Imerys Graphite and Carbon), binders (e.g. PAA or PVDF) and slurry solvent (e.g. water or NMP) was made. Depending on the projects, different component ratios were used. The electrode slurries were mixed by a Mazerustar high-shear mixer at 5000 rpm for 20 minutes or mixed by planetary ball milling (Retsch PM200) with 3 tungsten carbide balls (7/16 inch in diameter). Mixed slurries were spread onto a piece of 15 μm thickness copper foil (Furukawa) with a coating bar having a 0.004-inch gap (or 0.008-inch for loading consideration). The resulting coating was then dried, typically for 1 hour at 120 °C in air. Electrode disks with an area of 1.30 cm^2 were punched from the coating after drying and heated under vacuum at 120 °C overnight before cell making. Typical electrode loadings were 1.5~2.5 mAh/cm^2. Coin cell assembly was conducted in an argon-filled glovebox. 2325 coin cells were made with a working electrode versus lithium metal foil (99.9%, Sigma-Aldrich, 38 μm). The electrolyte was 1 M LiPF$_6$ (BASF) dissolved in a solvent mixture of ethylene carbonate: diethylene carbonate: fluoroethylene carbonate (EC: DEC: FEC, all from BASF) in a volume ratio of 3:6:1. One layer of Celgard 2301 and one layer of BMF were used as separators. Two copper spacers were used to guarantee proper internal pressure and electrical connectivity.
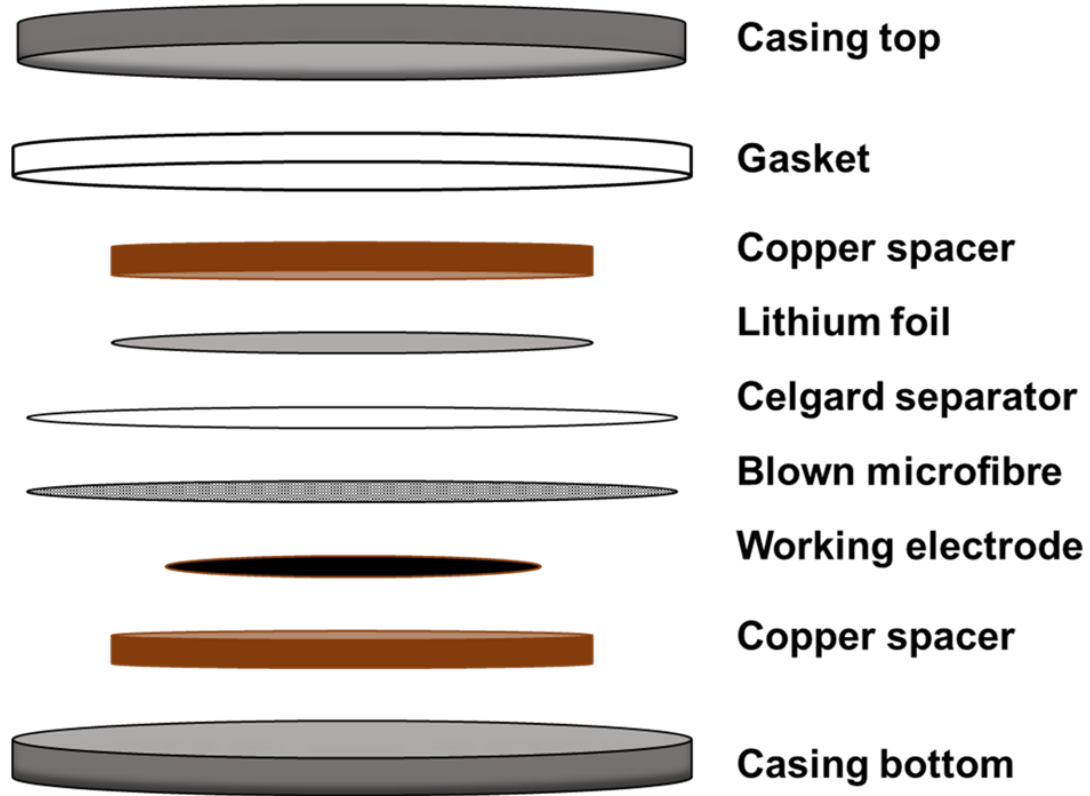
Figure 2.2   Exploded structure view of a coin cell.

Electrochemical properties of the working electrode , such as specific or volumetric capacity, irreversible capacity, coulombic efficiency, voltage hysteresis, and cycle life are evaluated by galvanostatic cycling. In a half cell, specific capacity is calculated by lithiation or delithiation charge divided by the active material mass. The irreversible capacity is defined as the capacity loss between the first discharge and charge processes. For lithium-ion battery anode materials, the coulombic efficiency (CE) of the nth cycle ($ŋ_n$) is defined as:

$$ŋ_n = \frac{Q_{n,delithiation}}{Q_{n,lithiation}} \qquad (2.2)$$

where $Q_{n,delithiation}$ is the amount of charge that passed through the cell during the

delithiation of the negative electrode material, and $Q_{n,\text{lithiation}}$ is the amount of charge that passed through the cell during the lithiation of the negative electrode material during the nth cycle. Coulombic efficiency is an important indicator of charge transfer efficiency in an electrochemical reaction. Voltage hysteresis is calculated as the difference between the mean charge and discharge voltages.

Coin cells were cycled at $30 \pm 0.2\,°C$ between 0.005 V and 0.9 V using the Neware battery testing system. During galvanostatic charge and discharge of a cell, the current is often expressed as a C rate. 1C means it takes 1 hour to fully charge or discharge a cell. C/5 means it takes 5 hours to completely charge or discharge. Cells were held at the constant potential at the end of each discharge (lithiation) half-cycle until a lower current limit was reached to simulate constant current-constant voltage (CCCV) cycling of commercial Li-ion cells. During the first cycle, cells were cycled at a C/20 rate with a C/40 lower current limit at the end of discharge followed by charging at a C/20 to 0.9 V. For the next cycles a C/5 current was used with a C/20 lower current limit at the end of discharge and a C/5 charging current.

CHAPTER 3 DECONVOLUTING SLURRY RHEOLOGY FROM BINDER FERFORMANCE IN Si-BASED ANODES[a]

3.1 Introduction

As mentioned in Chapter 1, binders are important for maintaining the stability of Li-ion battery negative electrodes containing Si-based active materials during charge-discharge cycling.[64,65] While the commonly used polyvinylidene difluoride (PVDF) binder is sufficient for graphite negative electrodes, its use with Si-based active materials results in capacity fade. This is because PVDF only connects with active material surfaces by weak Van der Waals forces. As a result, PVDF does not conformally coat the active materials, leaving bare active material surfaces in direct contact with electrolytes. Many studies show that binders that have functionalities to form chemical bonds with Si-based active material surfaces (such as carboxymethyl

---

[a] This chapter was adapted with permission form H. Jiang, C. Wei, M. N. Obrovac. Deconvoluting Slurry Rheology from Binder Performance in Si-Based Anodes, which was submitted to the Journal of the Electrochemical Society for publication on June 26, 2023 and is currently under review. H. Jiang's contribution included conducting all experiment and analysis work and writing the manuscript. C. Wei's contribution included performing preliminary experiments. M. N. Obrovac supervised the experiments and edited the manuscript.

cellulose (CMC)[49], alginate[66], polyimide (PI)[6768], phenolic resin (PR)[69], and poly(acrylic) acid (PAA)[39]) can substantially improve Si-based negative electrode capacity retention compared to PVDF.

Of the functionalized binders, CMC, alginate, and PAA are especially attractive since they dissolve in water. Such binders have abundant hydroxyl functional groups which can form covalent bonds with silicon. As a result, such binders conformally coat Si-based active material surfaces, forming an artificial solid electrolyte interface that prevents electrolyte decomposition.[18] PAA, in particular, has received much attention because of its high hydroxyl density. As a result, PAA has a 10 times larger adhesion strength to copper current collector compared to CMC and can cover the active particles more efficiently.[22] Thus, Si-based electrodes using PAA binder typically perform better than those using CMC binder.[70] The performance of PAA can be improved further by modification of its neutralizing its carboxylic acid groups to form a PAA salt (e.g. neutralization with LiOH or NaOH to form LiPAA and NaPAA). After neutralization, the PAA⁻ chains stretch individually and disentangle due to the repulsion of carboxylate groups. Thus, a superior and homogeneous distribution of slurry components is obtained.[71]

It is known that molecular weight (MW) is also an important factor for polymers. The longer chains have more intermolecular interactions such as van der Waals forces, which can increase the overall strength and toughness. Moreover, as the chains are elongated, they become much easier to entangle with each other. Especially for polymers with polarized groups, their inter- and intramolecular forces reduce their mobility. The combined effect of molecular interactions and polymer length enables

43

binders to both act as a dispersant and as a viscosity modifier.[53,54] These effects are highly important for maintaining slurry stability during the coating process. Without such effects, active particles and conductive additives can settle or aggregate during the slurry making or coating processes, resulting in poor electrode homogeneity.

Based on the above considerations, polymer binders are vitally important for establishing optimal slurry rheology and in the final mechanical properties of the electrode. In the case of Si-based active materials binders also vitally contribute to electrochemical properties. It is not clear if these different roles are related to each other. For instance, it has been reported that the molecular weight of PAA has a great influence on the cycling performance, with molecular weights in the range of 24-150 k (here "k" is used as shorthand for 1000 g/mol molecular weight units) being optimal for silicon/graphite composite anodes.[54] Another study found that 250 k PAA gave the best performance.[53] However, it is not clear from these studies if the effect of binder molecular weight is due to the optimization of slurry viscosity, electrode mechanical properties, interactions with the active particle surfaces, or all three of these effects. It has been shown that the molecular weight of binders is not the only factor that affects the cycling performance of Si-based anodes. In fact, research has demonstrated that single molecules or inorganic salts can serve as effective binders for Si-based anodes.[72] Such electrodes can have excellent cycling retention, as long as the molecules or inorganic salts contain a high concentration of carboxyl groups.[72]

The conflicting nature of the above reports likely stems from the inability to separate the very important, but very different roles binders have in the electrode slurry (as a rheology modifier) and in the final electrode coating (imparting mechanical

strength and providing an artificial SEI layer). It is likely that the optimal binder properties needed for establishing good slurry rheology are not the same as the optimal binder properties needed to obtain good electrode cycling performance in the dried electrode coating. In order to fully understand the role of binder MW on electrode coating performance, contributions that the slurry rheology and final electrode cycling performance need to be investigated independently. No previous investigations could be found that have accomplished this or nor could any previous methods be found that could enable such an investigation.

In this study, SiO was used as the active materials because it has lower volume expansion compared with Si during cycling. The lithium silicate and lithium oxide formed during the first lithiation can help to alleviate the volume change. But SiO still has large volume change up to 200%. Such great volume change will result particle pulverization and disconnection. The cycling performance of SiO is highly related to the binder functionality. Therefore, SiO is a good choice to test binder performance for silicon-based anodes. Another reason that SiO was selected as the active material is because SiO anode materials have been commercialized for a long time. The BTR SiO was used because of its high quality, and it is available for everyone.

The goal of this study is to understand how binder molecular weight and functionality individually contribute to the cycling performance of Si-based anode materials. To do this, NaPAA with different molecular weights were evaluated as binders for SiO anodes. Since the binder MW affects slurry rheology, which in turn affects the final coating quality, this variable needed to be removed. This was accomplished by utilizing viscous solvents to control the slurry viscosity independently

of the binder MW. This allowed the effects of binder MW on the final coating performance to be studied independently of its contribution to the rheology of the electrode slurry. This is apparently the first study in which the role of binder MW in establishing slurry rheology could be completely eliminated from the study of binder performance in the final electrode coating.

3.2   Experimental

Electrode binders were prepared from polyacrylic acid (PAA) aqueous solutions or sodium polyacrylic acid (NaPAA) powders with different molecular weights (1.2 k to 450 k), as listed in Table 3.1. To make standard electrodes 10 wt% NaPAA solutions in water were first prepared. To make 10 wt% aqueous solutions of NaPAA from NaPAA powders, the powders were simply dissolved with an appropriate amount of distilled water. To make 10 wt% aqueous solutions of NaPAA from aqueous PAA solutions, the PAA solutions were diluted with distilled water and then 2 M NaOH (>98%, sigma-aldrich) was added in an amount required by stoichiometry to fully sodiate the PAA carboxylic acid groups. Some electrodes with low MW NaPAA (1.2 k, 3 k, 8 k, and 15 k) were also prepared with propylene glycol (PG) as the main slurry solvent. For PG-based slurries, concentrated NaPAA aqueous solutions were diluted by adding PG to make the solutions 10 wt% in NaPAA. All solutions were mixed using a magnetic stirrer at 800 rpm overnight to ensure complete dissolution.

Table 3.1 Molecular weight, source, and state as received of the binders used in this study.

MW (g/mol)	vendor	state as received
1,200	Aldrich	poly(acrylic acid, sodium salt) 45wt% in H_2O
3,000	Polyscience	poly(acrylic acid, sodium salt) 40wt% in H_2O
8,000	Aldrich	poly(acrylic acid, sodium salt) 45wt% in H_2O
15,000	Aldrich	poly(acrylic acid, sodium salt) 35wt% in H_2O
50,000	Polyscience	poly(acrylic acid) 25wt% in H_2O
100,000	Aldrich	poly(acrylic acid) 35wt% in H_2O
250,000	Aldrich	poly(acrylic acid) 35wt% in H_2O
450,000	Aldrich	poly(acrylic acid) powder

SiO (BTR) was used as the electrode active material. It was either used as supplied or ball milled to make fine particle SiO (FP-SiO) by placing 0.5 ml of SiO powder and 180 g of 1/8 inch diameter stainless steel balls in a 60 ml hardened steel vial (SPEX CertiPrep). The vial was sealed in an argon atmosphere in a glovebox and then milled for 8 hours with a high-energy ball mill (8000D Mixer/Mill, SPEX CertiPrep). FP-SiO was then recovered by adding ethanol to the vial, ball milling for an additional 5 minutes, and then collecting and drying the resulting slurry.

Electrodes were prepared with an active/carbon black/binder ratio of 70/5/25 v/v/v ratio based on true densities. To prepare electrode formulations, 0.5554 g SiO (ρ_{SiO} =1.984 g/ml) or 0.6409 g FP-SiO (ρ_{FP-SiO} = 2.289 g/ml), 0.0452 g of carbon black (C-ERGY Super C65, Imerys S.A., ρ_{CB} = 2.26 g/ml), 1.716 g of 10 wt% NaPAA solution

(water or PG-based, ρ_{NaPAA}=1.716 g/ml), and 1.65 g of distilled water or 1.72g PG (to make the total solids: liquid ratio 1:8 v/v) were combined by mixing with a high shear mixer for 20 minutes at a speed of 5000 rpm. The slurries were then coated on copper foil using a 0.004-inch coating bar. Standard electrodes were dried in air at room temperature for one hour and then at 120 °C for an additional hour. Since PG has a lower vapour pressure than water, PG-based coatings were first dried in air at 40 °C for 1 hour and then at 120 °C for another hour. PG-based coatings were placed vertically in the thermal oven to mitigate binder/carbon black migration during drying. Disk electrodes (1.3 cm^2 diameter) were cut from the dried electrode coatings and then additionally dried at 120 °C in vacuum overnight before making cells.

Slurry viscosities were measured by a rotational viscometer (Fungilab viscolead one) equipped with a Brookfield small sample adapter (SSA18/13R). The viscometer was calibrated by viscosity reference standard RT50 and RT5000 (Paragon Scientific Ltd). Slurries were prepared as described above. After being mixed for 20 minutes, the slurries were transferred to the small sample adapter immediately. Viscosity readings were then recorded every 10 minutes for 1 hour.

Half cells were constructed in an Ar-filled glove box from standard 2325 coin cell hardware. Each cell contained a working electrode, 1 layer of microporous polypropylene separator (Celgard 2032), one layer of polypropylene blown microfiber separator (3M Company), and lithium foil (99.9%, Aldrich). The electrolyte solution consisting of 1 M LiPF$_6$ is dissolved in an ethylene carbonate/diethylene carbonate/fluoroethylene 6:3:1 v/v/v solvent solution (all from BASF). The cells were allowed to rest for 8 hours before cycling. Electrochemical tests were performed using

a Neware Test System. Cells were cycled galvanostatically within potential limits of 0.005 V to 0.9 V. Cells were held at a constant potential at the end of each discharge (lithiation) half-cycle until a lower current limit was reached to simulate constant current-constant voltage (CCCV) cycling. During the first cycle, cells were cycled at a C/20 rate with a C/40 lower current limit at the end of discharge. For the following cycles, a C/5 current was used with a C/20 lower current limit at the end of discharge. Here C-rate was defined based on a 1710 mAh/g capacity for SiO and FP-SiO.

3.3 Results and Discussions

Figure 3.1(a) shows the discharge capacity of SiO electrodes made with different molecular weight NaPAA binders. The first cycle voltage curve of these electrodes is shown in Figure 3.2. Except for the electrode with the highest molecular weight binder
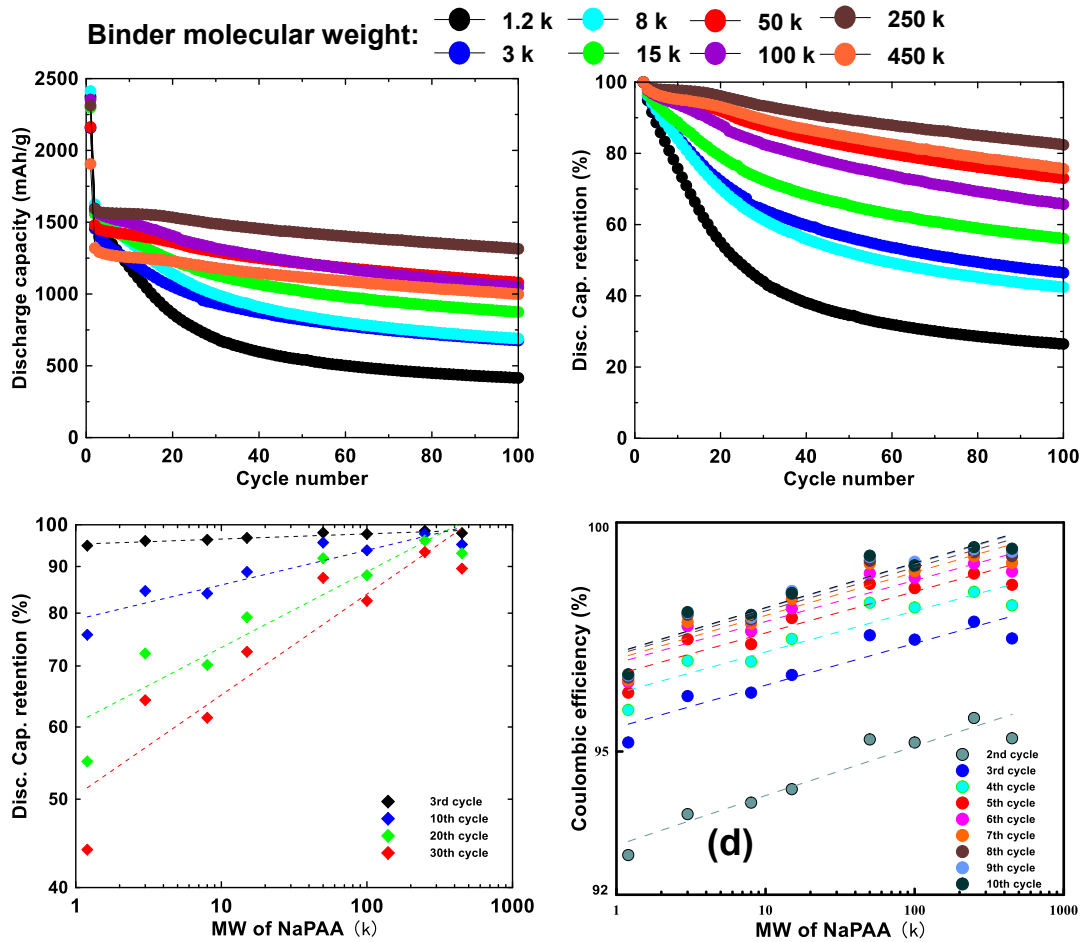
Figure 3.1   Electrochemical performance of SiO electrodes made from water-based slurries using NaPAA binders with different molecular weights: (a) discharge capacity, (b) discharge capacity retention, (c)discharge capacity retention at different cycles, and (d) CE.

(450 k), the initial lithiation and delithiation capacities are about 2300 mAh/g and 1500

mAh/g, respectively, with a random variation in the reversible capacity of about ± 5%.

This behaviour is typical for SiO, which has a large irreversible capacity due to the
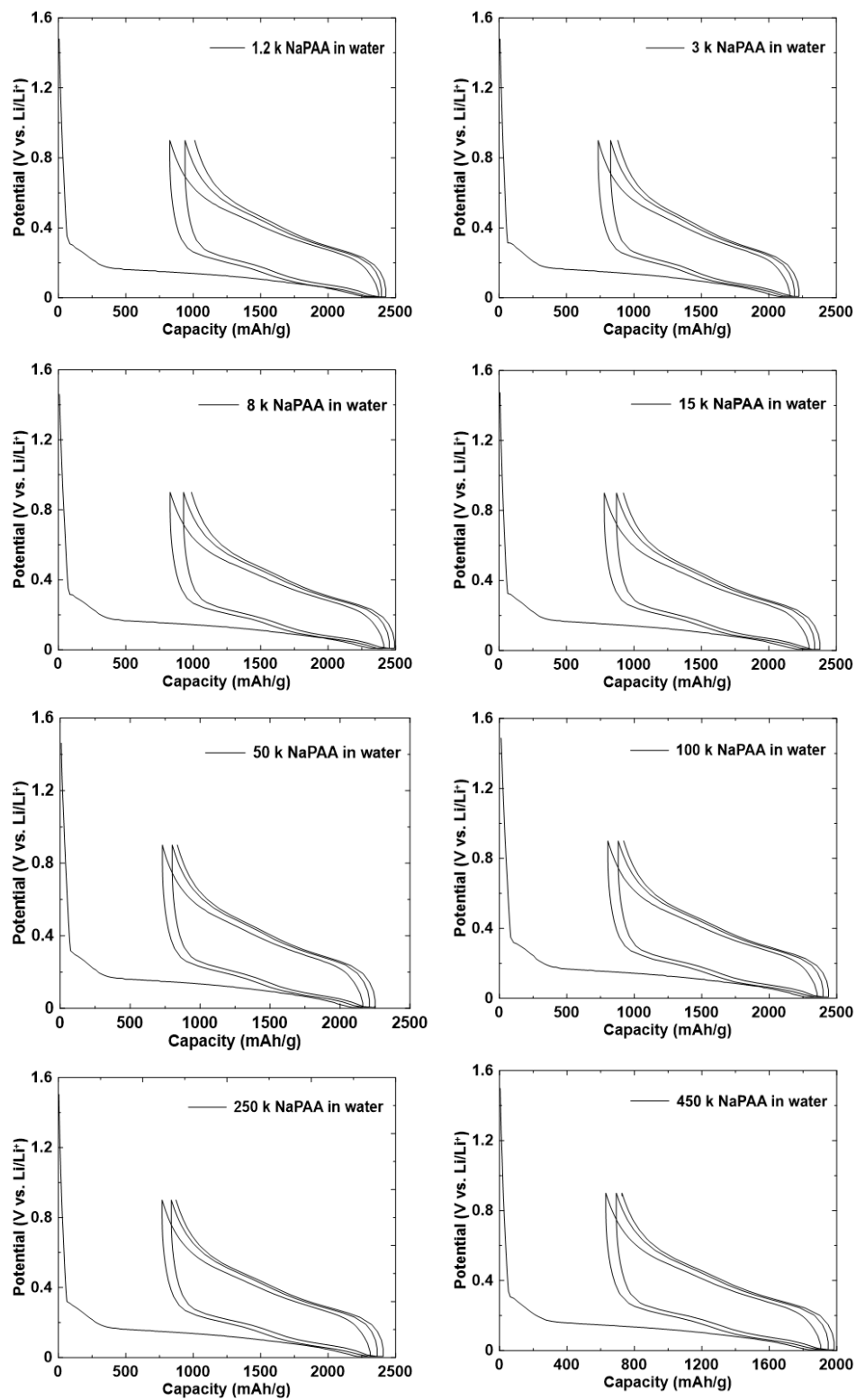
Figure 3.2   Voltage curves of SiO electrodes made in water-based slurries with different molecular weight NaPAA binders.

irreversible formation of lithium silicates during its initial lithiation. The initial

lithiation and delithiation capacities of the electrode with 450 k NaPAA binder are much lower than the others (~1900 mAh/g and 1300 mAh/g, respectively). This is likely due to the high viscosity of this slurry, which made mixing less efficient, resulting in a poorer dispersion of the electrode components.

Figure 3.1(b) shows the discharge capacity retention of the SiO electrodes normalized to their second discharge capacity, so that the capacity retention of the electrodes can be directly compared. Despite some variation, there is a general trend that capacity retention improves with increasing MW. This can be seen in Figure 3.1(c), which shows the capacity retention at different cycles plotted as a function of the NaPAA binder MW on a log-log scale. According to Figure 3.1(c), the logarithm of the discharge capacity retention has approximately a linear dependence on the logarithm of the NaPAA binder MW at any cycle number. In other words, the relationship between the discharge capacity retention and the binder MW approximates a power law. It can also be seen that the dependence of the capacity retention with binder MW becomes more pronounced as the cycle number is increased. It is well known that the viscosity of polymer solutions also depends on polymer MW with a power law relationship.[73] Therefore, Figure 3.1(c) is suggestive that the discharge capacity retention dependence on MW is due to changes in the electrode slurry viscosity. It will be shown below that this is indeed the case. Figure 3.1(d) shows the coulombic efficiency (CE) for different cycle numbers plotted as a function of binder MW on a log-log scale. As can be seen in this figure the CE also approximately has a power law dependence on the binder MW, which is also suggestive that the CE of these electrodes is related to slurry viscosity.

The reason why the viscosity of the slurry can have an impact on electrode capacity

fade and CE during cycling is illustrated in Figure 3.3, which shows an image of the electrode prepared with the lowest MW NaPAA binder. Areas of dried binder on either side of the electrode coating are evident where the binder has seeped from the coating. In some areas, this seepage has also drawn out some of the solid particles to either side of the coating. This behavior results in binder loss from the electrode. Insufficient slurry viscosity can also cause active particles to settle, resulting in uneven active loading and the segregation of active materials and carbon black. Figure 3.4 shows the results of viscosity measurements of NaPAA aqueous SiO slurries with different MW binders. The slurries were transferred from the mixing device immediately to the sample container of viscometer. The initial viscosity measurement data points are shown in Table 3.2. Because the slurry would be cast right after mixing, the initial measurements in the first 10 minutes are more important than the rest of the data, which can be affected by shear thinning, particle settling, and increases in temperature due to friction created by the rotating spindle during the viscosity measurement. These effects are apparent in the decreasing over time as shown in the viscosity vs. time plots of Figure 3.4. The viscosity of the slurries with 1.2 and 3 k NaPAA binder was so low that particle settling from the slurry was observed. Slurry viscosity increased when higher MW binders were used and no particle settling was observed for slurries with higher MW binders. The 450 k NaPAA slurry viscosity was so high that it was out of range of the viscometer. From these results, a viscosity of at least 200 cP was required to maintain a stable slurry without particle settling.

Figure 3.3   A picture of the coating made from SiO from a water-based slurry with 1.2k NaPAA.

Table 3.2 Initial viscosity measurement data points

MW	1.2 k	3 k	15 k	50 k	100 k	250 k
Viscosity (cP)	24.1	27.5	185.6	195.5	263.7	206.8
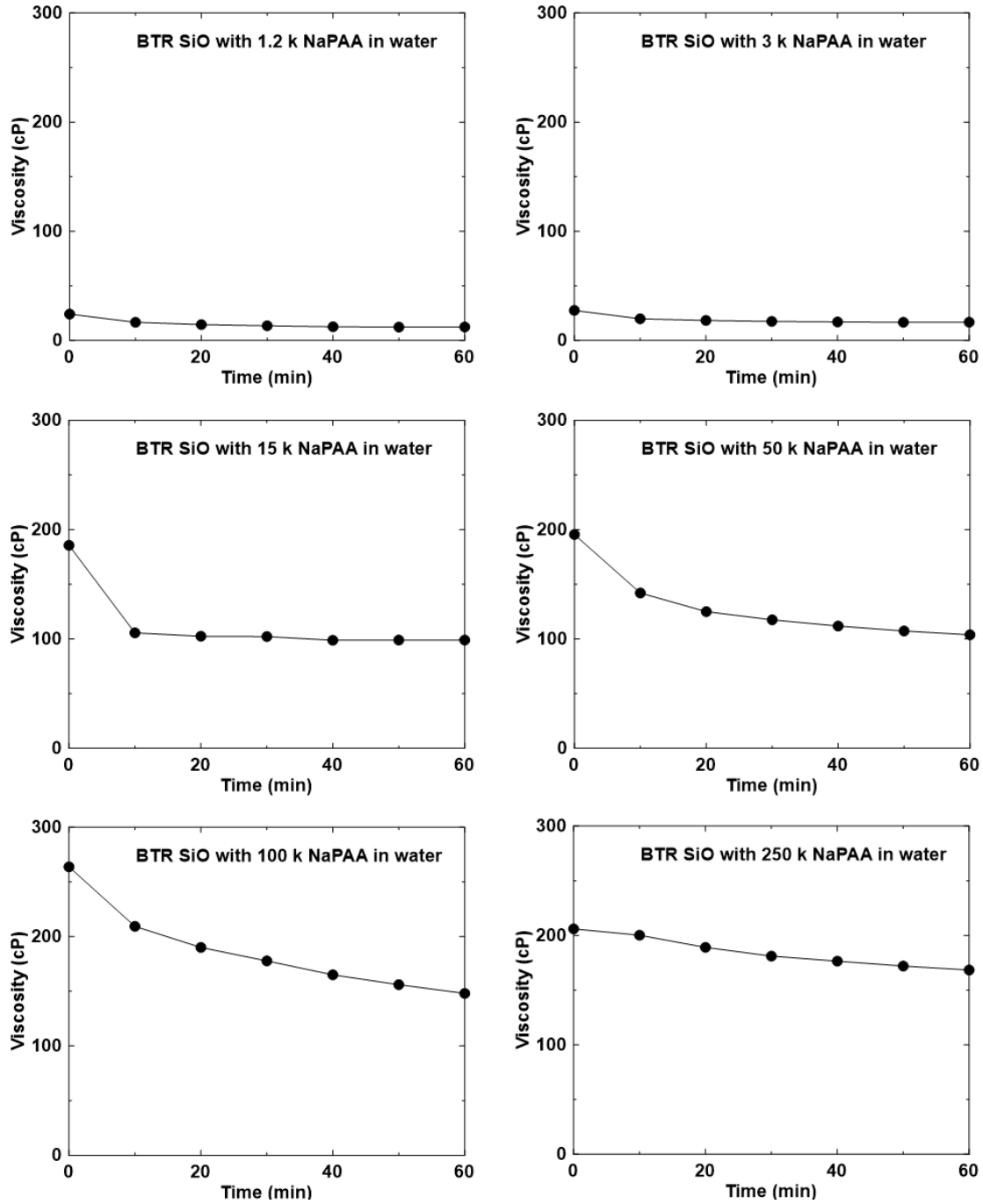
Figure 3.4   Viscosities of SiO slurries made from water-based slurries with different MW NaPAA binders.

It is not known from the above results if the poor performance of electrodes with low MW binders is solely from the effects of low viscosity slurries or if the binder MW has additional contributions to cycling performance. One way of reducing the effect of slurry viscosity is to reduce the active particle size. Therefore, the same water-based slurry formulations binders were utilized to make a series of electrodes with different MW NaPAA binders and FP-SiO as the active material. Particle size reduction improves the distribution of the active phase by reducing settling. As a result, issues with uneven active loading and the segregation of active materials and carbon black seen during the coating of SiO electrodes with low MW binders were avoided with the FP-SiO coatings. Figure 3.5 shows the discharge capacity of these electrodes for 200
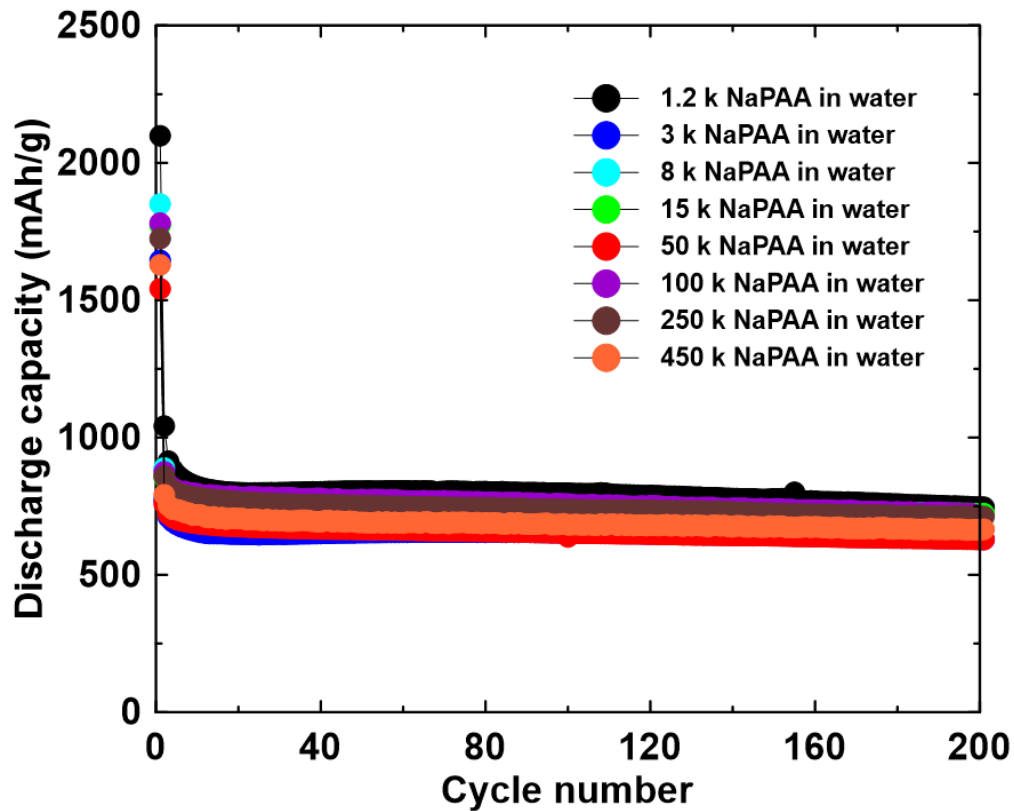
Figure 3.5   Discharge capacity of FP-SiO electrodes made from water-based slurries using NaPAA binders with different molecular weights.

cycles in half cells. After simple ball milling to make FP-SiO, the reversible capacity of SiO was reduced to about 700 mAh/g and severe capacity loss occurred over the first 10 cycles. This is because the surface area increased from 2.318 m^2/g for SiO to 16.497 m^2/g for FP-SiO. The higher surface area FP-SiO would require more binder to efficiently cover the particle surfaces. Therefore, the FP-SiO electrodes are starved of binder, resulting in the loss of active material. Nevertheless, after the initial 10 cycles no obvious capacity fading was observed for all NaPAA molecular weights. This suggests that the binder MW may not play a large role in capacity retention, if particle settling/segregation is addressed. Nevertheless, reducing active material particle size is not a good way to achieve this, since it leads to binder starvation. It also leads to higher
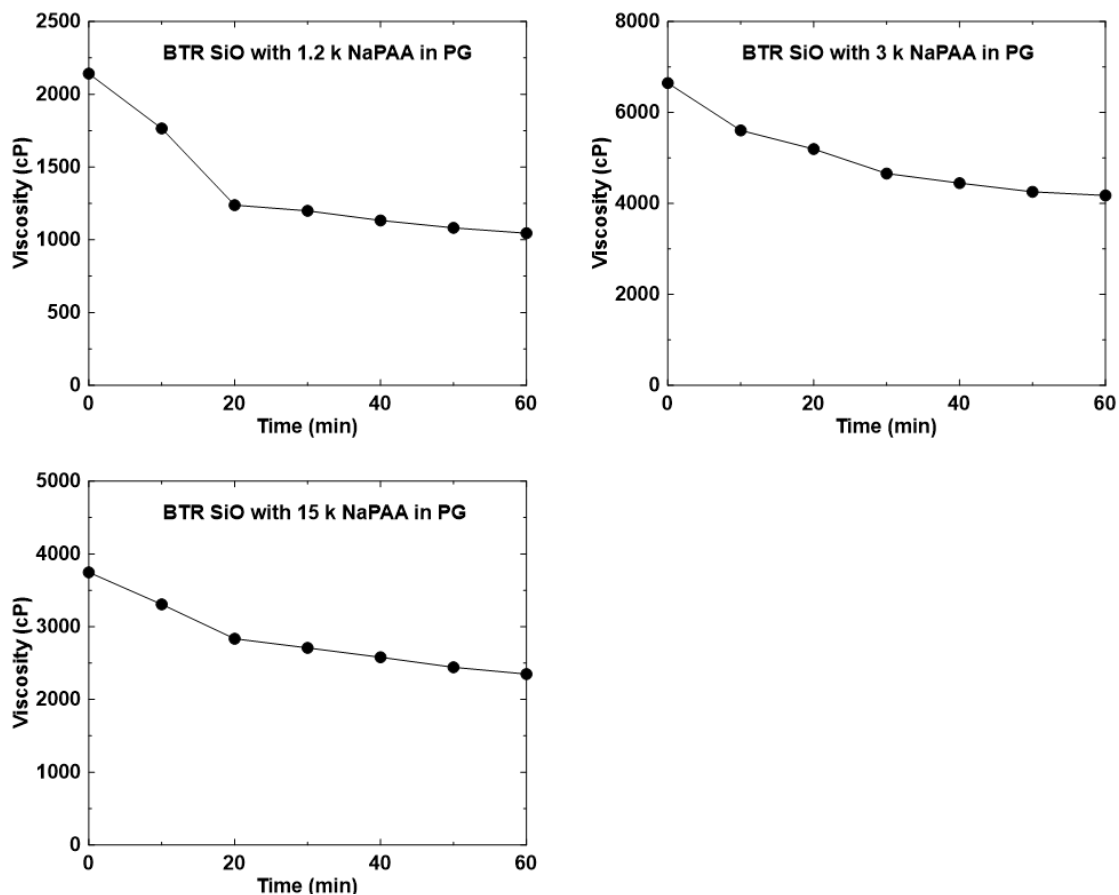
Figure 3.6   Viscosities of SiO slurries made from PG-based slurries with different MW NaPAA binders.

surface area, which is known to increase reactivity with electrolyte.

In order to increase the viscosity of slurries with low MW binders (1.2, 3, and 15 k), while maintaining the same electrode formulation and utilizing the large SiO particles, propylene glycol (PG) was used as the slurry solvent. It was not possible to use PG with higher molecular binders since the viscosity of the slurries became too high for efficient mixing and coating. The advantage of using PG is that it evaporates during the electrode drying process and therefore does not affect the final electrode. composition. Figure 3.6 shows the viscosity of PG-based SiO electrode slurries. The as-prepared PG slurry viscosities with the low MW NaPAA binders are much higher than the water-based slurries and well exceed the slurry viscosities required to keep the SiO particles in suspension (by about 20-40X).

For coatings made from the PG-based slurries, it was found that the CB tended to segregate to the top of the electrode coating during the drying process. This is illustrated in Figure 3.7(a), which shows an SEM image of the top surface of a PG-based SiO electrode after drying in the conventional horizontal orientation. Because of CB segregation, large amounts of CB are seen at the top surface. In order to get a
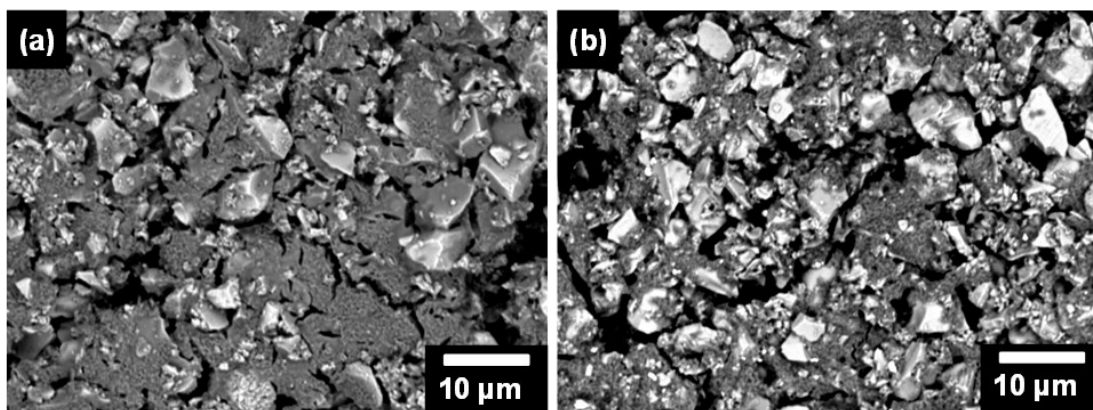
Figure 3.7   BSE images of the top view of SiO electrodes made from PG-based slurries with 1.2k NaPAA binder utilizing (a) horizontal drying and (b) vertical drying.

homogeneous distribution of the solids, PG-based coatings were positioned vertically during the drying process. Figure 3.7(b) shows the top surface of a PG-based coating dried vertically. The CB and SiO particles are now distributed homogeneously.

Figure 3.8(a) shows the capacity vs. cycle number of SiO electrodes made from PG-based slurries with low MW NaPAA binders compared to SiO electrodes made from water-based electrodes with high MW NaPAA binders. Compared to their water-based counterparts, electrodes made from PG-based slurries have much improved performance. For instance, the capacity retention of the SiO electrode made with 1.2 k NaPAA increased from 27% to 91%. Figure 3.8(b) compares the capacity retention of these electrodes with respect to the second cycle. The capacity retention of all the SiO
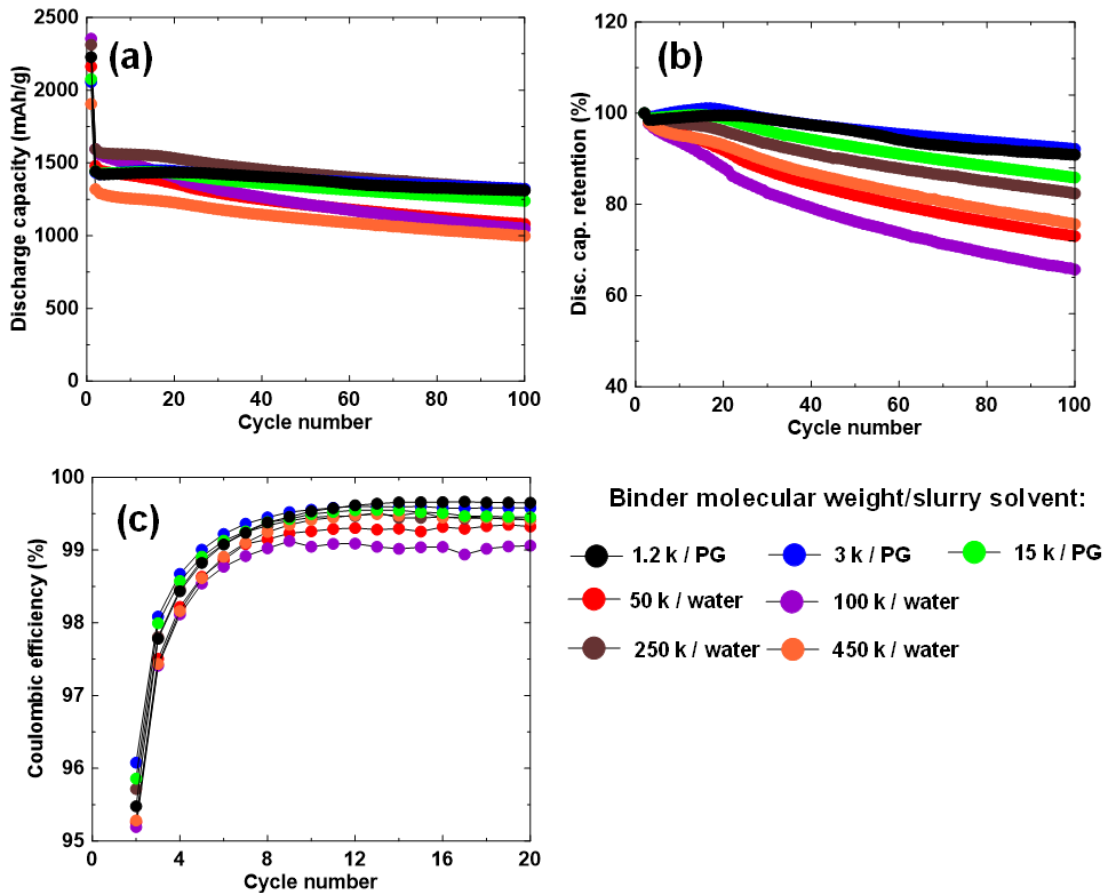
Figure 3.8   (a) Discharge capacity, (b) capacity retention, and (c) coulombic efficiency of SiO electrodes made from PG and water-based slurries with different MW NaPAA binder.

electrodes made from low molecular weight PG-based slurries now even exceed capacity retention of the best SiO electrode (250 k NaPAA) made with a water-based slurry. The coulombic efficiency of the SiO electrodes made from PG-based slurries with low MW PG-based binders is also the highest amongst all the SiO electrodes, as shown in Figure 3.8(c).

The above results show that when a high NaPAA binder solution viscosity is maintained, the binder MW has very little impact on the cycling of electrodes with Si-based anodes. In fact, the highest capacity retention and CE were obtained for the lowest MW NaPAA binder when the binder solution viscosity was kept high. Therefore, the function of this binder in providing an artificial SEI layer and maintaining particle connectivity during cycling is primarily due to the binder chemistry and not its MW. This is consistent with previous results that show that good cycling can be obtained with Si-based anodes even when single molecules are used as binders, like citric acid.[38] Here it is additionally demonstrated that a high binder solution viscosity may be maintained independent of the binder MW. This separation of binder solution viscosity from MW could provide enormous flexibility in electrode design, since it enables small MW binders and single molecules to be practically utilized as binders while maintaining slurry viscosities that are compatible with commercial electrode coating methods.

3.4   Conclusion

In this study, NaPAA with MWs ranging from 1.2 - 450 k were evaluated as binders for SiO electrodes prepared from water-based slurries. The capacity retention and CE

of these electrodes were poor for low MW binders but improved with increasing binder MW. This improvement in capacity retention and CE with binder MW was found to have a power-law like dependence, which suggests that they were related to binder solution viscosity. To increase the viscosity of the low MW NaPAA solutions, PG was utilized as the slurry solvent. This resulted in good cycling performance being obtained for SiO anodes, regardless of the NaPAA binder MW. In fact, the best cycling performance was obtained for an electrode prepared from a PG-based slurry utilizing the lowest binder MW.

It is well known that binders play two roles in Si-based anodes: establishing good slurry characteristics (good particle dispersion and a good rheology) and maintaining good electrode cycling performance (creating an artificial SEI and maintaining particle connectivity during cycling). By utilizing PG to fulfill the first role, this study shows that these two roles are essentially independent of each other. The use of viscous slurry solvents, like PG, could therefore enable researchers to focus on binder molecules that are specifically designed to improve cycling without also needing to serve as a slurry rheology modifier. This provides an enormous space for binder chemistry exploration that could lead to higher performance and lower cost binders.

CHAPTER 4   NANO-Si FILLED GRAPHITE PARTICLES BY MECHANOFUSION[b]

4.1   Introduction

The development of high-energy-density lithium-ion batteries is significantly important. Graphite is the most widely used active material for lithium-ion battery anodes. Compared with graphite (LiC_6, 890 Ah/L), silicon has a much higher volumetric capacity ($Li_{15}Si_4$, 2194 Ah/L).[74] In order to develop next-generation lithium-ion batteries, silicon-based negative electrode materials have been widely studied recent years, however fundamental challenges hinder their implementation. One of these key challenges is volume expansion. During lithiation and delithiation, silicon experiences huge volume changes (280%).[14] Repeated expansion and contraction of Si during lithiation and delithiation can result in particle pulverization due to the resulting stress and strain. For the whole electrode structure, this volume expansion can destroy the electrode's integrity and therefore electrical connection amongst active particles and the current collector can become lost.[38] It has been reported that nano-sized silicon can release the internal stress from expansion and so avoid particle fracture.[15] However,

---

nanoparticles have a large surface area which is not desirable as it may increase reactivity with electrolyte. Another issue is also due to the volume change of silicon, it is hard to form a stable solid electrolyte interphase (SEI) on the surface of Si-based anode materials. Particle pulverization and damage to the SEI can lead to continuous side reactions at the silicon/electrolyte surface, causing the SEI to grow. The resulting thick SEI layer can cause high polarization and lithium loss and accelerate cell failure.[75]

To address these challenges, a strategy of combining silicon with graphite or carbon has been investigated for a long time. A simple blend of silicon and graphite does not work well because the Si component of the electrode still has the issues associated with volume expansion coupled with electrolyte reactivity.[23] Instead Si-C composite materials have been used. As an example, Chao Li et al employed rotary spray drying to make silicon-carbon nanotube spherical composites.[76] The prepared material showed 2500 mAh/g capacity after 500 cycles. As another example, Minseong Ko et al synthesized silicon nanolayer embedded graphite composites via chemical vapor deposition (CVD).[77] A thin layer of amorphous silicon layer was deposited onto and within porous graphite particles, followed by the deposition of a carbon overlayer. By this method, a silicon layer was deposited both on the outside and inside surfaces of spherical graphite, which significantly improved energy density. Applying the final carbon coating resulted in good cycling performance. It is well known that applying carbon-coatings onto Si-based anode materials can enhance electric and ionic conductivity and help maintain a stable SEI layer.[78,22,79]

Mechanofusion (MF) processing, developed in Japan in the 1980s, is a common method used on a large scale to create composite particles.[79,80] In this method particles

are exposed to high shear and compaction forces. During processing, no significant impact forces occur. MF not only can coat fine particles onto coarse powders but also can cause fine particles to become embedded within course particles. In previous publications, we described the use of MF to embed guest Si-alloy particles into porous graphite host particles for the preparation of silicon alloy/graphite composite anode materials.[79] Some of the resulting composites achieved, 950 mAh/g (1437 Ah/L) at 2C rate and a capacity retention of 95%/100 cycles. To accomplish this, the particles required carbon coating to protect the guest Si-alloy particles from exposure to electrolyte. Despite these promising results, the guest alloy particles were only partially embedded. This is because they had a large size distribution, resulting in many guest particles being too large to be embedded. The critical size for embedding was found to be 1 μm, with any particles larger than this remaining on the surface of the graphite.[81]

In this study, a silicon/graphite composite is synthesized by embedding fine Si guest particles into cavities within graphite particles via mechanofusion. The Si guest particles utilized are all below the critical embedding size, to ensure more complete embedding. In addition, pure Si rather than a Si alloy was used, so that a higher capacity could be achieved with less guest particles.

4.2   Experimental

Material synthesis

A disperse nano silicon (n-Si) powder was made by ball milling 2 g of a mixture of 95 wt % n-Si (300 nm, 99%, SkySpring Nanomaterials, Inc.) and 5 wt % stearic acid (95%, Sigma-Aldrich) with 180 g of 0.125" stainless steel balls in a 65 mL hardened steal vial

with a high energy ball mill (SPEX 8000). This milling step broke up aggregates of n-Si powder in the as-received sample. The stearic acid served as a dispersant during the milling and MF processes. After ball milling, the dispersed n-Si product was recovered from the milling media by ethanol washing. This produced an ethanol slurry, which was separated from the milling media by sieving. Finally, the ethanol was evaporated from the slurry at 120 °C overnight in air, leaving behind the dispersed n-Si powder. To embed 5 wt % n-Si in graphite, 1.385 g dispersed n-Si and 25 g natural spherical graphite (A3901, Asbury Carbons) were processed in a mechanofusion machine (Dry Particle Fusion Machine, DPM Solutions, Hebville, NS) with a 7.66 cm diameter chamber at 3000 rpm with a 1.0 mm press head gap and 0.5 mm scraper gap. The silicon-graphite composite product after 5 hours of mechanofusion processing is referred to here as Si@Gr.

Carbon coating by chemical vapor deposition (CVD) was conducted in a custom-made CVD system as described in Reference 22.[22] Briefly, the powder is placed in a rotating quartz tube with inner opposing screws, which maintains a fluidized bed while keeping the powder sample in the center of the reaction zone in the tube. The rotating tube is heated with a laboratory tube furnace. For CVD carbon coating in this study, about 9 g of Si@Gr was placed in the rotating tube, which was heated to 800 °C in argon atmosphere. The gas was then changed to ethylene at an 80 cc/min flow rate and the sample dwelled at 800 °C for 3 hours. The gas was then changed back to argon and the sample was allowed to cool to room temperature.

Carbon coating under hydrothermal (HT) conditions was conducted in an autoclave, using a method described in a previous study (the manuscript is in preparation). In this

study,140 g deionized water, 10 g α-D-Glucose (anhydrous, 96%, Sigma-Aldrich) as a carbon source, 10 g isopropanol alcohol and 8 g Si@Gr were placed in a mini bench top hydrothermal reactor (Model 4560, Parr Instrument Company). The mixture was heated at 250 ℃ for 3 hours while being stirred by a magnetic driven impeller at a speed of 250 rpm. After the product was cooled down, the slurry was washed with ethanol three times by suction filtration, dried at 120 ℃ in air overnight, and then heated at 800 ℃ in argon for 3 hours.

Thermogravimetric Analysis

Thermogravimetric analysis (TGA) measurements were conducted with a SDT Q600 V20.9 Build 20 DSC-TGA analyzer. Oxygen was used as the gas flow. Samples were heated from 20 °C to 800 °C with a scan rate of 10 degrees per minute.

Electrode coating

Electrode slurries were prepared by mixing 0.6300 g of the silicon/graphite composites, 0.0350 g of carbon black (super C65, Imerys Graphite and Carbon) and 0.0350 g of polyvinylidene fluoride (MW ~534000, Sigma-Aldrich), (corresponding to a mass ratio of 90:5:5) in N-methy2-pyrrolidone (Sigma-Aldrich, anhydrous 99.5%), which was utilized in an amount required to obtain an appropriate viscosity for coating electrodes. All slurries were mixed for 20 minutes with a 1" (2.54 cm) diameter Cowles blade at 5000 rpm and then spread onto a copper foil (Furukawa Electric, Japan) with a 0.008" (0.2 mm) coating bar. The coatings were dried in air for 1 hour at 120 °C and then cut into 1.3 cm^2 disk electrodes.

Material and electrode characterization

X-ray diffraction patterns were collected with a Rigaku Ultima IV diffractometer using Cu k_α radiation in 0.05° increments. True densities were measured with a He gas pycnometer (|Q|Pyc, InstruQuest). The specific surface area was determined by the multi-point Brunauer-Emmett-Teller (BET) method using a Micromeritics Flowsorb II2300 surface area analyzer. Electrode cross sections were cut with a JEOL cross-section polisher (JEOL, IB-19530CP). Sample and cross-section images were observed with TESCAN MIRA3 scanning electron microscope (SEM).

Electrochemical characterization

Electrodes were assembled in 2325-type coin cells with lithium foil (Aldrich 99.9%) as a counter/reference electrode. One layer of microporous separator (Celgard 2300) and a blown microfiber membrane (3M Company) were used as separators. 1 M $LiPF_6$ (BASF) dissolved in ethylene carbonate (EC, BASF), and diethyl carbonate (DEC, BASF) (2:1 by volume) was employed as electrolyte. Before cell making, electrodes were dried at 120 °C in vacuum overnight. Coin cell assembly was carried out in an argon-filled glovebox. Cells were cycled between 5 mV to 0.9 V using a Neware 4000 test system at a temperature of 30.0 ± 0.2 °C. Cells were held at constant potential at the end of each discharge (lithiation) half-cycle until a lower current limit was reached to simulate constant current-constant voltage (CCCV) cycling. For the first cycle, the cells were discharged to 0.5 mV at 1/20 C with a 1/40 C lower current limit at the end of discharge and then charged to 0.9 V at 1/20 C. For subsequent cycles, the cells were

charged and discharged at 1/5 C with a 1/20 C lower current limit at the end of discharge. Here C-rate was defined based on a 3579 mAh/g capacity for Si and a 372 mAh/g capacity for graphite.

4.3   Results and Discussion

Figure 4.1(a) shows an SEM image of unprocessed graphite particles. The particles are rounded and are about 10 μm in size. On the surface of the particles individual graphite plates can be observed. A cross section of the particles, shown in Figure 4.1(b), reveals that the particles contain significant cavities. These cavities can account for 50%
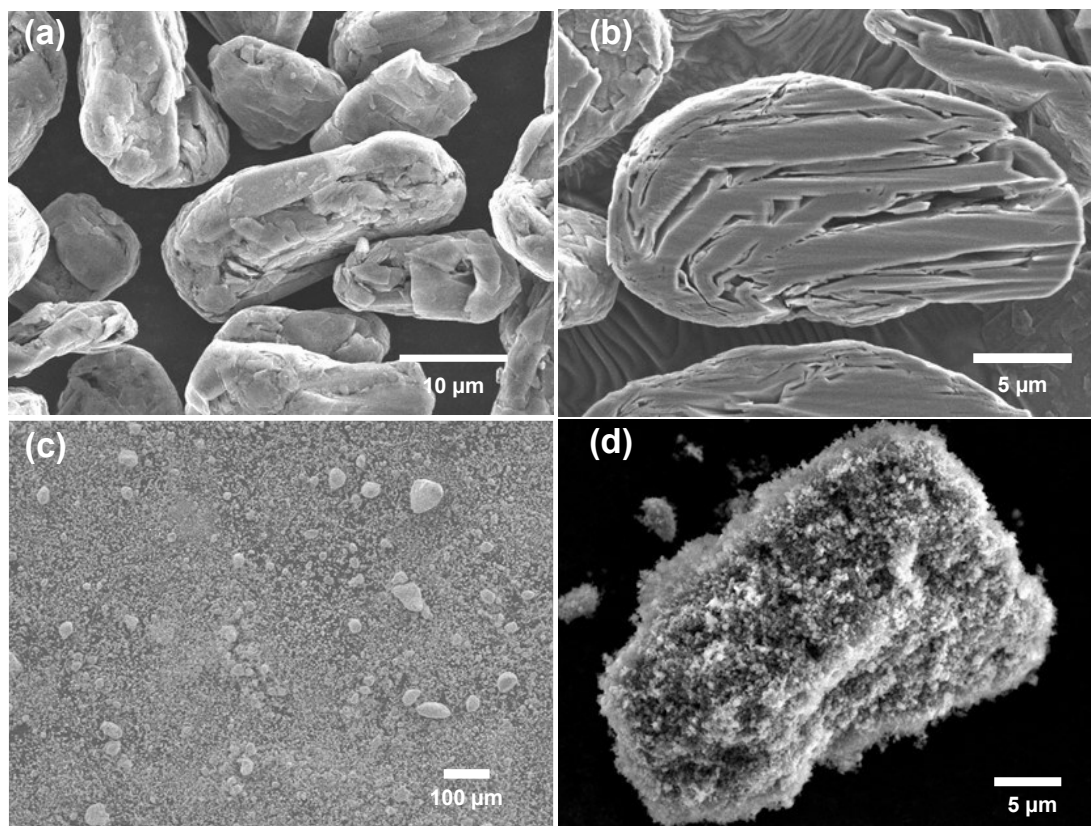
Figure 4.1   SEM images of (a) pristine graphite particles, (b) a cross-section of pristine graphite particles, (c) as-received nano silicon, and (d) ball-milled silicon.

or more of the particle volume. The particles appear to be made up of sheets of graphite that are curled up. This morphology and the resulting large cavity volume is likely a consequence of the spheronization process used to make these particles from natural graphite. As a result of this morphology, this graphite has a rather large BET surface area of 4.962 m^2/g, which is also indicative that many or most of the cavities are accessible to gas adsorption from the outside of the particle. We chose this graphite as a host for n-Si embedding because of this large accessible cavity volume.

Figure 4.1(c) shows an SEM image of the as received n-Si. It consists of small ~300 nm Si particles that are aggregated together into up to 80 μm secondary particles. The surface area of n-Si is 28 m^2/g. If this material was used directly for mechanofusion with graphite, the secondary particles densified and aggregated further, resulting in a mixture of graphite and dense n-Si secondary particles that are up to 50 μm in size, as shown in Figure 4.2. During this study, it was found that avoiding the aggregation of n-Si into large dense particles during mechanofusion with graphite represents one of the biggest challenges for embedding n-Si into graphite particles.
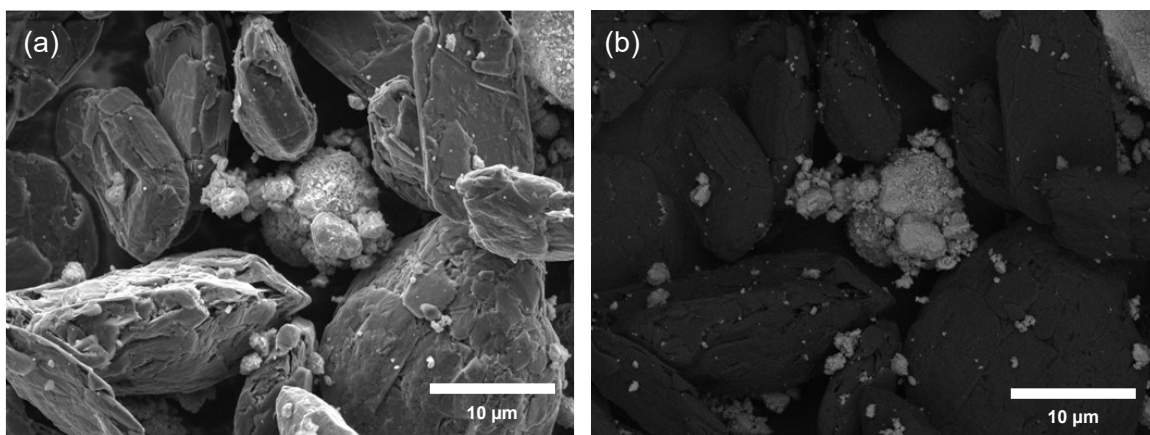
Figure 4.2   (a)SEM and (b) BSE images showing the results of directly mechanofusing n-Si and graphite.

Ball milling the n-Si with stearic acid as a dispersant, resulted in most of the

secondary particles being broken up into individual nanoparticles and secondary particles consisting of loosely aggregated nanoparticles, as shown in Figure 4.1(d). The ball milling process also increased the surface area from 28 m^2/g for unprocessed n-Si to 39 m^2/g for dispersed n-Si. As will be shown below, the dispersed n-Si can be successfully dispersed and embedded into graphite by mechanofusion without aggregating. Not using stearic acid as a dispersant resulted in n-Si aggregation. Therefore, the presence of stearic acid helps to avoid the aggregation of n-Si during mechanofusion.

Figure 4.3 shows how the dispersed n-Si/graphite mixture evolved during mechanofusion with processing time. After the first hour of processing (Figure 4.3(a)),
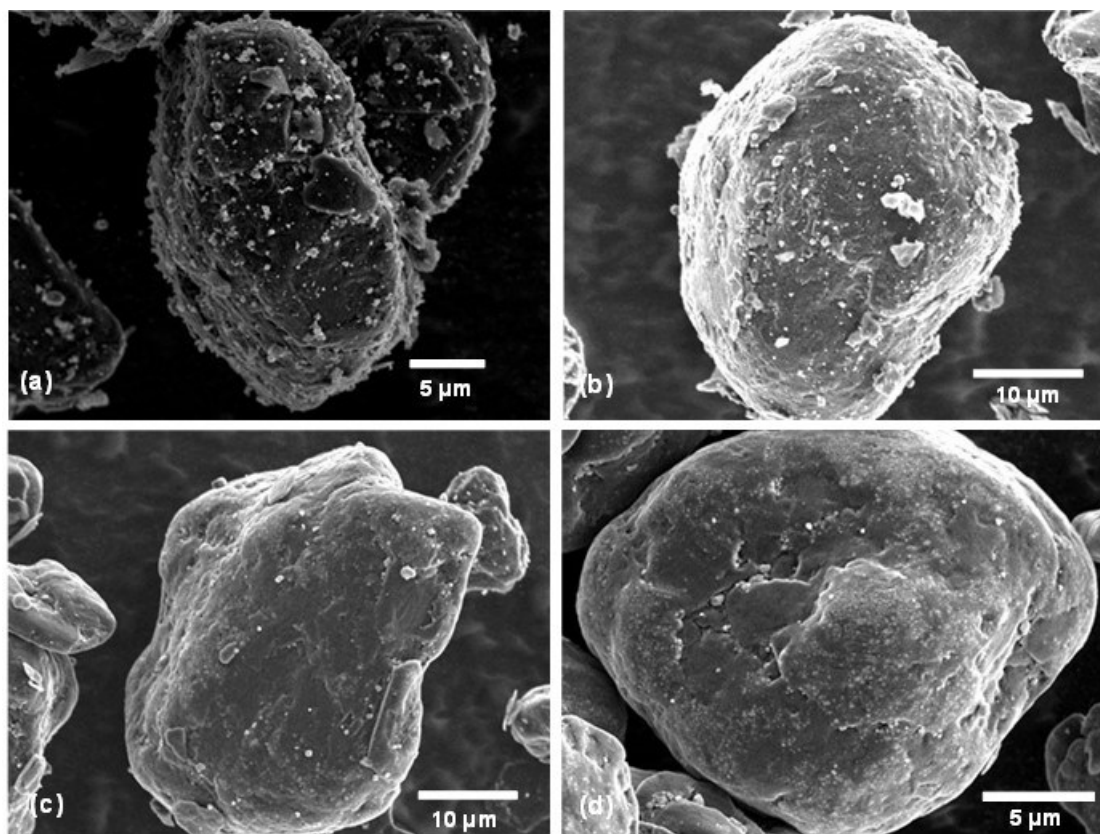
Figure 4.3   SEM image of (a) 1 hour, (b) 2 hours, (c) 3 hours and (d) 5 hours mechanofusion product.

the n-Si and graphite particles became well mixed, with the n-Si particles being relatively uniformly absorbed on the graphite surface. The shape of the graphite did not change. After 2 hours of processing (Figure 4.3(b)), the number of n-Si particles visible in the SEM images markedly decreased and the graphite surface started to be rounded. After 3 hours (Figure 4.3(c)), the graphite particle surface became smooth. Few n-Si particles can be observed on the graphite surface. Instead, some of the n-Si particles reside just under the graphite surface and are visible in these images as bright spots. With a further 2 hours of processing (Figure 4.3(d)), there was no further morphology change observed.

Figure 4.4(a-c) shows cross-section images of the final Si@Gr product. The cavities inside the graphite particles are filled with n-Si particles. However, some of the cavities
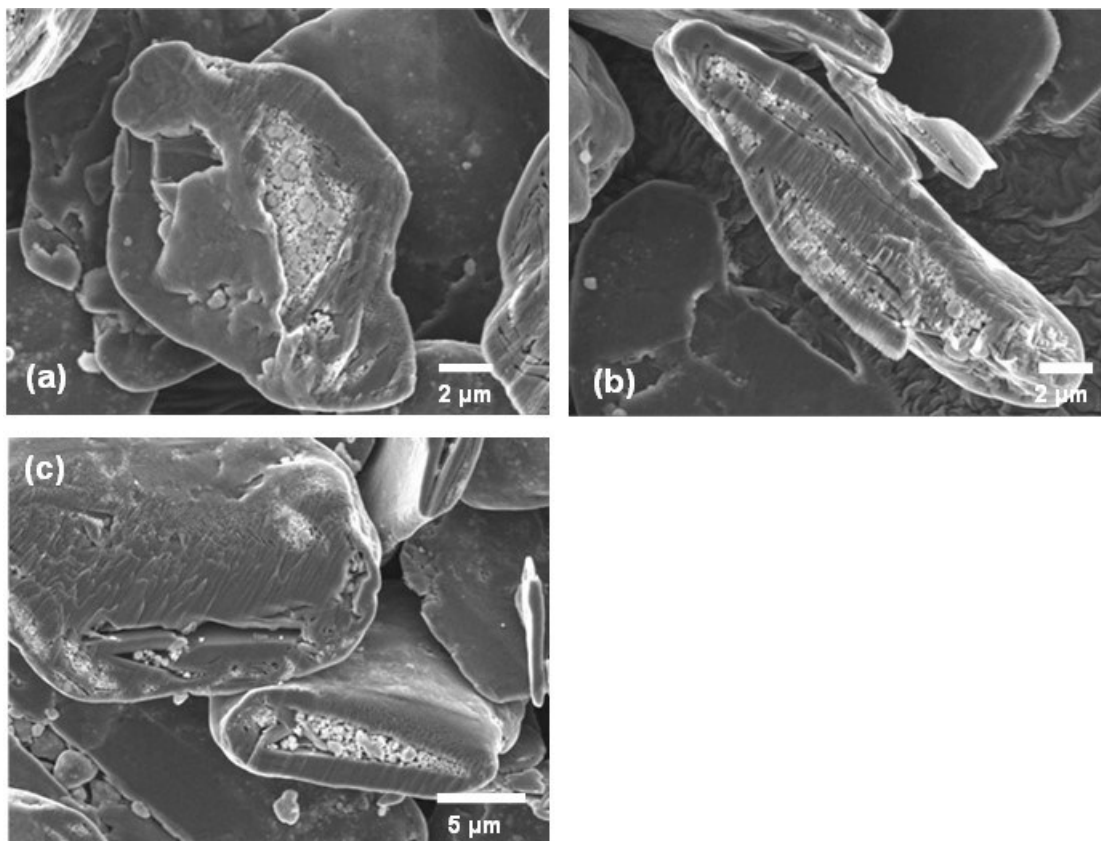
Figure 4.4   Cross-section SEM image of Si@Graphite.

remain empty. From looking at many particle cross-sections, it was observed that the filled cavities were often linked to a crack or fissure in the particle surface, while the empty cavities were never observed to have this property. From these observations, we suspect that all the empty cavities are not connected to the surface of the particles (inaccessible cavities), while all the filled cavities are in fact connected to a fissure on the particle surface (accessible cavities). It is not always apparent that accessible cavities are indeed accessible from SEM images since paths from the surface to the accessible cavities would not always be exposed by 2-dimensional cross-sections. As will be shown below, the results of carbon coating experiments confirm this model: all the n-Si filled cavities are accessible from the outside, while all of the empty cavities are inaccessible from the outside.

That only accessible cavities are filled provides an explanation for the embedding process. During mechanofusion the n-Si particles seem to behave essentially like a fluid and fill any empty cavities they have access to from the surface, without disturbing the graphite host. Therefore, ideal graphite particles for the synthesis of Si@Gr would be ones that have a large fraction of empty cavities and where a large fraction of these is connected to the surface by some channel or fissure. We have found that spherical natural graphite is excellent for this purpose since they have these qualities. Alternately, ideal guest particles need to be small enough to fit in the channels connecting the accessible cavities to the particle surface. From earlier experiments, we have found that guest particles need to be less than 1 μm in size to be able to be embedded in this type of graphite by mechanofusion, while guest particles larger than this remain on the graphite surface.[81] From these considerations, we believe that the ~300 nm size n-Si

guest particles coupled with the high void fraction spherical natural graphite used here represent an ideal combination for creating Si@Gr particles by mechanofusion.

As further confirmation that the MF processing did not affect the host graphite, XRD patterns of the dispersed n-Si, graphite, and Si@Gr product particles are shown in Figure 4.6. Si@Gr has the combined peaks of graphite and n-Si, while the crystalline structure of graphite after mechanofusion remained unchanged. The surface area of Si@Gr was also measured to be 7.513 m^2/g, which is close to the predicted value of 6.66 m^2/g according to a physical mixture of n-Si and graphite in a 5:95 weight ratio.

After mechanofusion processing some of the Si@Gr particles were carbon coated by CVD. This was done to close off the paths from the particle surface leading to
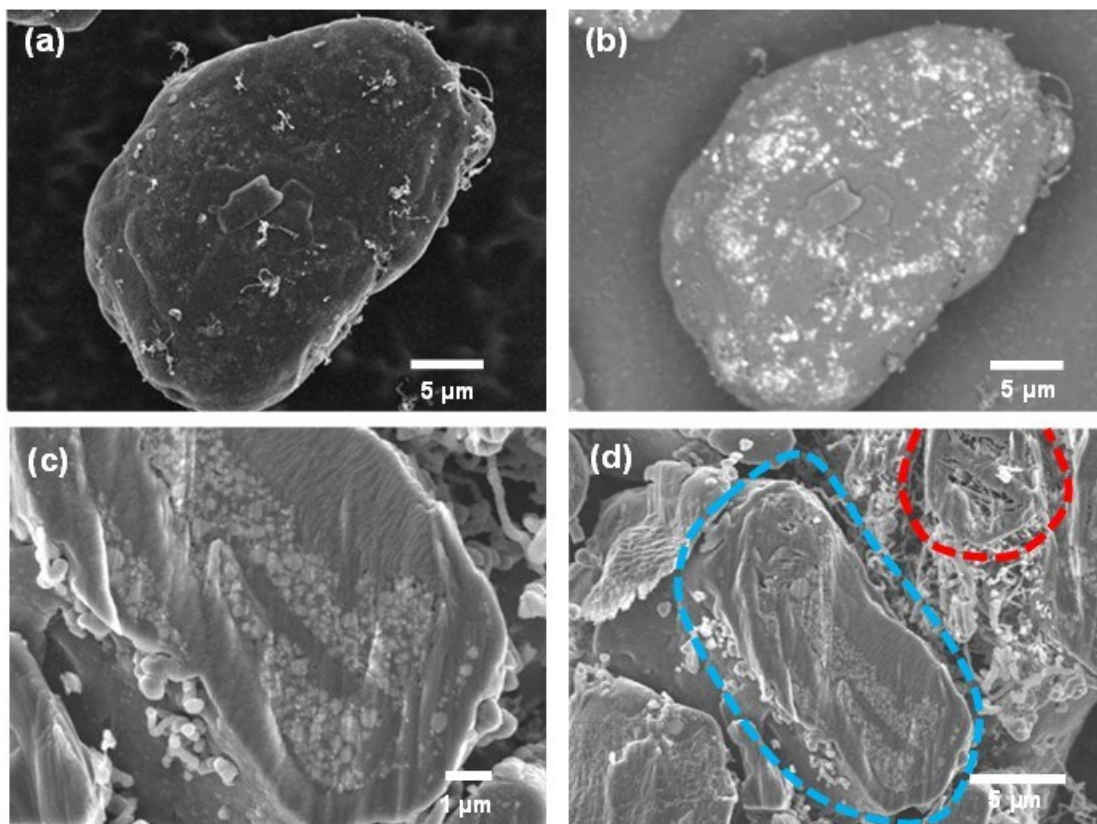
Figure 4.5   SEM images of CVD-Si@Gr composite particles: (a) and (b) show SE and BSE images of the same particle, (c) shows an SEM image of a cross-sectioned particle, and (d) shows cross-sectioned particles with accessible cavities (blue) and inaccessible cavities (red).

accessible cavities, to inhibit electrolyte from penetrating into these cavities and reacting with the n-Si during Li-ion cell operation. Figure 4.5(a) shows an SE SEM image of a Si@Gr particle after CVD carbon coating (CVD-Si@Gr). In comparison to Si@Gr, shown in Figure 4.3(c), the CVD-Si@Gr surface is smoother and fewer residual n-Si particles are visible on the particle surface. Some carbon fibers can also be seen on the surface of the particle that have grown on the surface during the CVD process. It is well known that transition metals catalyze carbon fiber growth under CVD conditions. The fibers observed here likely have grown from iron impurities that either originate from the ball milling process used to disperse the n-Si or the mechanofusion process itself. Figure 4.5(b) shows a BSE SEM image of the same particle. Using backscattered electrons, the subsurface n-Si particles can still be imaged, indicating that the carbon coating must be very thin. Despite the thin coating, the surface area of the CVD-Si@Gr particles has become greatly reduced (1.668 m^2/g) compared to the surface area of Si@Gr (7.513 m^2/g).

Figure 4.5(c) shows an SEM image of a cross-sectioned CVD-Si@Gr particle, which shows that the n-Si particles embedded within the graphite cavities were carbon coated by the CVD process. This shows that the ethylene gas can penetrate into accessible cavities, resulting in carbon deposition within these cavities during CVD processing. In comparison to the carbon coating on the graphite, which is too thin to be visible in the cross-section image, the carbon coating on the n-Si particles is much thicker, being about 200 nm - 400 nm in thickness. Apparently, the n-Si surface must catalyze the decomposition of ethylene more efficiently than the surface of graphite. As a result of the thick carbon coating on the n-Si surfaces, most of the accessible cavities

within the graphite particles containing embedded n-Si are essentially completely filled with n-Si and carbon. This large amount of carbon is apparent as low angle intensity in the XRD pattern of CVD-Si@Gr shown in Figure 4.6.
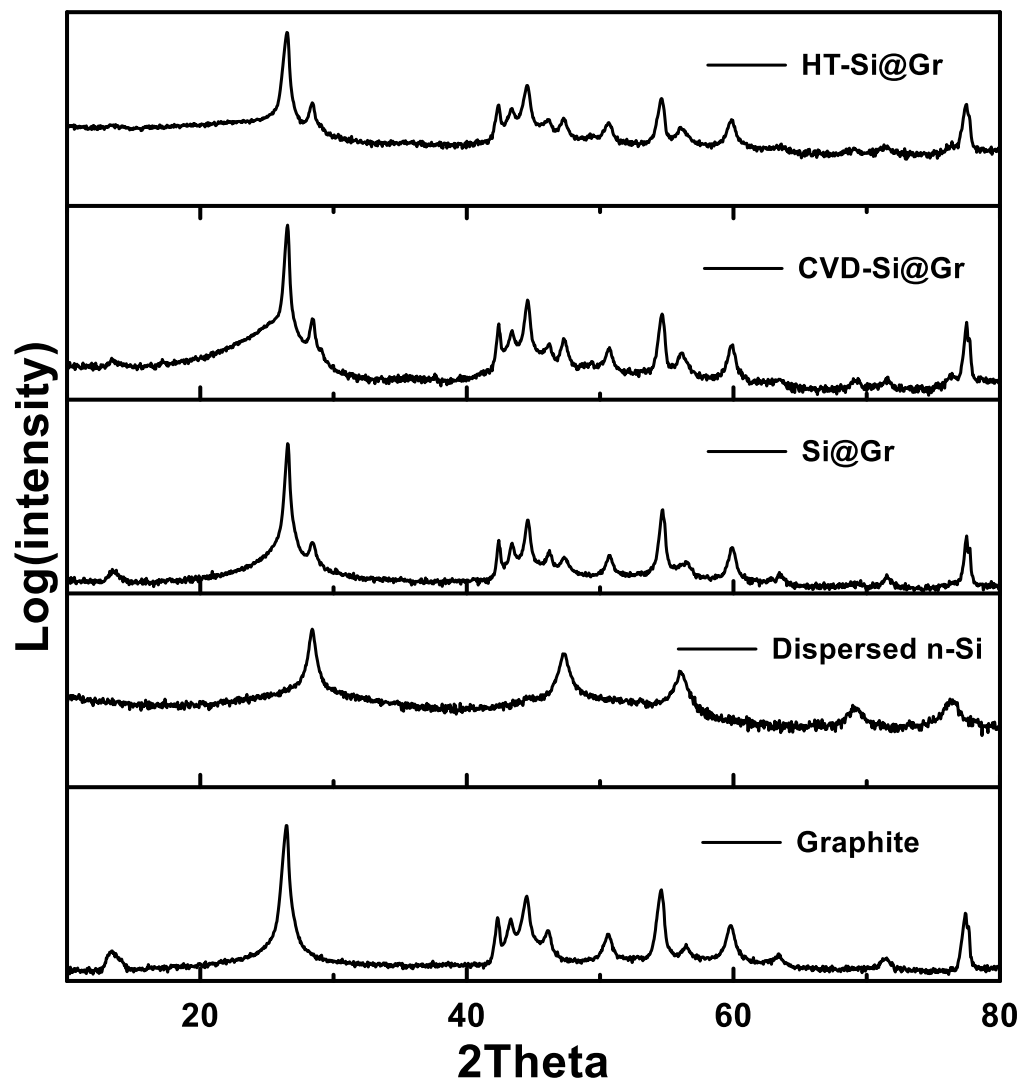
Figure 4.6   XRD patterns of graphite, dispersed n-Si, and Si@Gr composites.

The ability of the CVD process to fully coat the n-Si and essentially fill the accessible cavities explains the low surface area of the CVD-Si@Gr samples. In contrast to the accessible cavities, the inaccessible cavities remain unchanged after the CVD process, as shown in Figure 4.5(d), which shows an SEM image cross sectioned CVD-Si@Gr particle that contains accessible cavities and a CVD-Si@Gr particle

containing inaccessible cavities. The particle with accessible cavities is filled with n-Si, which are coated with carbon. The particle with inaccessible cavities is empty. Either the ethylene cannot access the inaccessible cavities or a carbon layer is also deposited in these cavities, but is too thin to detect.

Figure 4.7 shows an SE SEM image of a Si@Gr particle that was carbon coated by the hydrothermal method (HT-Si@Gr). This resulted in a much thicker carbon coating than what was obtained by the CVD process. As a result, few features from the original graphite surface are visible. In addition, almost no subsurface particles can be seen in BSE SEM images (as shown in the BSE image in Figure 4.7(b)). As shown in Figure 4.7(c), this thick carbon coating caused many of the particles to fuse together. Figure
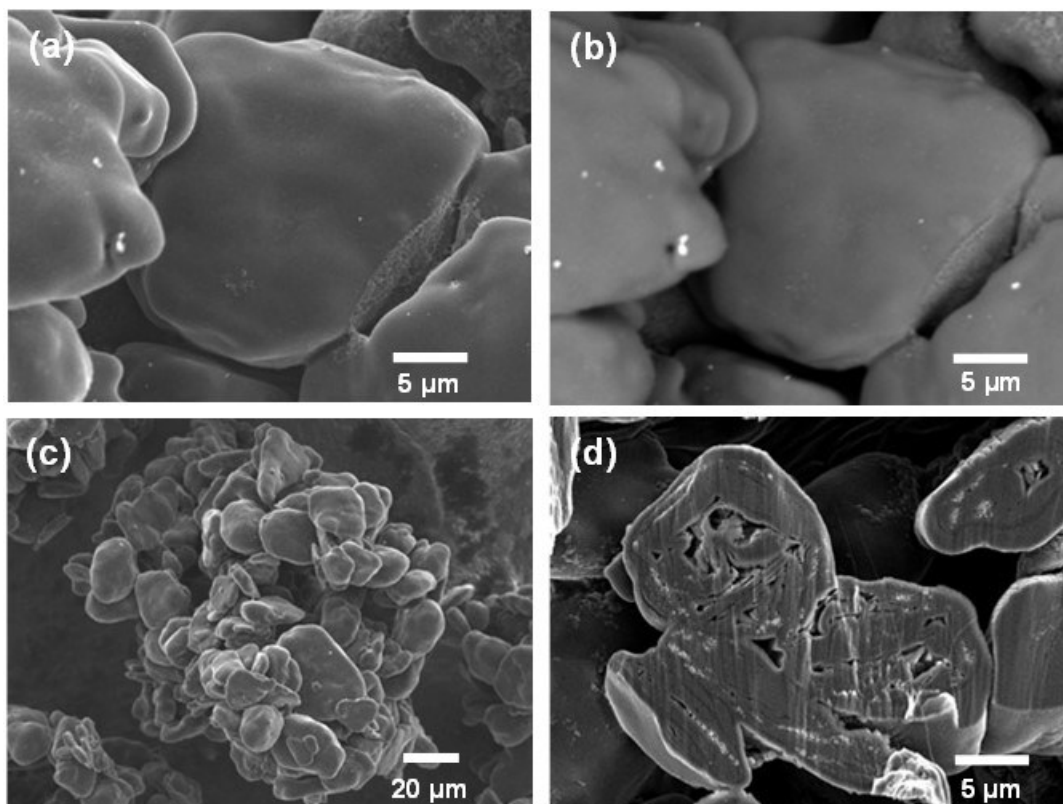
Figure 4.7   SEM images of HT-Si@Gr composite particles: (a) and (b) show SE and BSE images of the same particle, (c) shows an SEM image of a cluster of HT-Si@Gr composite particles, and (d) shows a cross-sectioned particle.

4.7(d) shows a cross-sectioned HT-Si@Gr particle. The carbon coating can be seen as a ~200 nm - 400 nm thick border surrounding many of the particles. As with the CVD-Si@Gr sample, most of the n-Si within the accessible cavities were carbon coated, showing that these cavities were also accessible to carbon deposition during HT processing. In contrast, the inaccessible cavities did not show evidence of carbon coating. This can be seen also in Figure 4.7(d), in which a particle with empty cavities showing no evidence of carbon coating is present. These observations confirm that all the cavities in Si@Gr particles that host n-Si are accessible to the outside of the particle, while all the empty cavities are inaccessible. The coating by hydrothermal method is not uniform. The particles in the center of Figure 4.7(d) have a thin layer while the particle at the top right corner has a thick coating. After hydrothermal treatment, the surface area increased to 56.64 m^2/g, due to the porous type of carbon that results from the HT coating process.

TGA measurements were made to determine how much carbon was deposited during the CVD coating process. The results of TGA measurements of the Si@Gr, CVD-Si@Gr, and HT-Si@Gr samples are shown in Figure 4.8(a), (b) and (c), respectively. The Si@Gr sample lost 89.34% of its mass after heating in air to 800°C
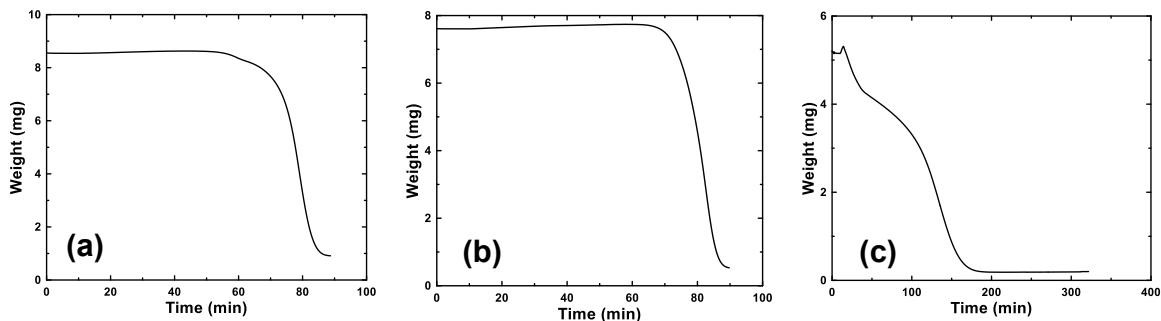
Figure 4.8   TGA results of (a) Si@Gr, (b) CVD-Si@Gr, and (c) HT-Si@Gr.

and then its mass became stable. This almost exactly corresponds to the expected net weight loss according to the full oxidation of Si@Gr into $CO_2(g)$ and $SiO_2(s)$. Assuming this full oxidation reaction, then according to the TGA results, the Si@Gr sample contained 4.97 wt. % Si, corresponding to the sample's designed 5 wt % Si content. In contrast, the CVD-Si@Gr sample lost 93.02% of its mass during heating to 800°C and then its mass became stable. Assuming full oxidation of the sample to $CO_2(g)$ and $SiO_2(s)$, this corresponds to the sample containing only 3.26 wt. % Si. Given that the CVD-Si@Gr sample was 95% graphite and 5% Si prior to carbon coating, this means that amorphous carbon created during CVD accounts for 34.81 wt. % of the CVD-Si@Gr sample. This large amount of deposited carbon is consistent with the large

amount of carbon observed to fill the accessible cavities in the graphite particles after CVD processing. Hydrothermal treated sample lost 96.17 wt. % after being heated to 800 °C. Therefore, there was 3.55 wt. % silicon, 67.46 wt. % graphite, and 28.99 wt. % carbon in the HT-Si@Gr composite.

Figure 4.9(a) shows the voltage curve of the porous host graphite. It has a relatively high irreversible capacity of 100 mAh/g due to its high surface area, but it has a high reversible capacity (367 mAh/g) and staging plateaus characteristic of a high degree of graphitization. Figure 4.9(b) shows the voltage curve of an electrode made with a 5/95 w/w blend of Si and graphite. Additional capacity due to the added Si can clearly be
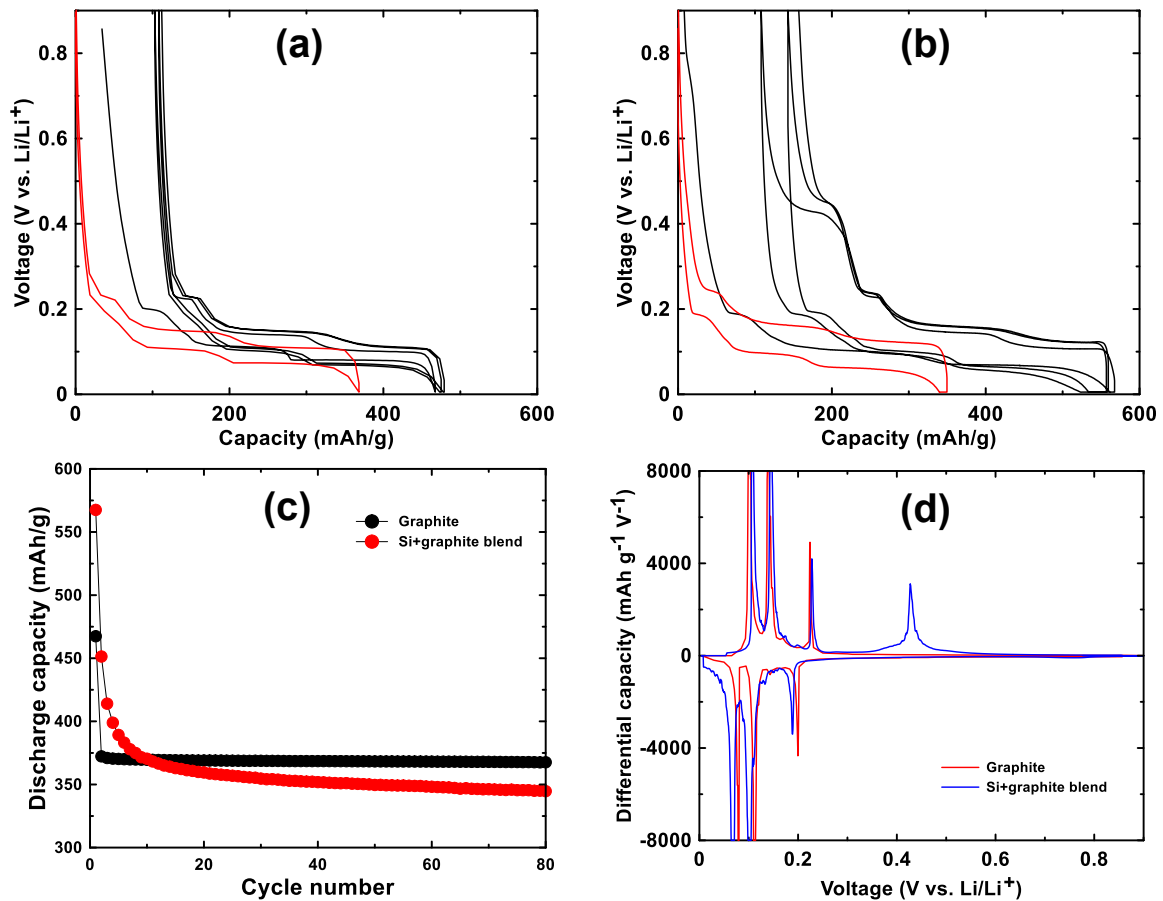
Figure 4.9   (a) and (b) Voltage profile of graphite and blending silicon and graphite (black line: 1-3 cycles; red line: 50th cycle). (c) and (d) Discharge capacity and differential capacity of graphite and blending silicon and graphite.

seen during delithiation as a plateau at about 0.45 V due to the delithiation of the $Li_{15}Si_4$

phase. Consequently, the active material capacity increased to about 450 mAh/g

compared to pure graphite. However, the addition of Si has also noticeably increased

the electrode polarization, with a larger difference between the graphite staging plateaus

during lithiation and delithiation. Furthermore the 0.45 V $Li_{15}Si_4$ delithiation plateau

quickly diminishes during cycling and by cycle 50 it is nearly gone. This suggests that

the active silicon in this electrode is rapidly fading. This is expected behavior for silicon

in an electrode with PVDF binder and cycling with no electrolyte additives.

Figure 4.9(c) shows a plot of the capacity vs. cycle number of the graphite electrode

and the electrode made with a silicon-graphite blend. The graphite electrode has no

capacity fade over the 80 cycles shown, while the silicon-graphite blend initially fades

rapidly, and then exhibits roughly linear fade after cycle 20. To estimate how much of

this capacity is attributable to silicon and to graphite, it is noted that approximately 95%

of the delithiation capacity of $Li_{15}Si_4$ occurs between 0.3 V and 0.9 V, while about 95%

of the delithiation capacity of graphite occurs between 0.005 V and 0.3 V. This can be

seen readily in the differential capacity curves of the Si blended electrode compared to

the Si-graphite blended electrode shown in Figure 4.9(d). Above 0.3 V the graphite

electrode has very little delithiation capacity, while the Si-graphite blended electrode

has substantial capacity in this region. From this property, the capacity contribution of

graphite (C_{Gr}) and silicon (C_{Si}) can be estimated from the delithiation capacity

according to:

$$C_{Overall} = C_{Gr} + C_{Si} = C_{(0.005-0.3\,V)} + C_{(0.3-0.9\,V)} \qquad (4.1)$$

$$C_{(0.005-0.3\,V)} = 95\% \times C_{Gr} + 5\% \times C_{Si} \qquad (4.2)$$

$$C_{(0.3-0.9\ V)} = 5\% \times C_{Gr} + 95\% \times C_{Si} \tag{4.3}$$

$$C_{Gr} = \frac{95\% \times C_{(0.005-0.3\ V)} - 5\% \times C_{(0.3-0.9\ V)}}{95\%^2 - 5\%^2} \tag{4.4}$$

$$C_{Si} = \frac{95\% \times C_{(0.3-0.9\ V)} - 5\% \times C_{(0.005-0.3\ V)}}{95\%^2 - 5\%^2} \tag{4.5}$$

Where $C_{(0.005-0.3V)}$ is the delithiation capacity between 0.005 V and 0.3 V and $C_{(0.3-0.9V)}$ is the delithiation capacity between 0.3 V and 0.9 V.
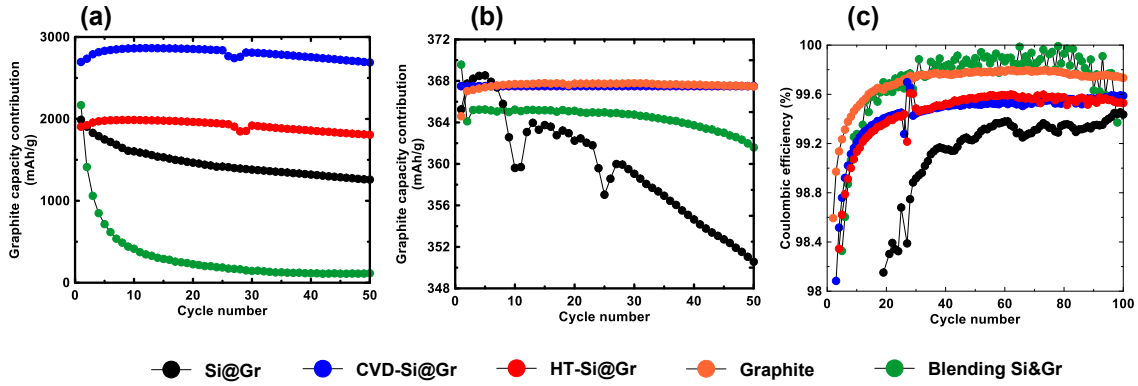
Figure 4.10   (a) Si contribution and (b) graphite contribution to the active material capacity vs. cycle number. (c) Coulombic efficiency of electrodes in this study as a function of cycle number.

Figure 4.10(a) and (b) shows a plot of the Si and graphite contribution to the delithiation capacity, respectively, of the Si-graphite blended electrode calculated according to equations (4.4) and (4.5) for the first 50 cycles. Only the first 50 cycles are shown because increasing cell polarization in the Si-graphite blended electrode causes appreciable capacity to appear above 0.3 V in addition to the Si component capacity, which interferes with the capacity calculation. As shown in Figure 4.10(a), the Si contribution to the Si-graphite blended electrode capacity fades rapidly, as expected. The graphite contribution to the Si-graphite blended electrode capacity is shown in Figure 4.10(b). Initially, the graphite contribution capacity is 370 mAh/g, which is similar to the capacity of the pure graphite electrode, but after the first cycle the capacity

drops to about 365 mAh/g. This is likely due to impedance caused by the presence of Si and its associated SEI. The graphite capacity contribution then stays constant until about cycle 40, but then starts to decrease as cell polarization increases. Figure 4.10(c) shows the coulombic efficiency (CE) of the graphite and Si-graphite blended electrodes. Initially the Si-graphite blended electrode has poor CE due to the reactivity of Si with electrolyte. After the Si capacity has faded and most of the active capacity is due to the graphite component only, the CE of the Si-graphite blended electrode becomes similar to the pure graphite electrode. From these results it can be concluded that in the Si-graphite blended electrode, the Si component of the electrode fades rapidly, while the graphite component does not exhibit significant fade. In addition, greater voltage

polarization in the blended electrode was observed comparedto that of pure graphite due to the presence of Si.

Figure 4.11(a), (b), and (c) show the voltage curves of Si@Gr, CVD-Si@Gr, and HT-Si@Gr, respectively. The discharge capacity and CE of these electrodes are shown in Figure 4.11(d) and 4.10(c). For the Si@Gr electrode, the Si and graphite capacity contributions as a function of cycle number were calculated in the same way as the Si-graphite blended electrode and the results are shown in Figure 4.10(a) and (b). As with the Si-graphite blended electrode, Si@Gr has a high voltage polarization compared to pure graphite. It also has a high initial capacity and initial rapid fade. However, the
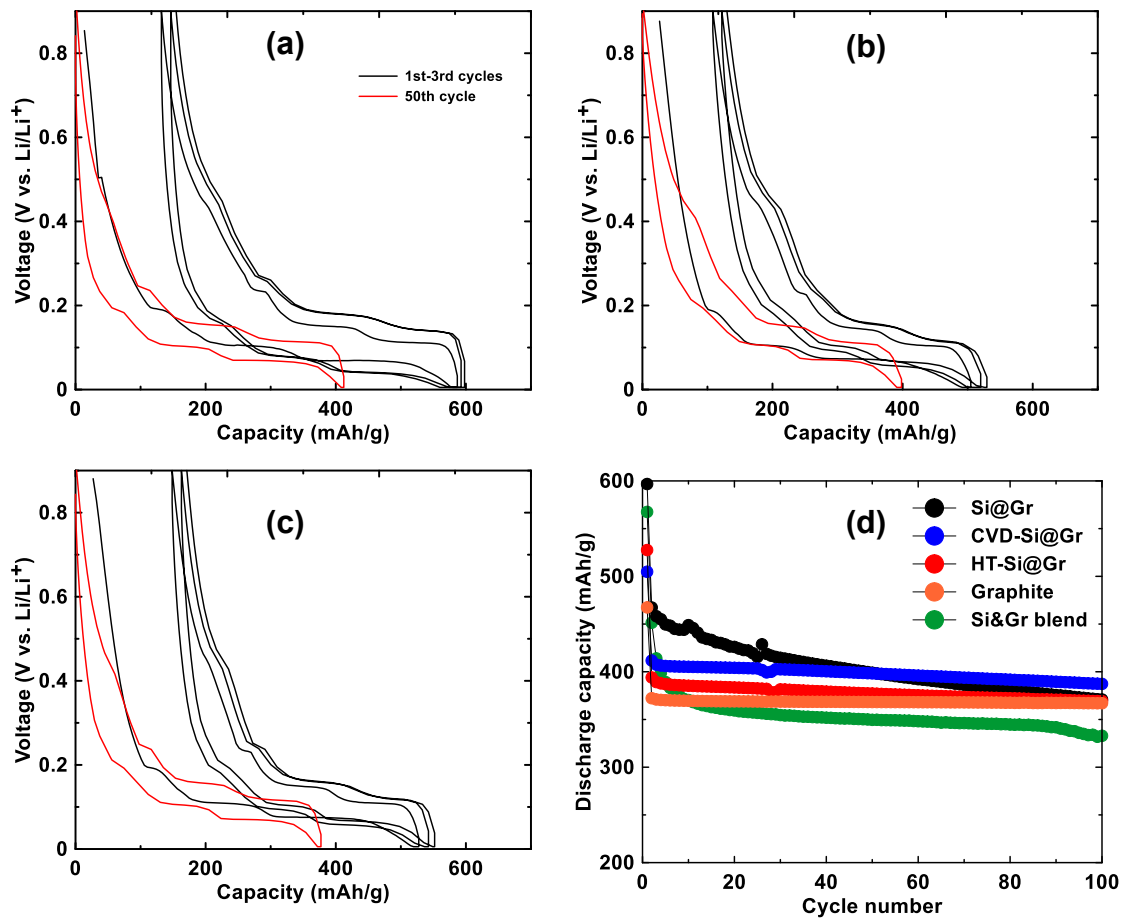
Figure 4.11   (a), (b) and (c) Voltage profile of Si@Gr, CVD-Si@Gr, and HT-Si@Gr, respectively (black line: 1-3 cycles; red line: 50th cycle). (d) Discharge capacity of silicon graphite composites.

capacity retention of Si@Gr is improved compared to the simple Si-graphite blend. This
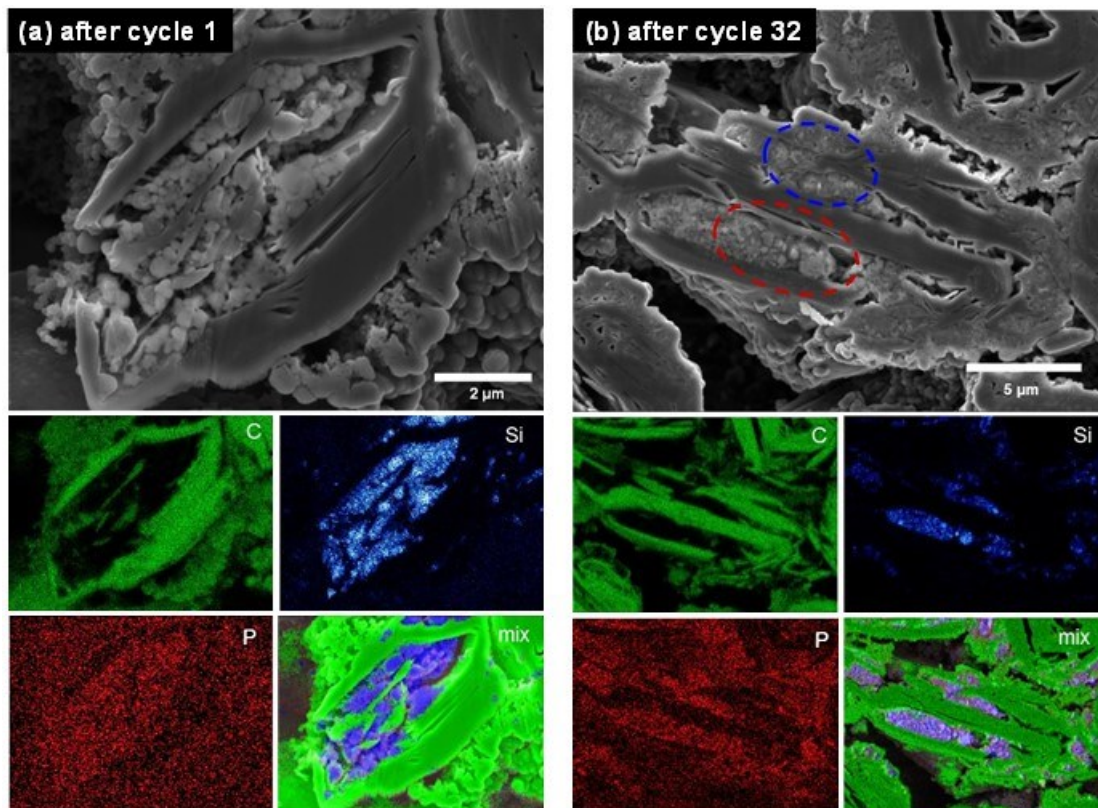
Figure 4.12 SEM images and EDS C, Si, P, and composite compositional maps of Si@Gr electrodes after (a) one cycle and (b) 32 cycles.

suggests that the Si@Gr structure can mitigate the degradation of silicon to some extent. As shown in Figure 4.11(a), Si@Gr has a greatly improved Si contribution to the capacity compared to the Si-graphite blend electrode. However, the Si capacity contribution is still only about 2000 mAh/g, which is much less than the 3578 mAh/g theoretical capacity for Si. This indicates that not all of the Si is active in this electrode. In addition, both the Si and graphite capacity contributions exhibit fade.

The reason for the above behavior can be seen in Figure 4.12(a) and (b), which shows SEM images and C, Si, P, and composite compositional maps of a cross section of a Si@Gr electrode after the first and thirty-second cycles, respectively. After the first cycle the Si particles appear nearly pristine. The phosphorous map shows almost no

contrast, indicating an absence of electrolyte decomposition products that include P (from LiPF$_6$). After the 32nd cycle, shown in Figure 4.12(b), two types of Si particles can be observed, corresponding to active and inactive Si. Circled in blue are Si particles that have nearly disintegrated. This morphology is characteristic of cycled active Si, as a consequence of fracture from repeated volume expansion/contraction cycles. Circled in red are Si particles that appear pristine. This Si has not experienced any volume expansion and is therefore inactive. The presence of this inactive Si is consistent with the less than expected Si component capacity of the Si@Gr electrode shown in Figure 4.10(a). In the P-compositional map of this electrode after 32 cycles, shown in Figure 4.12(b), there is distinctly higher P-concentration in the Si-containing regions, indicating the presence of electrolyte decomposition products, which is consistent with the low CE exhibited by this electrode during cycling. The reasons why graphite capacity in Si@Gr composite faded are the formation of electrolyte decomposition products and the volume expansion of silicon. Figure 4.13 indicates that the volume expansion of silicon can burst the graphite shell and graphite fragments were surrounded by silicon SEI product. This can cause loss of electrical contact to the Si fragments, resulting in capacity fade.
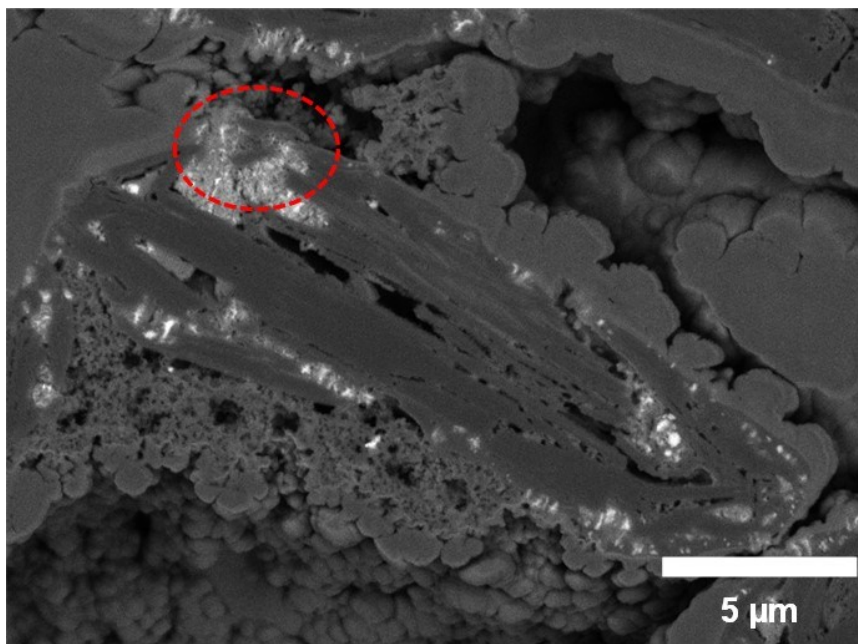
Figure 4.13   Cross-sectional BSE image of the Si@Gr electrode after 32 cycles.

Figure 4.11(b) and (d) show the voltage curve and discharge capacity vs. cycle number of the CVD-Gr@Si electrode. Initially, this electrode has a lower discharge capacity than the Si@Gr electrode. However, the CVD-Gr@Si electrode exhibits much less capacity fade and maintains about 390 mAh/g capacity over 100 cycles. To calculate the Si and graphite contributions to the capacity, equations (4.4) and (4.5) could not be used, since the result of this calculation showed that Si had substantial capacity below 0.3 V during delithiation. This would occur if some crystalline $Li_{15}Si_4$ were suppressed, which is known to happen when Si is bound to a substrate (here the substrate being the CVD deposited carbon).[74] Instead, the Si contribution to the capacity was calculated by subtracting from the total capacity, the capacity of graphite (367.5 mAh/g for the graphite used in this study) and amorphous carbon (225 mAh/g).[22] In other words, it was assumed that all electrode components except for Si cycled at their full capacity. The result of this calculation is that Si capacity contribution of CVD-

Gr@Si reaches about 3000 mAh/g and experiences 8% capacity fade over 50 cycles. This is close to the theoretical capacity of Si. Therefore, the assumption that the graphite and CVD deposited carbon are cycling at their full capacity must be a good one, since unless all components were cycling near their full capacities, the total capacity of the electrode could not be accounted for.

The high Si capacity indicates that most of the Si is active in this electrode during cycling. This is significantly improved performance compared to the Si component cycling in the mixed Si-Gr and Si@Gr electrodes. It is particularly impressive performance for Si in an electrode with no special binders and in a cell with no special electrolyte additives. The CE of CVD-Gr@Si plotted vs. cycle number is shown in Figure 6(c) and is improved (~99.6%) compared to Si@Gr (~99.4%), but it is lower than that of graphite (~99.8%). This shows that the deposited carbon reduces side reactions of Si with electrolyte compared to Si@Gr, but the extent of electrochemical side reactions is still greater than that for pure graphite.

Figure 4.14   SEM images and EDS C, Si, P, and composite compositional maps of CVD-Si@Gr electrodes after (a) one cycle and (b) 32 cycles.

The above behavior can be understood from the cross-section image and corresponding C, Si, P, and composite compositional maps of the CVD-Gr@Si electrode after 1 cycle and after 32 cycles, shown in Figure 4.14(a) and (b), respectively. After the first cycle, void spaces are present around the many of the embedded silicon particles, presumably as a result of their volume expansion and contraction. Otherwise, the Si particles appear to be almost pristine. As with the Gr@Si electrode, the P-compositional map shows almost no contrast, indicating an absence of P-containing electrolyte decomposition products. After 32 cycles, (Figure 4.14(b)) almost no distinct Si particles can be found. Instead, the carbon particles now contain regions of Si mixed with carbon. This is likely a result of repeated volume expansion and contraction of the

Si, which results in the formation of a homogenous Si/C composite. The observation that nearly all of the Si is in this form, is consistent with the near theoretical capacity of the Si component of this electrode. The phosphorous map now shows some distinct contrast with concentration of the phosphorous in the Si containing regions. This shows that although the CVD-Si@Gr electrode's reaction with the electrolyte may be slower than for the Si@Gr electrode, as indicated by CVD-Si@Gr's higher CE, electrolyte is still accessing the inside of the composite, resulting in a lower CE than graphite.

As shown in Figure 4.11(d) HT-Si@Gr shows improved capacity retention than uncoated Si@Gr and pure graphite. However, compared with CVD-Si@Gr, its capacity is lower because of the reduced silicon capacity contribution as shown in Figure 4.10
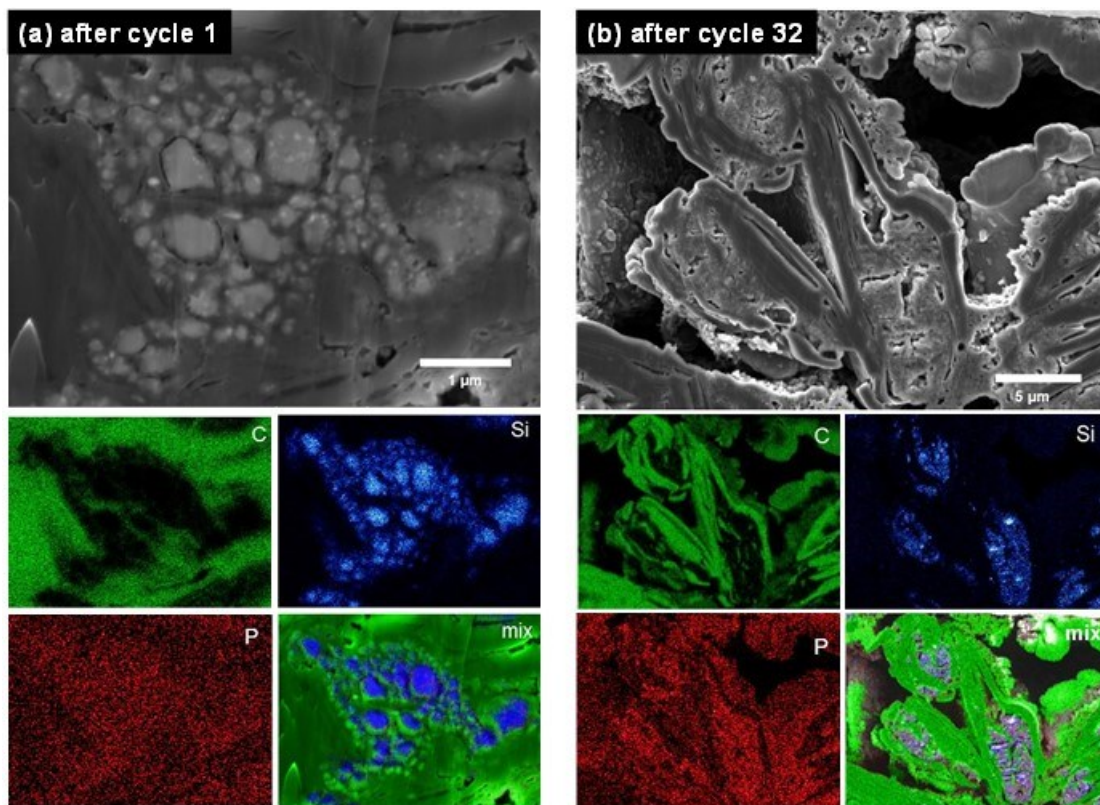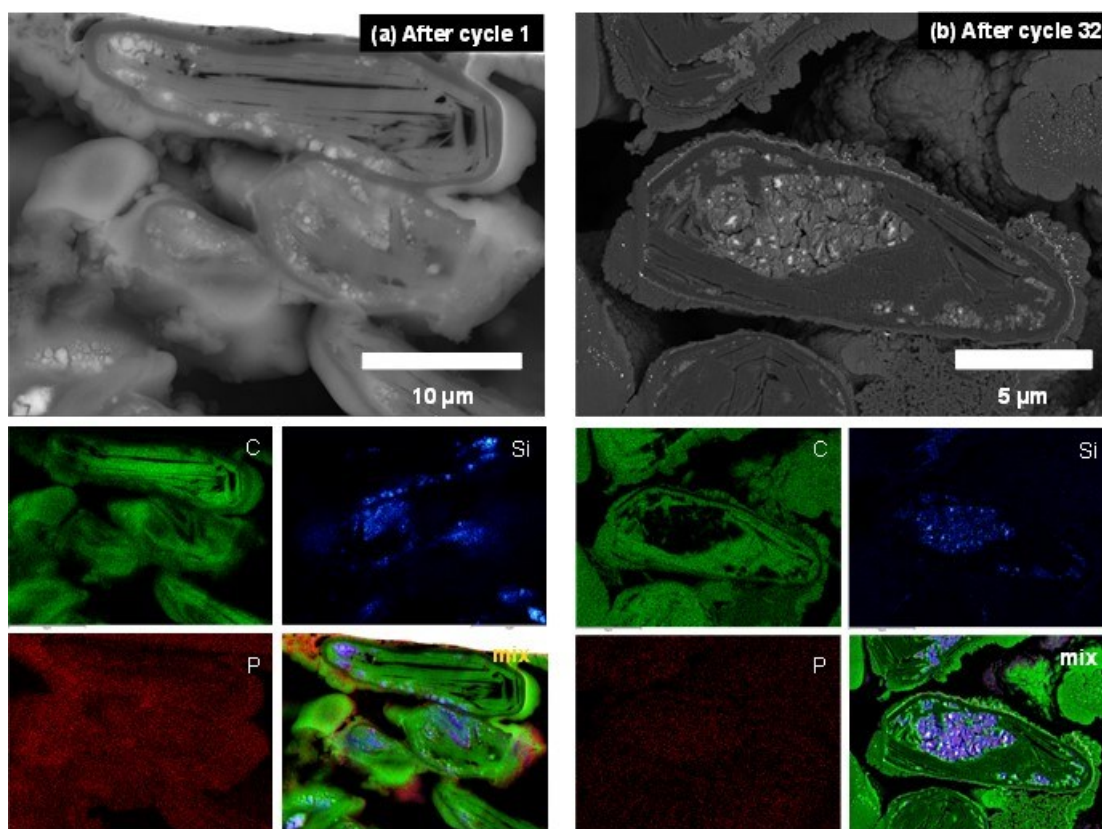

Figure 4.15   SEM images and EDS C, Si, P, and composite compositional maps of HT-Si@Gr electrodes after (a) one cycle and (b) 32 cycles.

(a). Only around 2000 mAh/g capacity of silicon is achieved when the same capacity calculation method as CVD-Si@Gr is applied. This indicates that some silicon particles may become inactive during the hydrothermal treatment. However, from the SEM images of cycled HT-Si@Gr, shown in Figure 4.15(b), all the Si particles appear to be active (indistinct highly fractured particles). In this case the low capacity of the silicon component may be due to the formation of inactive species during the hydrothermal carbon coating process (e.g. SiO_2) or its subsequent heat-treatment (e.g. SiC). From the XRD pattern in Figure 4.6, HT-Si@Gr has greatly increased intensity at low angle range corresponding to the presence of 28.99 wt. % amorphous carbon, which reduces the overall electrode's capacity. However, the carbon layer formed during the hydrothermal process has the same protective effect as CVD carbon. As shown in Figure 4.15, after the first cycle, most phosphorus deposited on carbon layers while only a little P signals are detected inside the graphite particles. Even after 32 cycles, the contrast between inside and outside graphite is not strong which means that most SEI layers were formed outside of the graphite particles. Therefore, electrolyte decomposition happened, but at a slow rate compared to uncoated Si@Gr.

Overall, of the Si-containing electrodes the CVD-Gr@Si electrode had the highest capacity and best capacity retention. Achieving nearly theoretical capacity for Si over 100 cycles in an electrode with a PVDF binder and in a cell with no special electrolyte additives is remarkable for Si. However, the ~400 mAh/g capacity of CVD-Gr@Si represents only a modest increase compared to graphite. This is due to the large amount of vapor deposited carbon (34 wt%). If the amount of deposited carbon could be reduced to something more reasonable like ~5 wt.%, then the capacity could be

increased to ~480 mAh/g. This is clearly an avenue for future studies.

4.4   Conclusion

Mechanofusion was used to embed n-Si particles into void spaces within natural graphite. It was found that during mechanofusion the n-Si particles behaved like a fluid and penetrated only into void spaces that were accessible from cracks or fissures in the graphite particle surface. The resulting Si@Gr composites were formulated in electrodes with PVDF binder and cycled versus lithium in cells with no special electrolyte additives. The Si@Gr composite had improved cycling compared to a Si-graphite mixture, but still suffered from severe capacity fade. This was due to electrolyte penetration into the Si-containing voids within the graphite, resulting in severe capacity fade of the Si phase and SEI growth that caused impedance and capacity fade also of the graphite phase. To improve cycling performance, carbon was chemical vapor deposited onto Si@Gr particles. The resulting CVD-Si@Gr sample achieved good cycling performance with conventional PVDF binder and FEC-free electrolyte. After 50 cycles, most silicon was still active with ~2750 mAh/g capacity from the Si phase and a 396.4 mAh/g capacity overall.

This study sheds light on a promising approach to a scalable method to synthesize silicon/graphite composites as drop-in substitutes for graphite that require no special binders or electrolyte additives to cycle in lithium-ion batteries. Future work will focus on increasing the capacity further, especially by reducing the amount of deposited carbon.

CHAPTER 5   CONCLUSION

5.1   Conclusion

With the increasing consciousness of environmental protection, the regulations on carbon emissions worldwide become harsher and harsher. The exploration of new energy sources and new means of energy storage is of great importance. Lithium-ion batteries, as energy storage and conversion devices, have attracted much attention. Traditional commercial lithium-ion batteries utilize graphite as an anode material. However, new anode materials offering higher capacities and that are less prone to dendrites could improve Li-ion battery energy density and safety further. The development of electric vehicles and energy storage stations put higher demand on lithium-ion batteries. Investigating high-energy density anode materials becomes a necessity. Silicon has a great theoretical capacity (3570 mAh/g, 2194 Ah/L). The average potential of lithiation is around 0.4 V, which will not cause lithium plating. However, great capacity comes with great volume expansion (280%). Huge volume change results in particle pulverization, disconnection from conductive agents, and coating delamination. The unstable SEI layer is another critical issue. In addition, silicon is a semiconductor with a low conductivity.

To solve these problems, this thesis used two strategies. The first is to develop an efficient binder. The other is to incorporate Si into graphite. Binders play an important

role in silicon-based anodes. A good binder can bind all electrode components tightly. Specifically, for Si-based anodes, a binder which can withstand the high-volume change is desired. Binders adsorbed on the active particles' surface can behave as an artificial SEI, which can protect the silicon from side reactions. Moreover, binders are also important as slurry modifiers to get a good distribution of all components. Although employing pure silicon in anodes is still a challenge, a combination of graphite and silicon is a practical and promising way to ameliorate graphite anodes. In a silicon graphite composite anode, silicon can provide extra lithium storage while graphite works independently. Since the content of silicon is controlled, the concern of volume expansion is trivialized. Simple mixing of silicon and graphite cannot work well because of silicon's problems as mentioned above. The structure of silicon graphite composite needs to be specifically designed to overcome volume expansion and to avoid the electrolyte coming into contact with Si. Generally, silicon must be dispersed within graphite and protected by graphite or another coating to obtain a long cycle life.

In Chapter 3 a study of the binder performance for silicon-based anodes is described. Pure silicon anode is not practical in the current stage. Silicon monoxide is one of the best substitutes for silicon. It has a high capacity (1710 mAh/g, 1400 Ah/g), but its volume expansion is reduced to 200%. Nevertheless, this volume change can still be detrimental to electrodes. Therefore, a binder that has strong binding forces and can coat the active particles to form an artificial SEI is necessary. PAA has been proven as an advanced binder for silicon-based anodes. PAA has lots of superior properties such as forming chemical bonds with silicon particles and good solubility in water. Molecular weight is a very important factor for polymer binders. This thesis

investigated the effect of NaPAA molecular weight on the cycling performance of SiO anodes. Aqueous low MW binders resulted in low slurry viscosity, particle settling, and binder loss during coating. This study showed the relationship between cycling performance and MW for aqueous slurries. When PG was used as the slurry solvent, the problem of poor rheology for low MW binders was eliminated. As a result, binder performance is deconvoluted from slurry rheology. Electrodes with low MW binders can then cycle as well as those with high MW binders. The viscous solvent can maintain a homogeneous dispersion of electrode components. It was demonstrated that the binder MW has no relation to electrode performance, as long as good rheological properties are maintained.

Chapter 4 introduced a novel way to synthesize silicon graphite composite via mechanofusion. A spherical natural graphite was used as a host structure because of its abundance of inner cavities. Nano silicon as guest particles were embedded in these cavities. The as-prepared Si@Gr composite particles had improved cycle life and capacity EC/DEC electrolyte with PVDF binders compared to a simple Si-graphite blended electrode. To improve performance further carbon coating by hydrothermal and chemical vapour deposition was conducted on the Si@Gr composite. This resulted in the silicon particles becoming fully encapsulated in a carbon matrix. In particular, the carbon-coated CVD-Si@Gr can achieve a capacity of 390 mAh/g over 100 cycles in a conventional electrolyte without any additives. The mechanism of degradation was investigated by cross-sectional EDS imaging. For uncoated Si@Gr composites, silicon was directly exposed to electrolyte and formed a thick SEI during cycling. For CVD-Si@Gr, silicon expanded during the lithiation process breaking the carbon coating and

creating some pores after shrinking. Electrolytes can penetrate along the boundaries of silicon and form SEI, but this process is greatly impeded compared to the uncoated Si@Gr composite, resulting in improved capacity retention.

5.2   Future work

The success of binders like PAA and CMC for Si-based anodes is because of their functional carboxylic groups. These carboxylic groups can not only bind with silanol groups but also show a good connection to copper foil. In the future, more types of binders will be evaluated. The discovery presented in this thesis is that slurry solvents can establish good slurry rheology independently of the binder molecular weight offers exciting avenues for studying new binders. In particular, single molecule binders should be studied, to see if they can perform just as well as their polymeric counterparts when a viscous slurry solvent (such as PG) is utilized. If this proves to be true, then molecules with many functional groups like -OH, -COOH, and $-NH_2$ could be studied as binders. Molecules with more than one type of functional group or blends of functional groups could be studied to take advantage of interactions between different functional groups. For instance, such molecules might even physically and chemically cross-link at elevated temperatures. As a result, the special 3-dimensional structure can adapt to huge volume changes and keep electrode integrity. Some of my experiments suggested PG might interact with PAA by esterification or hydrogen bonds over a long-time period at high temperature. The possibility of interactions between PG and PAA needs to be investigated carefully.

Currently, there is a lot of research focusing on silicon graphite composites. The core-shell structure is the most popular structure design. The structure created by mechanofusion is very interesting. With the insertion of silicon into the holes, the utility rate of space and capacity is improved. However, there is no defined core and no defined shell. Silicon embedded in the cavities is risky for exposure to electrolytes. Therefore, extra steps need to be taken to encapsulate silicon particles. Directly coating carbon on nano silicon does not work because the strength of amorphous carbon cannot resist the strain from silicon volume expansion. So after silicon is embedded into graphite, the pores need to be closed as well. During my previous experiments, it was found that by adjusting the mechanofusion gap and speed, different configurations were obtained. In this way, a structure where silicon stays in the shelter of graphite can be synthesized by adjusting the speed and adding different components in multiple steps. On the other hand, various coating methods need to be developed to make sure there is no access to silicon, while still providing Si with room for volume expansion. CVD, hydrothermal treatment, and pitch pyrolysis have already been tried. However, for different samples, the conditions may be different. In addition, the amount of carbon coating should be just enough to restrict electrolyte access to the Si, but not significantly affect capacity: for instance, in amounts similar to carbon coatings currently used for commercial graphites (~0.5 wt%). Thus, a systematic investigation of the coating method in conjunction with mechanofusion conditions is necessary to find the optimal conditions for making Si@Gr particles in which the Si has volume in which to expand, but is protected from electrolyte by an exterior carbon coating.

BIBLIOGRAPHY

(1)   Mauger, A.; Julien, C. M.; Goodenough, J. B.; Zaghib, K. Tribute to Michel Armand: From Rocking Chair – Li-Ion to Solid-State Lithium Batteries. *J Electrochem Soc* **2020**, *167* (7), 070507. https://doi.org/10.1149/2.0072007JES.

(2)   Wu, Q.; Zhang, B.; Lu, Y. Progress and Perspective of High-Voltage Lithium Cobalt Oxide in Lithium-Ion Batteries. *J Energy Chem*, **2022**, 74, 283–308. https://doi.org/10.1016/j.jechem.2022.07.007.

(3)   Radin, M. D.; Hy, S.; Sina, M.; Fang, C.; Liu, H.; Vinckeviciute, J.; Zhang, M.; Whittingham, M. S.; Meng, Y. S.; Van der Ven, A. Narrowing the Gap between Theoretical and Practical Capacities in Li-Ion Layered Oxide Cathode Materials. *Adv Energy Mater*. Wiley-VCH Verlag, **2017**, 7 (4), 160288 https://doi.org/10.1002/aenm.201602888.

(4)   Du, F.; Ding, L.; Shi, W.; Wang, Y.; Fan, Z.; Li, Y.; Zheng, J. Promoting Effect of Magnesium Introduced in Li/Ni Sites of LiNiO2 for Lithium-Ion Batteries. *Ceram Int* **2023**, *49* (6), 9924–9931. https://doi.org/10.1016/j.ceramint.2022.11.168.

(5)   Tian, Y.; Qiu, Y.; Liu, Z.; Wei, X.; Cao, H. LiMnO2@rGO Nanocomposites for High-Performance Lithium-Ion Battery Cathodes. *Nanotechnology* **2021**, *32* (1), 015402. https://doi.org/10.1088/1361-6528/abb48c.

(6)   Malik, M.; Chan, K. H.; Azimi, G. Review on the Synthesis of LiNixMnyCo1-x-YO2 (NMC) Cathodes for Lithium-Ion Batteries. *Mater Today Energy*, **2022**, 28, 101066 https://doi.org/10.1016/j.mtener.2022.101066.

(7)   Yi, T. F.; Zhu, Y. R.; Zhu, X. D.; Shu, J.; Yue, C. B.; Zhou, A. N. A Review of Recent Developments in the Surface Modification of LiMn2O4 as Cathode Material of Power Lithium-Ion Battery. *Ionics*, **2009**, 15, 779–784. https://doi.org/10.1007/s11581-009-0373-x.

(8)   Suttison, S.; Pengpat, K.; Intatha, U.; Fan, J.; Zhang, W.; Eitssayeam, S. Preparation of LFP-Based Cathode Materials for Lithium-Ion Battery Applications. *Mater Today Proc* **2022**, *65*, 2347–2350. https://doi.org/10.1016/j.matpr.2022.05.302.

(9)   Zheng, G.; Lee, S. W.; Liang, Z.; Lee, H. W.; Yan, K.; Yao, H.; Wang, H.; Li, W.; Chu, S.; Cui, Y. Interconnected Hollow Carbon Nanospheres for Stable Lithium Metal Anodes. *Nat Nanotechnol* **2014**, *9* (8), 618–623.

https://doi.org/10.1038/nnano.2014.152.

(10) Yang, C. P.; Yin, Y. X.; Zhang, S. F.; Li, N. W.; Guo, Y. G. Accommodating Lithium into 3D Current Collectors with a Submicron Skeleton towards Long-Life Lithium Metal Anodes. *Nat Commun* **2015**, 6, 8058. https://doi.org/10.1038/ncomms9058.

(11) Agubra, V. A.; Fergus, J. W. The Formation and Stability of the Solid Electrolyte Interface on the Graphite Anode. *J Power Sources*. **2014**, 268, 153–162. https://doi.org/10.1016/j.jpowsour.2014.06.024.

(12) Ding, Y. S.; Li, W. N.; Iaconetti, S.; Shen, X. F.; DiCarlo, J.; Galasso, F. S.; Suib, S. L. Characteristics of Graphite Anode Modified by CVD Carbon Coating. *Surf Coat Technol* **2006**, *200* (9), 3041–3048. https://doi.org/10.1016/j.surfcoat.2005.05.040.

(13) Lee, J. H.; Lee, H. Y.; Oh, S. M.; Lee, S. J.; Lee, K. Y.; Lee, S. M. Effect of Carbon Coating on Electrochemical Performance of Hard Carbons as Anode Materials for Lithium-Ion Batteries. *J Power Sources* **2007**, *166* (1), 250–254. https://doi.org/10.1016/j.jpowsour.2006.12.078.

(14) Zhang, W. J. Lithium Insertion/Extraction Mechanism in Alloy Anodes for Lithium-Ion Batteries. *J Power Sources*, **2011**, 196 (3), 877–885. https://doi.org/10.1016/j.jpowsour.2010.08.114.

(15) Ryu, I.; Choi, J. W.; Cui, Y.; Nix, W. D. Size-Dependent Fracture of Si Nanowire Battery Anodes. *J Mech Phys Solids* **2011**, *59* (9), 1717–1730. https://doi.org/10.1016/j.jmps.2011.06.003.

(16) Li, P.; Kim, H.; Myung, S. T.; Sun, Y. K. Diverting Exploration of Silicon Anode into Practical Way: A Review Focused on Silicon-Graphite Composite for Lithium Ion Batteries. *Energy Storage Materials*, **2021**, 35, 550–576. https://doi.org/10.1016/j.ensm.2020.11.028.

(17) Lu, Z.; Liu, N.; Lee, H. W.; Zhao, J.; Li, W.; Li, Y.; Cui, Y. Nonfilling Carbon Coating of Porous Silicon Micrometer-Sized Particles for High-Performance Lithium Battery Anodes. *ACS Nano* **2015**, *9* (3), 2540–2547. https://doi.org/10.1021/nn505410q.

(18) Magasinski, A.; Zdyrko, B.; Kovalenko, I.; Hertzberg, B.; Burtovyy, R.; Huebner, C. F.; Fuller, T. F.; Luzinov, I.; Yushin, G. Toward Efficient Binders for Li-Ion Battery Si-Based Anodes: Polyacrylic Acid. *ACS Appl Mater Interfaces* **2010**, *2* (11), 3004–3010. https://doi.org/10.1021/am100871y.

(19) Obrovac, M. N.; Christensen, L. Structural Changes in Silicon Anodes during Lithium Insertion/Extraction. *Electrochem Solid-State Lett* **2004**, *7* (5), A93-96. https://doi.org/10.1149/1.1652421.

(20) Jia, H.; Zheng, J.; Song, J.; Luo, L.; Yi, R.; Estevez, L.; Zhao, W.; Patel, R.; Li, X.; Zhang, J. G. A Novel Approach to Synthesize Micrometer-Sized Porous Silicon as a High Performance Anode for Lithium-Ion Batteries. *Nano Energy* **2018**, *50*, 589–597. https://doi.org/10.1016/J.NANOEN.2018.05.048.

(21) Ng, S. H.; Wang, J.; Wexler, D.; Chew, S. Y.; Liu, H. K. Amorphous Carbon-Coated Silicon Nanocomposites: A Low-Temperature Synthesis via Spray Pyrolysis and Their Application as High-Capacity Anodes for Lithium-Ion Batteries. *J Phys Chem C* **2007**, *111* (29), 11131–11138. https://doi.org/10.1021/jp072778d.

(22) Wang, J.; Obrovac, M. N. Lab-Scale Chemical Vapor Deposition onto Powders. *AIP Adv* **2022**, *12* (7), 075209. https://doi.org/10.1063/5.0095882.

(23) Wen, Z. S.; Yang, J.; Wang, B. F.; Wang, K.; Liu, Y. High Capacity Silicon/Carbon Composite Anode Materials for Lithium Ion Batteries. *Electrochem commun* **2003**, *5* (2), 165–168. https://doi.org/10.1016/S1388-2481(03)00009-2.

(24) Yoon, Y. S.; Jee, S. H.; Lee, S. H.; Nam, S. C. Nano Si-Coated Graphite Composite Anode Synthesized by Semi-Mass Production Ball Milling for Lithium Secondary Batteries. *Surf Coat Technol* **2011**, *206* (2–3), 553–558. https://doi.org/10.1016/j.surfcoat.2011.07.076.

(25) Jung, D. S.; Hwang, T. H.; Park, S. Bin; Choi, J. W. Spray Drying Method for Large-Scale and High-Performance Silicon Negative Electrodes in Li-Ion Batteries. *Nano Lett* **2013**, *13* (5), 2092–2097. https://doi.org/10.1021/nl400437f.

(26) Philipp, H. R. Optical Properties of Non-Crystalline Si, SiO, SiOx and SiO2. *J. Phys. Chem.* **1971**, *32* (8), 1935–1945. https://doi.org/10.1016/S0022-3697(71)80159-2

(27) Nagamori, M.; Boivin, J.-A.; Claveau, A. Gibbs Free Energies of Formation of Amorphous Si2O3, SiO and Si2O. *J Non Cryst Solids* **1995**, *189* (3), 270–276. https://doi.org/10.1016/0022-3093(95)00239-1

(28) Brady, G. W. A Study of Amorphous SiO. *J Phys Chem* **1959**, *63*, 1119–1120. https://pubs.acs.org/doi/pdf/10.1021/j150577a020

(29) Friede, B.; Jansen, M. Letter to the Editor Some Comments on So-Called "Silicon Monoxide." *J Non Cryst Solids* **1996**, *204* (2), 202–203. https://doi.org/10.1016/S0022-3093(96)00555-8

(30) Cao, Y.; Dunlap, R. A.; Obrovac M. N. Electrochemistry and Thermal Behavior of SiOx Made by Reactive Gas Milling. *J Electrochem Soc* **2020**, *167,* 110501. https://doi.org/10.1149/1945-7111/ab9e83

(31) Otero, M.; Heim, C.; Leiva, E. P. M.; Wagner, N.; Friedrich, A. Design-Considerations Regarding Silicon/Graphite and Tin/Graphite Composite Electrodes for Lithium-Ion Batteries. *Sci Rep* **2018**, *8* (1), 15851. https://doi.org/10.1038/s41598-018-33405-y.

(32) Wetjen, M.; Pritzl, D.; Jung, R.; Solchenbach, S.; Ghadimi, R.; Gasteiger, H. A. Differentiating the Degradation Phenomena in Silicon-Graphite Electrodes for Lithium-Ion Batteries. *J Electrochem Soc* **2017**, *164* (12), A2840–A2852. https://doi.org/10.1149/2.1921712jes.

(33) Moyassari, E.; Roth, T.; Kücher, S.; Chang, C.-C.; Hou, S.-C.; Spingler, F. B.; Jossen, A. The Role of Silicon in Silicon-Graphite Composite Electrodes Regarding Specific Capacity, Cycle Stability, and Expansion. *J Electrochem Soc* **2022**, *169* (1), 010504. https://doi.org/10.1149/1945-7111/ac4545.

(34) Etacheri, V.; Haik, O.; Goffer, Y.; Roberts, G. A.; Stefan, I. C.; Fasching, R.; Aurbach, D. Effect of Fluoroethylene Carbonate (FEC) on the Performance and Surface Chemistry of Si-Nanowire Li-Ion Battery Anodes. *Langmuir* **2012**, *28* (1), 965–976. https://doi.org/10.1021/la203712s.

(35) Liu, G.; Zheng, H.; Song, X.; Battaglia, V. S. Particles and Polymer Binder Interaction: A Controlling Factor in Lithium-Ion Electrode Performance. *J Electrochem Soc* **2012**, *159* (3), A214–A221. https://doi.org/10.1149/2.024203jes.

(36) Mazouzi, D.; Karkar, Z.; Hernandez, C. R.; Manero, P. J.; Guyomard, D.; Roué, L.; Lestriez, B. Critical Roles of Binders and Formulation at Multiscales of Silicon-Based Composite Electrodes. *J Power Sources*, **2015**, 280, 533–549. https://doi.org/10.1016/j.jpowsour.2015.01.140.

(37) Zheng, H.; Yang, R.; Liu, G.; Song, X.; Battaglia, V. S. Cooperation between Active Material, Polymeric Binder and Conductive Carbon Additive in Lithium Ion Battery Cathode. *J Phys Chem C* **2012**, *116* (7), 4875–4882. https://doi.org/10.1021/jp208428w.

(38) Wei, C.; Obrovac, M. N. Small Molecule Slurry Additives for Si Alloy Coatings with CMC/SBR Binder. *J Electrochem Soc* **2019**, *166* (14), A3217–A3221. https://doi.org/10.1149/2.0311914jes.

(39) Karkar, Z.; Guyomard, D.; Roué, L.; Lestriez, B. A Comparative Study of Polyacrylic Acid (PAA) and Carboxymethyl Cellulose (CMC) Binders for Si-Based Electrodes. *Electrochim Acta* **2017**, *258*, 453–466. https://doi.org/10.1016/j.electacta.2017.11.082.

(40) Hernandez, C. R.; Etiemble, A.; Douillard, T.; Mazouzi, D.; Karkar, Z.; Maire, E.; Guyomard, D.; Lestriez, B.; Roué, L. A Facile and Very Effective Method to Enhance the Mechanical Strength and the Cyclability of Si-Based Electrodes for Li-Ion Batteries. *Adv Energy Mater* **2018**, *8* (6). https://doi.org/10.1002/aenm.201701787.

(41) Hu, B.; Jiang, S.; Shkrob, I. A.; Zhang, J.; Trask, S. E.; Polzin, B. J.; Jansen, A.; Chen, W.; Liao, C.; Zhang, Z.; Zhang, L. Understanding of Pre-Lithiation of Poly(Acrylic Acid) Binder: Striking the Balances between the Cycling Performance and Slurry Stability for Silicon-Graphite Composite Electrodes in Li-Ion Batteries. *J Power Sources* **2019**, *416*, 125–131. https://doi.org/10.1016/j.jpowsour.2019.01.068.

(42) Nguyen, C. C.; Yoon, T.; Seo, D. M.; Guduru, P.; Lucht, B. L. Systematic Investigation of Binders for Silicon Anodes: Interactions of Binder with Silicon Particles and Electrolytes and Effects of Binders on Solid Electrolyte Interphase Formation. *ACS Appl Mater Interfaces* **2016**, *8* (19), 12211–12220. https://doi.org/10.1021/acsami.6b03357.

(43) Ui, K.; Fujii, D.; Niwata, Y.; Karouji, T.; Shibata, Y.; Kadoma, Y.; Shimada, K.; Kumagai, N. Analysis of Solid Electrolyte Interface Formation Reaction and Surface Deposit of Natural Graphite Negative Electrode Employing Polyacrylic Acid as a Binder. *J Power Sources* **2014**, *247*, 981–990. https://doi.org/10.1016/j.jpowsour.2013.08.083.

(44) Browning, K. L.; Sacci, R. L.; Doucet, M.; Browning, J. F.; Kim, J. R.; Veith, G. M. The Study of the Binder Poly(Acrylic Acid) and Its Role in Concomitant Solid-Electrolyte Interphase Formation on Si Anodes. *ACS Appl Mater Interfaces* **2020**, *12* (8), 10018–10030. https://doi.org/10.1021/acsami.9b22382.

(45) Koo, B.; Kim, H.; Cho, Y.; Lee, K. T.; Choi, N. S.; Cho, J. A Highly Cross-Linked Polymeric Binder for High-Performance Silicon Negative Electrodes in Lithium Ion Batteries. *Angewandte Chemie - International Edition* **2012**, *51* (35), 8762–8767. https://doi.org/10.1002/anie.201201568.

(46) Liu, Z.; Han, S.; Xu, C.; Luo, Y.; Peng, N.; Qin, C.; Zhou, M.; Wang, W.; Chen, L.; Okada, S. In Situ Crosslinked PVA-PEI Polymer Binder for Long-Cycle Silicon Anodes in Li-Ion Batteries. *RSC Adv* **2016**, *6* (72), 68371–68378. https://doi.org/10.1039/c6ra12232a.

(47) Wu, M.; Song, X.; Liu, X.; Battaglia, V.; Yang, W.; Liu, G. Manipulating the Polarity of Conductive Polymer Binders for Si-Based Anodes in Lithium-Ion Batteries. *J Mater Chem A Mater* **2015**, *3* (7), 3651–3658. https://doi.org/10.1039/c4ta06594h.

(48) Li, S. Y.; Church, B. C. Effect of Aqueous-Based Cathode Slurry PH and Immersion Time on Corrosion of Aluminum Current Collector in Lithium-Ion Batteries. *Materials and Corrosion* **2016**, *67* (9), 978–987. https://doi.org/10.1002/maco.201608843.

(49) Vogl, U. S.; Das, P. K.; Weber, A. Z.; Winter, M.; Kostecki, R.; Lux, S. F. Mechanism of Interactions between CMC Binder and Si Single Crystal Facets. *Langmuir* **2014**, *30* (34), 10299–10307. https://doi.org/10.1021/la501791q.

(50) Han, Z. J.; Yamagiwa, K.; Yabuuchi, N.; Son, J. Y.; Cui, Y. T.; Oji, H.; Kogure, A.; Harada, T.; Ishikawa, S.; Aoki, Y.; Komaba, S. Electrochemical Lithiation Performance and Characterization of Silicon-Graphite Composites with Lithium, Sodium, Potassium, and Ammonium Polyacrylate Binders. *Phys Chem Chem Phys* **2015**, *17* (5), 3783–3795. https://doi.org/10.1039/c4cp04939j.

(51) Komaba, S.; Itabashi, T.; Watanabe, M.; Groult, H.; Kumagai, N. Electrochemistry of Graphite in Li and Na Salt Codissolving Electrolyte for Rechargeable Batteries. *J Electrochem Soc* **2007**, *154* (4), A322. https://doi.org/10.1149/1.2472552.

(52) Lee, B. R.; Oh, E. S. Effect of Molecular Weight and Degree of Substitution of a Sodium-Carboxymethyl Cellulose Binder on Li4Ti5O 12 Anodic Performance. *J Phys Chem C* **2013**, *117* (9), 4404–4409. https://doi.org/10.1021/jp311678p.

(53) Kasinathan, R.; Mario, M.; Axmann, P.; Wohlfachrt-Mehrens, M. Influence of the Molecular Weight of Poly-Acrylic Acid Binder on Performance of Si-Alloy Graphite Composite Anodes. *Energy Technology* **2018**, No. 6, 2256–2263. https://doi.org/10.1002/ente.201800302

(54) Hu, B.; Shkrob, I. A.; Zhang, S.; Zhang, L.; Zhang, J.; Li, Y.; Liao, C.; Zhang, Z.; Lu, W.; Zhang, L. The Existence of Optimal Molecular Weight for Poly(Acrylic Acid) Binders in Silicon/Graphite Composite Anode for Lithium-Ion Batteries. *J Power Sources* **2018**, *378*, 671–676.

https://doi.org/10.1016/j.jpowsour.2017.12.068.

(55) Miranda, A.; Li, X.; Haregewoin, A. M.; Sarang, K.; Lutkenhaus, J.; Kostecki, R.; Verduzco, R. A Comprehensive Study of Hydrolyzed Polyacrylamide as a Binder for Silicon Anodes. *ACS Appl Mater Interfaces* **2019**, *11* (47), 44090–44100. https://doi.org/10.1021/acsami.9b13257.

(56) Bunaciu, A. A.; Udriștioiu, E. gabriela; Aboul-Enein, H. Y. X-Ray Diffraction: Instrumentation and Applications. *Crit Rev Anal Chem* **2015**, *45* (4), 289–299. https://doi.org/10.1080/10408347.2014.949616.

(57) Pope, C. G. X-Ray Diffraction and the Bragg Equation. *J Chem Educ* **1997**, *74* (1), 20. https://doi.org/10.1021/ed074p129.

(58) Mohammed, A.; Abdullah, A. Scanning Electron Microscopy: A Review. In *International Conference on Hydraulics and Pneumatics*; **2018**, 77–85. https://fluidas.ro/hervex/proceedings2018/77-85.pdf

(59) Vernon-Parry, K. D. Scanning Electron Microscopy: An Introduction. *III-Vs Review* **2000**, *13* (4), 40–44. https://doi.org/10.1016/S0961-1290(00)80006-X

(60) Chang, C. S. Measuring Density Porosity of Grain Kernels Using a Gas Pycnometer. *Cereal Chem* **1988**, *65* (1), 13–15. https://www.ars.usda.gov/ARSUserFiles/30200525/177%20Measuring%20Density%20Porosity%20of%20Grain%20Kernels.pdf

(61) West, J. B. The Original Presentation of Boyle's Law. *J Appl Physiol* **1999**, *84* (4), 1543–1545. https://doi.org/10.1152/jappl.1999.87.4.1543

(62) Fagerlund, G. Determination of Specific Surface by the BET Method. *Mat. Constr* **1973**, *6*, 239–245. https://doi.org/10.1007/BF02479039

(63) Ouyang, L.; Wu, Z.; Wang, J. Fabricating Technology and Influence Factors of Slurries in Li-Ion Batteries. *Journal of Materials Engineering* **2021**, *49* (7), 21–34. https://doi.org/10.11868/j.issn.1001-4381.2020.000088

(64) Obrovac, M. N. Si-Alloy Negative Electrodes for Li-Ion Batteries. *Curr Opin Electrochem*, **2018**, 9, 8–17. https://doi.org/10.1016/j.coelec.2018.02.002.

(65) Obrovac, M. N.; Chevrier, V. L. Alloy Negative Electrodes for Li-Ion Batteries. *Chem Rev*. ACS, **2014**, 114, 11444–11502. https://doi.org/10.1021/cr500207g.

(66) Kovalenko, I.; Zdyrko, B.; Magasinski, A.; Hertzberg, B.; Milicev, Z.; Burtovyy, R.; Luzinov, I.; Yushin, G. A Major Constituent of Brown Algae for Use in High-Capacity Li-Ion Barreries. *Science (1979)* **2011**, *334* (6052), 75–79. https://doi.org/10.1126/science.1208891.

(67) Wilkes, B. N.; Brown, Z. L.; Krause, L. J.; Triemert, M.; Obrovac, M. N. The Electrochemical Behavior of Polyimide Binders in Li and Na Cells. *J Electrochem Soc* **2016**, *163* (3), A364–A372. https://doi.org/10.1149/2.0061603jes.

(68) Oh, J.; Jin, D.; Kim, K.; Song, D.; Lee, Y. M.; Ryou, M. H. Improving the Cycling Performance of Lithium-Ion Battery Si/Graphite Anodes Using a Soluble Polyimide Binder. *ACS Omega* **2017**, *2* (11), 8438–8444. https://doi.org/10.1021/acsomega.7b01365.

(69) Hatchard, T. D.; Bissonnette, P.; Obrovac, M. N. Phenolic Resin as an Inexpensive High Performance Binder for Li-Ion Battery Alloy Negative Electrodes. *J Electrochem Soc* **2016**, *163* (9), A2035–A2039. https://doi.org/10.1149/2.1121609jes.

(70) Komaba, S.; Shimomura, K.; Yabuuchi, N.; Ozeki, T.; Yui, H.; Konno, K. Study on Polymer Binders for High-Capacity SiO Negative Electrode of Li-Ion Batteries. *J Phys Chem C* **2011**, *115* (27), 13487–13495. https://doi.org/10.1021/jp201691g.

(71) Han, Z. J.; Yamagiwa, K.; Yabuuchi, N.; Son, J. Y.; Cui, Y. T.; Oji, H.; Kogure, A.; Harada, T.; Ishikawa, S.; Aoki, Y.; Komaba, S. Electrochemical Lithiation Performance and Characterization of Silicon-Graphite Composites with Lithium, Sodium, Potassium, and Ammonium Polyacrylate Binders. *Phys Chem Chem Phys* **2015**, *17* (5), 3783–3795. https://doi.org/10.1039/c4cp04939j.

(72) Nguyen, C. C.; Seo, D. M.; Chandrasiri, K. W. D. K.; Lucht, B. L. Improved Cycling Performance of a Si Nanoparticle Anode Utilizing Citric Acid as a Surface-Modifying Agent. *Langmuir* **2017**, *33* (37), 9254–9261. https://doi.org/10.1021/acs.langmuir.6b04310.

(73) Stoyko Fakirov. *Fundamentals of Polymer Science for Engineers*, 1st edition.; Wiley-VCH, 2017.

(74) Iaboni, D. S. M.; Obrovac, M. N. Li 15 Si 4 Formation in Silicon Thin Film Negative Electrodes . *J Electrochem Soc* **2016**, *163* (2), A255–A261. https://doi.org/10.1149/2.0551602jes.

(75)   Yan, Z.; Wei, C.; Obrovac, M. N. Understanding Interfacial Impedance Growth in Porous Electrodes Containing Blended Active Materials. *J Power Sources* **2019**, *438* (August), 226955. https://doi.org/10.1016/j.jpowsour.2019.226955.

(76)   Li, C.; Ju, Y.; Qi, L.; Yoshitake, H.; Wang, H. A Micro-Sized Si-CNT Anode for Practical Application: Via a One-Step, Low-Cost and Green Method. *RSC Adv* **2017**, *7* (86), 54844–54851. https://doi.org/10.1039/c7ra11350a.

(77)   Ko, M.; Chae, S.; Ma, J.; Kim, N.; Lee, H. W.; Cui, Y.; Cho, J. Scalable Synthesis of Silicon-Nanolayer-Embedded Graphite for High-Energy Lithium-Ion Batteries. *Nat Energy* **2016**, *1* (9), 16113. https://doi.org/10.1038/nenergy.2016.113.

(78)   Yoshio, M.; Wang, H.; Fukuda, K.; Umeno, T.; Dimov, N.; Ogumi, Z. Carbon-Coated Si as a Lithium-Ion Battery Anode Material. *J Electrochem Soc* **2002**, *149* (12), A1598. https://doi.org/10.1149/1.1518988.

(79)   Cao, Y.; Hatchard, T. D.; Dunlap, R. A.; Obrovac, M. N. Mechanofusion-Derived Si-Alloy/Graphite Composite Electrode Materials for Li-Ion Batteries. *J Mater Chem A Mater* **2019**, *7* (14), 8335–8343. https://doi.org/10.1039/c9ta00132h.

(80)   Yokoyama, T.; Urayama, K.; Yokoyama, T. Ultra-Fine Grinding and Consequent Changes of Powder Characteristics. *KONA* **1983**, *1*, 53–63. https://doi.org/10.14356/kona.1983010

(81)   Liu, Y.; Charlton, M.; Wang, J.; Bennett, J. C.; Obrovac, M. N. Si 85 Fe 15 O x Alloy Anode Materials with High Thermal Stability for Lithium Ion Batteries . *J Electrochem Soc* **2021**, *168* (11), 110521. https://doi.org/10.1149/1945-7111/ac3163.